Metallicity Estimation of Core-Collapse Supernova Environments within 30 Mpc

Rudi Ganss

*A thesis submitted in partial fulfilment for the requirements for
the degree of Master of Science (by Research)*

Jeremiah Horrocks Institute for Maths, Physics and Astronomy
University of Central Lancashire

June 2020

Declaration

The work presented in this thesis was carried out at the Jeremiah Horrocks Institute for Maths, Physics and Astronomy, University of Central Lancashire. This thesis has been submitted in partial fulfilment of the requirements for the degree of Master of Science.

I declare that while registered as a candidate for the research degree, I have not been a registered candidate or enrolled student for another award of the University or other academic or professional institution.

I declare that no material contained in the thesis has been used in any other submission for an academic award.

I declare that this thesis is the result of my own work unless otherwise stated.

No proof-reading service was used in the compilation of this thesis.

Signature of Candidate _____
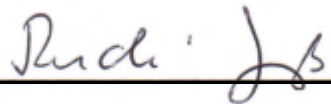
Rudi Ganss

Abstract

This thesis researches the local metallicities of environments of Type IIP, Type Ib and Type Ic supernovae (SNe), within a luminosity distance of 30 Mpc, by long-slit spectroscopy. During the runtime of the project 76 targets out of a sample of 110 selected targets could be observed at the Isaac Newton Telescope (INT) on La Palma. For 66 observed targets the metallicities could be measured by the N2 and O3N2 strong emission line methods, using calibrations of Pettini and Pagel (2004, PP04) and Marino et al. (2013, M13). The PP04 mean values of the local metallicities are about 8.62 dex. The metallicities by M13 are about 0.1 dex less. No significant differences between the means of the three SN types have been found. The sample of the INT observations has been extended by the results of previous work of 46 targets meeting the selection criteria of the project. Again, no significant differences between the means of the three SN types have been found.

Normalised cumulative distribution functions (CDFs) of the metallicities of the three SN types are presented. Type Ib and Ic distributions tend to higher metallicity than Type IIP, however Type Ic SNe are also present at lower metallicities whereas Type Ib SNe are not. The Type Ib distribution is narrower than both the Ic and IIP distributions. The Kolmogorov-Smirnov test as well as the Anderson-Darling test indicates no statistical significance for a difference in the local metallicities of the three SN types.

The narrow CDFs of Type Ib SNe give some evidence for a significant fraction of single massive progenitor stars, whilst the low metallicity of Type Ic suggests a significant fraction of compact binary progenitors. More observational data and additional statistical tests such as Monte Carlo simulation by future work are required to further constrain the progenitor stars of Type Ib,c SNe.

Content

Acknowledgements

List of Tables

List of Figures

Chapter 1

Introduction

Nucleosynthesis in the Big Bang only produced the lightest elements hydrogen and helium and some traces of lithium. All subsequent chemical evolution of the universe was driven by stars. Massive stars are the key player in chemical enrichment of the universe. Their strong stellar winds and their ultimate death as supernovae (SNe) enrich the interstellar medium with chemical elements burned during a star's lifetime and with new elements created in the SN explosion. The strong radiation and the explosion shock waves trigger (or - depending on the circumstances - can prevent) new star formation episodes reprocessing the burned chemical elements in new stellar life cycles. In order to understand details of the SN explosion process and the elements beyond iron formed in the explosion, the knowledge of the nature of SN progenitor stars is essential. This introductory chapter gives a brief overview on the different types of SNe, on evolutionary phases of the massive stars believed to be progenitors of core-collapse SNe and on methods and results of the search for SN progenitors.

1.1 Supernovae in the Universe

1.1.1 Supernovae Types

Historically, the classification of SNe is mainly based on spectral features and divided in two main types: the hydrogen-poor Type I SNe and the hydrogen-rich Type II SNe (Figure 1-1).
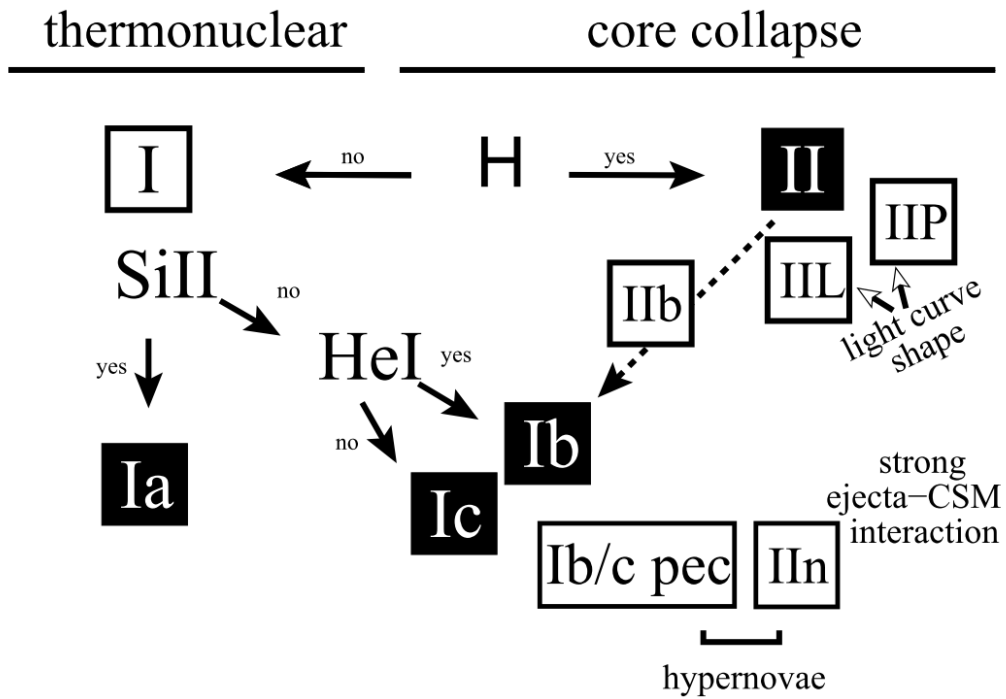
Figure 1-1: Classification scheme of SNe (image: Turatto 2003).

The hydrogen-poor Type I SNe are further divided in three sub-types Ia, Ib and Ic by features in the early spectrum around peak luminosity time. Type Ia SNe are characterised by strong Si II absorption features and the absence of helium and hydrogen lines, Type Ib spectra show strong helium but no hydrogen absorption lines and Type Ic spectra have neither hydrogen nor helium lines.

The hydrogen-rich Type II SNe are divided in four sub-types IIL, IIP, IIn and IIb. The most common types IIP and IIL are characterised by the shape of their light curves. Light curves of Type IIP have a distinct plateau phase after the peak luminosity where the luminosity is almost constant or has a slow decline, in contrast to the light curve of Type IIL SNe showing a steady (more or less linear) decrease after the peak luminosity (Figure 1-2).

The spectra of Type IIP and IIL are characterised by broad hydrogen emission lines (e.g. Gutiérrez et al. 2017) indicating high expansion velocities of the SN ejecta and/or surrounding stellar medium. In contrast, Type IIn SNe are characterised by relatively narrow emission lines (e.g. Taddia et al. 2013). The Type IIb SNe have an intermediate character between Type II and Type I SNe. This SN type has hydrogen lines in the early, photospheric phase which disappear in the later nebular phase when the ejecta becomes optically thin (e.g. Fang and Maeda 2018).
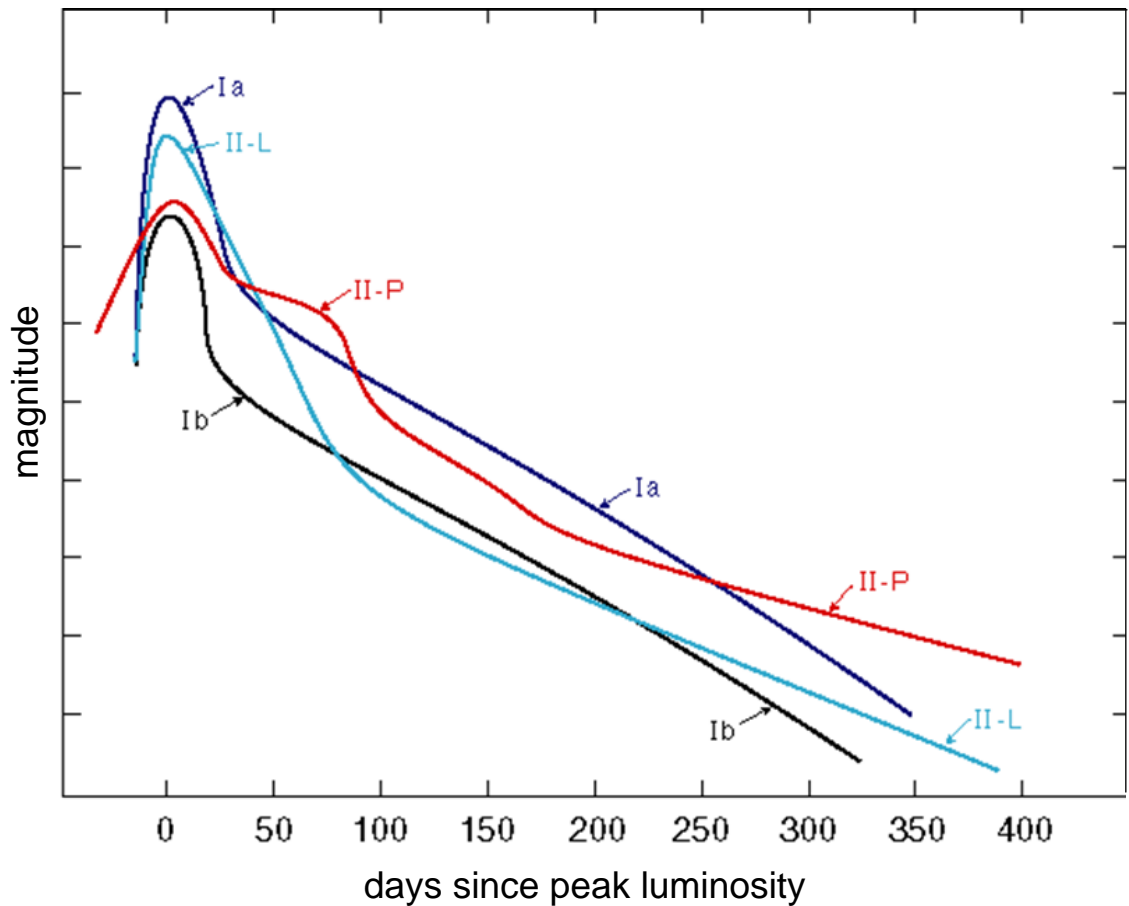
Figure 1-2: Schematic light curves of the different SN types. Light curve of Type Ib includes Type Ic as well. A distinct plateau phase characterises Type IIP light curve against a Type IIL light curve (image W.Hillebrandt[1] , adapted from Filippenko 1997).

In addition to these regular SN types, there are high energetic SNe events ("Hypernovae") not fitting into the scheme above. They are generally classified as Type Ibc-pec, also named as Types Ic-bl (if very broad lines in spectrum, e.g. Taddia et al. 2019) or Type Ic-GRB (if associated by a gamma ray burst; e.g. Woosley and Bloom 2006). A class of its own are superluminous SNe with absolute magnitudes $M_V < -21$ (e.g. Gal-Yam 2019).

1.1.2 Supernovae Rates and Environments

Differences in the rates and environments of particular SN types can provide constraints for the SNe progenitors. The most recent study of SN rates and environments in the local universe has been done by Li et al. (2011a, 2011b) based on observations with the Lick observatory (Figure 1-3).

---

[1] https://slideplayer.org/slide/789544/
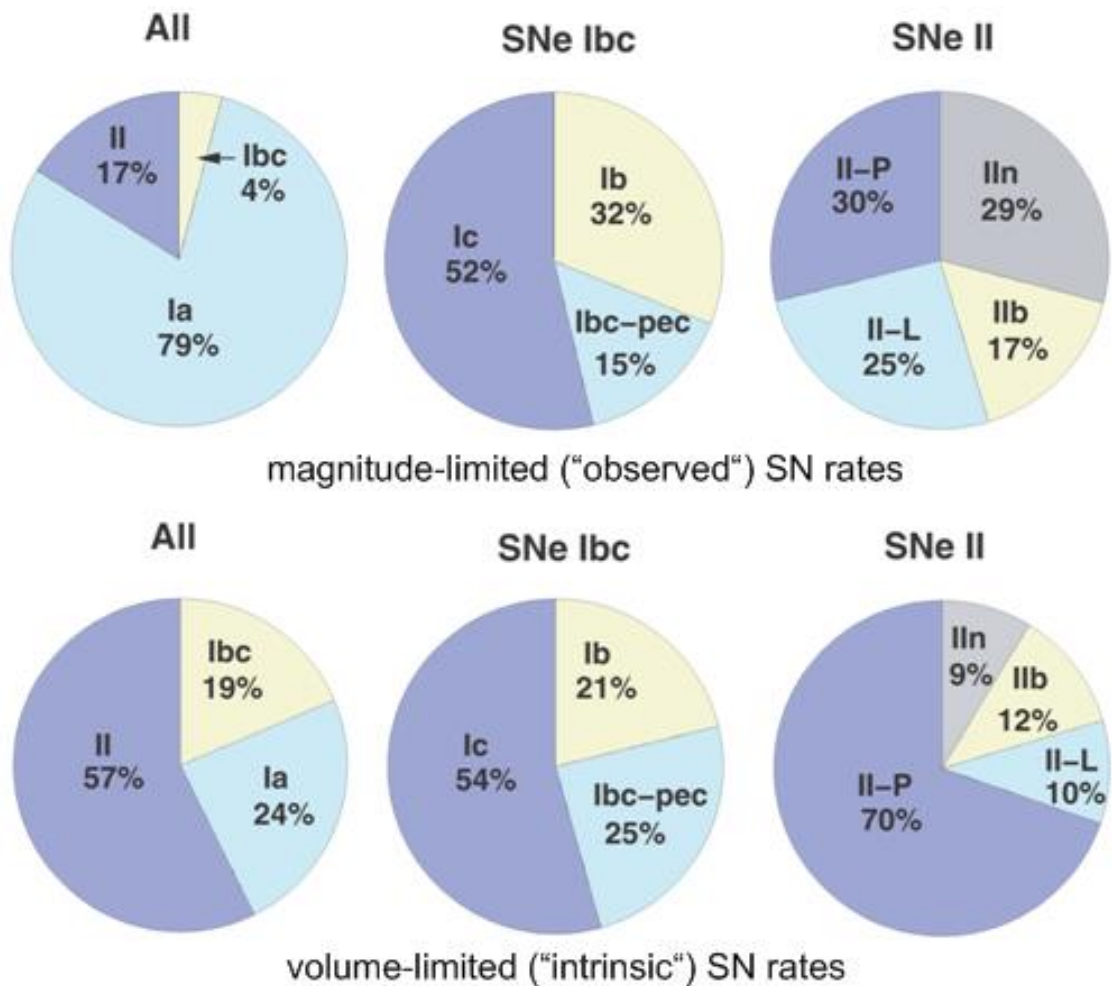
Figure 1-3: SN rates in the local universe. The upper panel shows the rates as observed (magnitude-limited) in the local universe. Type Ia is by far the most observed SN type and Type Ib,c SNe are rare. Taken into account the different luminosities of the SN types change the picture (lower panel): the intrinsic (volume-limited) SN rate is dominated by Type II SNe with more than the half of SN events (image adapted from Li et al. 2011a).

The upper panels of Figure 1-3 are the observed SN rates. The most observed SNe are Type Ia with 79% followed by 17% Type II and just 4% Type Ib,c (throughout this work 'Type Ib,c' means 'Type Ib and Type Ic'). But the observed rates are not coincident with the true, intrinsic rate of the SNe types because of the different luminosities of the SNe; e.g. Type Ia are generally more luminous than Type II and Type Ib,c (see section 1.1.3) and they are therefore more often observed. The lower panel of Figure 1-3 takes these differences into account and the picture changes completely: the most common SN type is Type II, followed by Type Ia. Within the Type II cohort, the Type IIP SNe are dominant by 70% over the almost equally partitioned other three Type II sub-classes. Type Ib,c SNe are dominated by Type Ic to about the half, Type Ib and Type Ibc-pec have almost the same frequency with 21% and 25%, respectively.
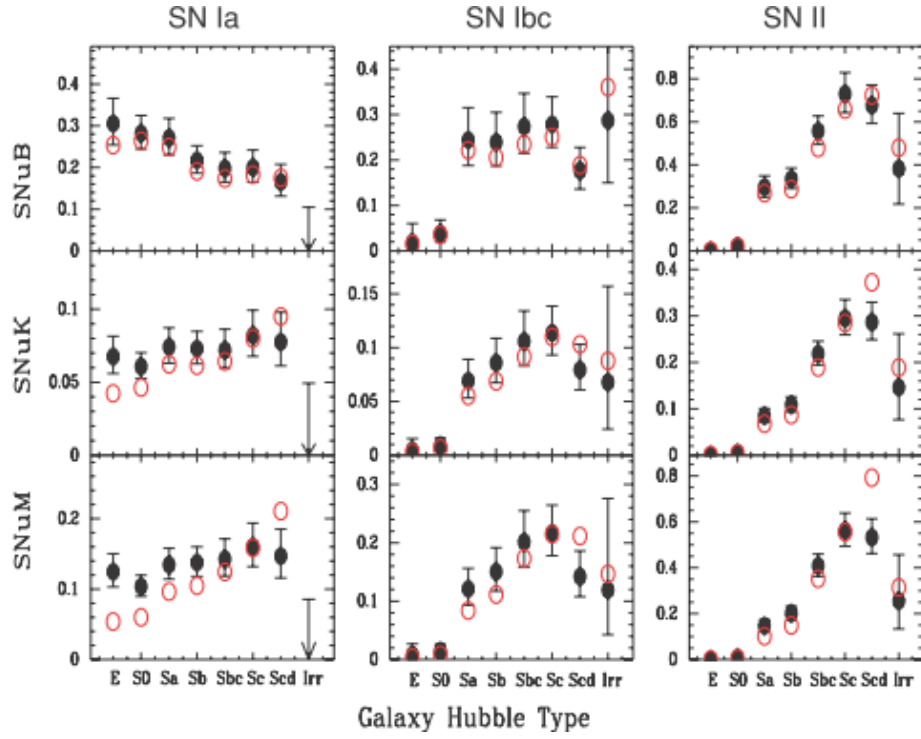
Figure 1-4: SN rates for galaxies with different Hubble types. Solid circles are the rates estimated with the apparent (fiducial) sizes of the galaxies, open circles the values based on the median size of the galaxies. The rates are expressed in "supernova units" SNu defined by 1 SN per 100 years and per 10^{10} solar (bolometric or K-band) luminosities or solar masses, respectively: 1 SNuB=1 SN$(100yr)^{-1}(10^{10}L_{\odot}^{B})^{-1}$, 1 SNuK=1 SN$(100yr)^{-1}(10^{10}L_{\odot}^{K})^{-1}$ and 1 SNuM=1 SN$(100yr)^{-1}(10^{10}M_{\odot})^{-1}$ (Li et al. 2011b).

Figure 1-4 shows the galactic environments of Type Ia, Ib,c and II SNe. While SN Ia are common in all galaxy types, Types Ib,c and II are common in late type galaxies only, preferably in the spiral arms with enhanced star formation (Anderson et al. 2015).

1.1.3 Supernovae Luminosities and Energies

The light curves of SNe differ in magnitude and shape (Figure 1-2) implicitly reflecting the different physical conditions of the progenitors and their environments.

Type Ia SNe are the most luminous regular SNe events with absolute bolometric magnitudes up to $M_{bol} \sim$ -19.46. Type Ib,c SNe are about 2 mag fainter with $M_{bol} \sim$ -17.61. Type IIL SNe are the brightest SNe of Type II with $M_{bol} \sim$ -17.56, Type IIP are with $M_{bol} \sim$ -17.00 about 0.5 mag fainter (all values taken from Richardson et al. 2002; without superluminous SNe).

The rise time of the light curve to the peak is 15-25 days for all SN types (e.g. Li et al. 2011a). The decline time depends on type: Type Ia SNe decline within about 60 days to 10% (Δ2.5 mag) of the peak luminosity, Type Ib,c need around 80 days (with a large scatter from 40-100 days) and Type II SNe decline generally in more than 100-150 days (e.g. Li et al. 2011a).

The liberated energy of a SN explosion is about the same order of magnitude for all SN types. A typical Type II SN explosion liberates energy in the order of 10^{53} erg, of which 10^{51} erg appear as kinetic energy and 10^{49} erg are released as electromagnetic radiation. The large majority of energy is transported by the radiation of neutrinos (Carroll and Ostlie 2006).

The physical powering mechanism for all SNe types, except SNe Ia, is the liberation of gravitational energy when the core of a massive star collapses after exhausting the nuclear fuel in the core. Thus SN types Ib, Ic and II are also called core-collapse SNe.

Type Ia SNe are believed to be powered by the thermonuclear explosion of (at least) one degenerate white dwarf star in a binary system (review e.g. Maoz et al. 2014). Because the focus of this work is on core-collapse SNe, the Type Ia SNe will not further discussed.

1.2 Massive Star Evolution

The lower initial mass limit for a star to produce a core-collapse SN is commonly accepted to be ~8 $M_\odot$ (e.g. Smartt 2009). This sub-section briefly describes the evolution of massive stars with masses >8 $M_\odot$ from the main-sequence to the end of their life as core-collapse SN explosion.

1.2.1 Massive Stars and HII Regions

Main sequence stars with masses above 8 $M_\odot$ are classified as O-type or early B-type (OB-stars for short) in the Havard spectral classification scheme (e.g. Carroll and Ostlie 2006) depending on their temperature.

The surface temperatures of O-stars are high enough to emit Lyman continuum photons (e.g. Sternberg et al. 2003). The energetic Lyman photons ionise the surrounding hydrogen gas resulting in a Strömgren-sphere (Strömgren 1939) with ionised hydrogen around the star. The radius r_S of a Strömgren-sphere depends on the number N of the ionising photons per second, the number density n_H of hydrogen and the quantum-mechanical recombination coefficient α (likelihood that an electron and a proton can form a hydrogen atom) and is given by (e.g. Carroll and Ostlie 2007):

$$r_S \cong \sqrt[3]{\frac{3}{4\pi} \frac{N}{\alpha\, n_H^2}} \qquad \text{(Eq. 1-1)}$$

Table 1-1: Physical parameters of HII regions (Kurtz 2005).

Class of Region	Size (pc)	Density (cm^{-3})	Emis. Meas. $(pc\ cm^{-6})$	Ionized Mass $(M_\odot)$
Hypercompact	$\lesssim 0.03$	$\gtrsim 10^6$	$\gtrsim 10^{10}$	$\sim 10^{-3}$
Ultracompact	$\lesssim 0.1$	$\gtrsim 10^4$	$\gtrsim 10^7$	$\sim 10^{-2}$
Compact	$\lesssim 0.5$	$\gtrsim 5 \times 10^3$	$\gtrsim 10^7$	~ 1
Classical	~ 10	~ 100	$\sim 10^2$	$\sim 10^5$
Giant	~ 100	~ 30	$\sim 5 \times 10^5$	10^3–10^6
Supergiant	> 100	~ 10	$\sim 10^5$	10^6–10^8

Because most stars are formed in clusters (e.g. Lada and Lada 2003), the Strömgren-spheres of massive stars in the cluster may overlap and build larger HII regions. The sizes of these HII regions can be quite different, depending on the number of hosted ionising stars, the star temperatures, the density and temperature of the gas. The sizes range from 0.03 pc for hypercompact HII regions to sizes >100 pc for supergiant HII regions (Table 1-1).

The massive OB-stars have to burn their hydrogen fuel much quicker than lower mass stars to keep in hydrostatic equilibrium. Thus, despite their high mass, the lifetime on the main sequence is very short and lasts just a few million years (typically 3 Myr for the most massive O-stars with initial masses of 120 $M_\odot$ to 16 Myr for initial 12 $M_\odot$ B1-stars, Conti et al. 2012). If the hydrogen fuel in the core is exhausted, it contracts and heats up until the fusion of the helium ashes in the core starts at higher temperatures, while the remaining hydrogen in outer layers is burning in a shell around the core. After exhausting the helium in the core, the process continues with carbon burning at again higher core temperatures and with shorter timescale (Table 1-2) as the next stage. Over the course of the time, the star develops an "onion" structure in its central region with shells burning different elements (Figure 1-5).

Table 1-2: Burning phases of a massive star with initial mass of 15 $M_\odot$. The larger the number of protons of the fuel the higher required core temperature and the shorter timescale of burning phase; data taken from Woosley et al. (2002).

burning phase	T [10^9K]	ρ [g/cm^3]	fuel	main products	timescale [yr]
hydrogen	0.035	5.81	H	He	1.11×10^7
helium	0.178	1.39×10^3	He	C, O	1.97×10^6
carbon	0.834	2.39×10^5	C	O, Ne	2.03×10^3
neon	1.63	7.24×10^6	Ne	O, Mg	0.732
oxygen	1.94	6.66×10^6	O, Mg	Si, S	2.58
silicon	3.34	4.26×10^7	Si, S	Fe, Ni	0.051
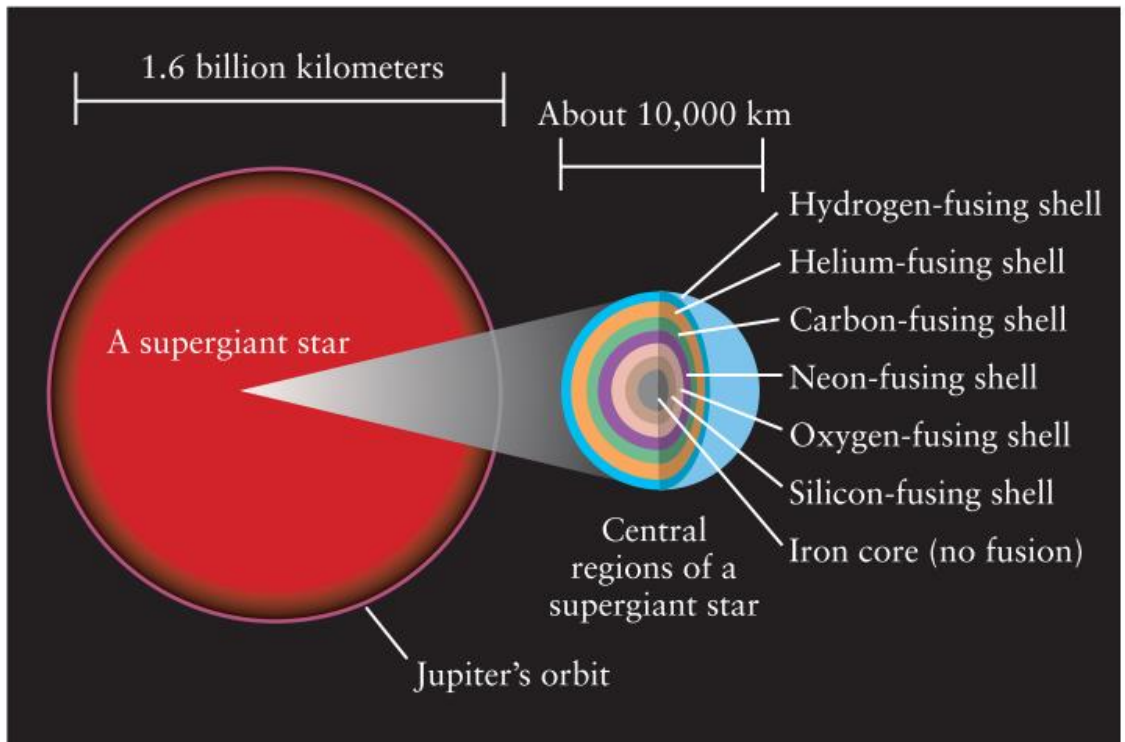
Figure 1-5: "Onion" structure of the central region of an evolved supergiant star around the core with different burning stage (image: Freedman and Kaufmann 2008).
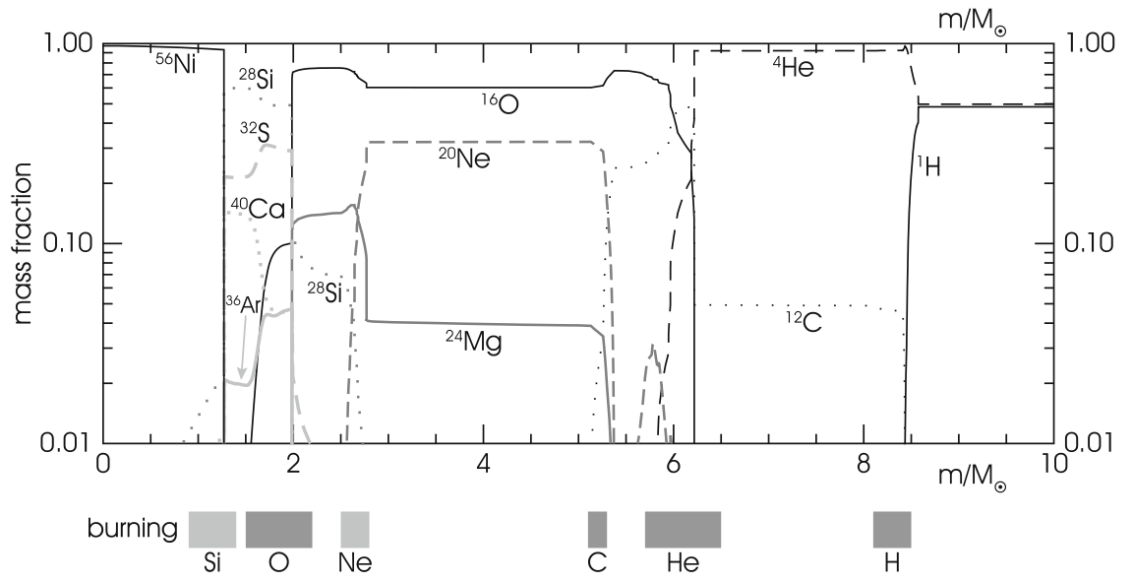
Figure 1-6: Chemical composition of the interior of a highly evolved population I star with initial mass of 25 $M_\odot$ close to the end of the hydrostatic nuclear burning. The image shows the mass concentration of important elements against the mass variable m(r). The grey boxes indicate the approximate positions of the different nuclear burning phases (image: Kippenhahn et al. 2012)

Figure 1-6 shows the chemical composition of such a highly evolved massive star close to the end of the hydrostatic nuclear burning. The grey boxes approximately indicate the positions of the different nuclear burning shells.

Like during the main-sequence phase the hydrogen burning shell fuses hydrogen to helium by the CNO-cycle pathway using carbon, nitrogen and oxygen as catalyst of the fusion of four protons to helium. The CNO cycle is preferred against the proton-proton fusion chain because of the high temperatures in massive stars.

The predominant fusion process in the helium burning shell is the triple-alpha process giving carbon as end product:

$$^4\text{He} + {}^4\text{He} \rightarrow {}^8\text{Be} + \gamma$$
$$^8\text{Be} + {}^4\text{He} \rightarrow {}^{12}\text{C} + \gamma$$
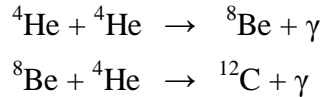
Additional elements burned in the Helium shell are nuclei with an even number of protons e.g. ^{16}O, ^{20}Ne, ^{24}Mg, … as result of subsequent ^{4}He fusions (alpha processes). At the boundary to the hydrogen shell nuclei with odd numbers of protons are fused by subsequent fusion of carbon with protons. The most important product of such processes is ^{14}N via the nuclear processes (these reactions are also part of the CNO cycle):

$$^{12}\text{C} + {}^1\text{H} \rightarrow {}^{13}\text{N} + \gamma \rightarrow {}^{13}\text{C} + e^+ + \nu_e$$
$$^{13}\text{C} + {}^1\text{H} \rightarrow {}^{14}\text{N} + \gamma$$
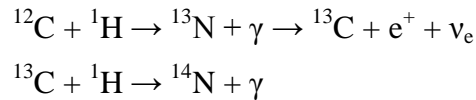
The ^{14}N product can be processed by subsequent alpha processes to heavier odd numbered and/or neutron-rich (most important: ^{22}Ne) nuclei.

The predominant process in the carbon shell is the fusion of carbon to neon and magnesium by the processes

$$^{12}\text{C} + {}^{12}\text{C} \rightarrow {}^{20}\text{Ne} + {}^4\text{He}$$
and
$$^{12}\text{C} + {}^{12}\text{C} \rightarrow {}^{24}\text{Mg} + \gamma$$
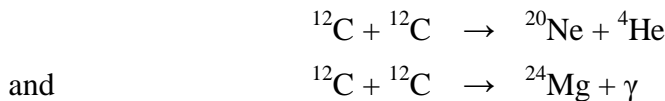
Before the temperatures towards the star core get high enough for oxygen fusion, the endothermic disintegration of ^{20}Ne by high energetic photons followed by a subsequent fusion process of remaining ^{20}Ne becomes energetically more favourable (e.g. Woosley et al. 2002) and provides a net energy of 4.586 MeV by the reactions

$$^{20}\text{Ne} + \gamma(4.73\text{MeV}) \rightarrow {}^{16}\text{O} + {}^4\text{He}$$
$$^{20}\text{Ne} + {}^4\text{He} \rightarrow {}^{24}\text{Mg} + \gamma(9.316\text{MeV})$$
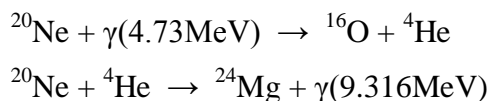
The prevalent fusion process in the oxygen shell provides silicon the by reaction

$$^{16}\text{O} + {}^{16}\text{O} \rightarrow {}^{28}\text{Si} + {}^4\text{He}$$

Many other reactions are possible by the ^{4}He product via alpha processes.

The last process providing fusion energy is the silicon burning that provides (among others) ^{56}Ni as end product that decays to ^{56}Fe:

$$^{28}\text{Si} + {}^{28}\text{Si} \rightarrow {}^{56}\text{Ni} + \gamma$$
$$^{56}\text{Ni} \rightarrow {}^{56}\text{Co} + e^+ + \nu_e \rightarrow {}^{56}\text{Fe} + e^+ + \nu_e$$
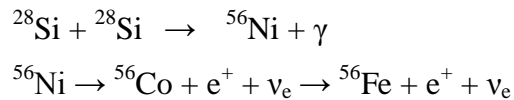
The fusion ash iron stops the fusion process. Burning iron is an endothermic reaction and requires energy rather than produces it. With iron in the core, the star gets unstable and the core collapses under its gravity in less than a second (e.g. Janka 2012) triggering a core-collapse SN explosion.

1.2.2 Evolutionary Track in the Hertzsprung-Russell Diagram

Like all other stars massive stars leave the main sequence after exhausting the hydrogen fuel in their cores. But their track in the Hertzsprung-Russell (HR)-diagram significantly differs from lower mass stars: because massive stars never develop a degenerate core, they never experience He-core/shell flashes with strongly increasing luminosities like lower mass stars. Thus, the post main-sequence evolution of massive stars is more gradual: they are moving more or less horizontally through the HR-diagram during the hydrogen shell/helium core burning with almost constant luminosity towards the RSG region where the carbon burning starts.

The actual shape of the evolutionary track of a massive star in the HR-diagram strongly depends on its mass loss by stellar winds. Figure 1-7 shows examples of some evolutionary tracks. Massive stars with initial masses of up to approximately 15-20 $M_\odot$ (all mass values strongly depend on parameters like rotation and metallicity) evolve via short transitional phases of a few 1000 years as blue (BSG) and yellow (YSG) supergiants (e.g. Crowther et al. 2006; Massey 2013) to the end stage as red (RSG) supergiants (e.g. Levesque 2010). Stars in this mass range do not suffer so much mass loss and they stay in the RSG region where they finally explode as core-collapse SNe.

More massive stars, initial masses of ~20-40 $M_\odot$, experience significant mass loss in the RSG region by stellar winds and evolve back to YSG/BSG supergiant region. Depending on their initial mass, metallicity and rotation these stars can oscillate back to the RSG region or develop to a luminous blue variable (LBV) star (Smith 2017) or a WR star.
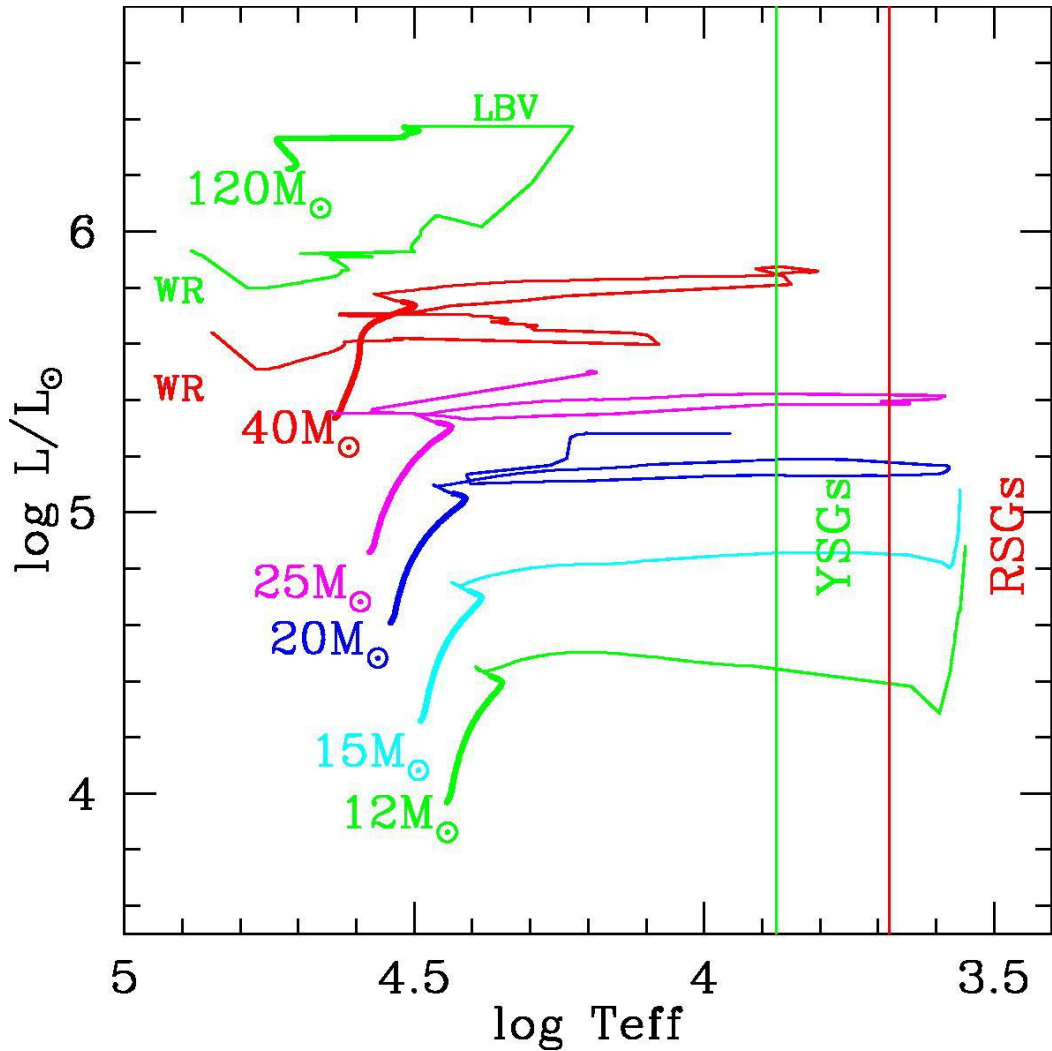
Figure 1-7: Evolutionary tracks of massive stars (all masses are initial masses) through the HR-diagram calculated with the Geneva code (Ekström et al. 2012). The vertical green and red lines mark the general regions of yellow supergiants and red supergiants, respectively; see text for a short description of the shape of the tracks (image: Massey 2013).

Massive stars with initial masses larger than ~40 $M_\odot$ do not evolve to a RSG at all because their outer envelope approaches the (modified) Eddington limit (Eddington limit is the maximum luminosity of a body at which the outward acting radiation pressure balances the inward acting gravity; e.g. Sanyal et al. 2015) with their high luminosities. These stars evolve to a LBV and develop large mass loss by inflation, strong stellar winds and/or eruptions which drive the stars back to higher temperatures in the HR-diagram where they end their lives as WR star. There is also observational evidence that LBVs can explode as Type IIb SNe (Groh et al. 2013).
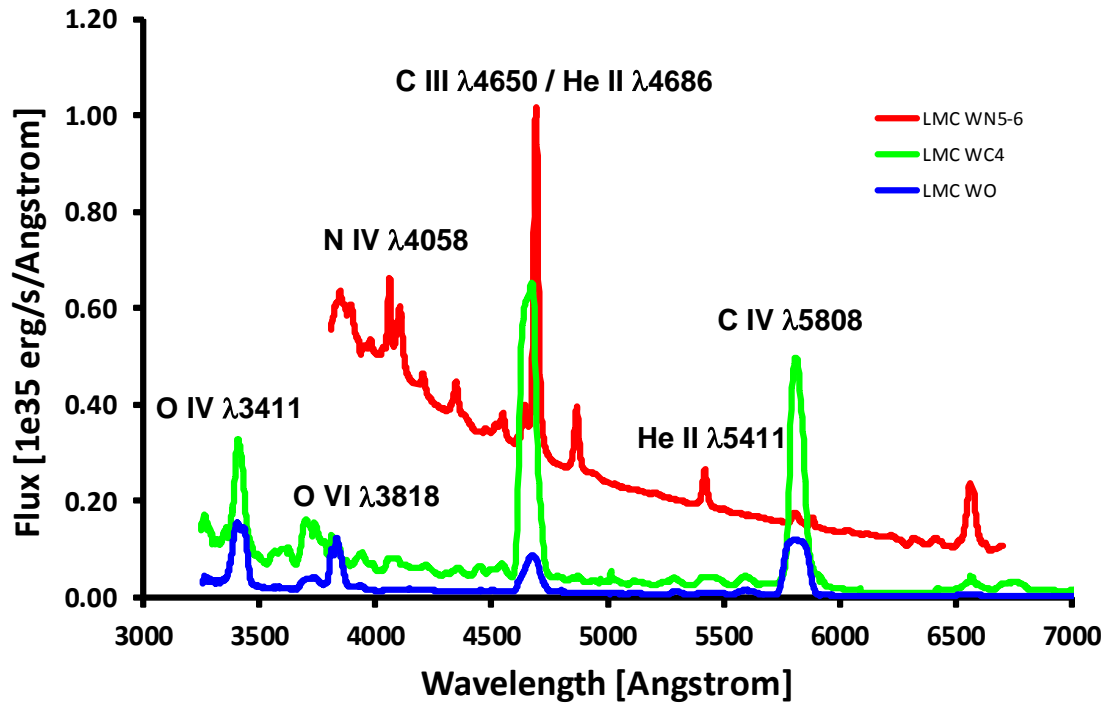
Figure 1-8: Spectral templates for different WR star types of the Large Magellanic Cloud. The figure was generated by the current author, based on data downloaded from the webpage of P. Crowther[2] and described in Crowther and Hadfield 2006.

1.2.3 Wolf-Rayet Stars

The WR stars (see Crowther 2007 for a review), discovered by Wolf & Rayet in 1867, are characterised by their unusual stellar spectra with broad emission lines of ionised helium and highly ionised burning products nitrogen, carbon and (rarely) oxygen. They are believed to be the evolved state of the most massive stars (see section 1.2.2).

WR stars are classified in three main types depending on their spectral features (Figure 1-8; review paper e.g. Crowther 2007):

- WN stars are characterised by emission lines of He I-II and N III-V
- WC stars are characterised by emission lines of He I-II and C III-IV
- WO stars are characterised by emission lines of He I-II, C IV and O V-VI

Based on the intensity ratios of their characteristic lines, WN stars are sub-divided into 9 sub-types, WC stars in 8 sub-types and the rare WO stars in 4 sub-types (e.g. van der Hucht 2001). Special spectral features are indicated by additional suffixes (e.g. 'h' for presence of hydrogen lines, 'w' for weak lines, etc.).

[2] http://www.pacrowther.staff.shef.ac.uk/science.html

12

The broad emission lines indicate that fast stellar winds are causing a large mass loss rate of the WR stars. The estimated mass loss rate goes up to about 10^{-5} $M_\odot/yr^{-1}$ (Tramper et al. 2016). The details of the physical mechanisms creating the strong stellar winds are not fully understood yet (e.g. Puls et al. 2008) but it is commonly accepted that they are driven by radiation lines. Thus, the mass loss due to winds depends in first order on the metallicity and the luminosity of the WR star: at higher luminosities and metallicities, the winds are stronger (e.g. Tramper et al. 2016). Because WR stars lose their outer shells by their strong winds, they are predicted to be progenitors stars of Type Ib,c SNe (see section 1.2.4).

1.2.4 Ultimate Fate of Massive Stars

The ultimate fate of a massive star is the SN explosion and the type of SN depends on the physical properties of the star, primarily its mass and its metallicity. Figure 1-9 shows the assumed resulting SN type depending on initial mass and metallicity. At solar metallicity, all massive stars finally explode as core-collapse SNe. The boundary between Type II and Type Ib,c SNe is at about 34 $M_\odot$ for solar metallicity. It goes to lower initial masses if the metallicity increases (stronger winds, see section 1.2.3).
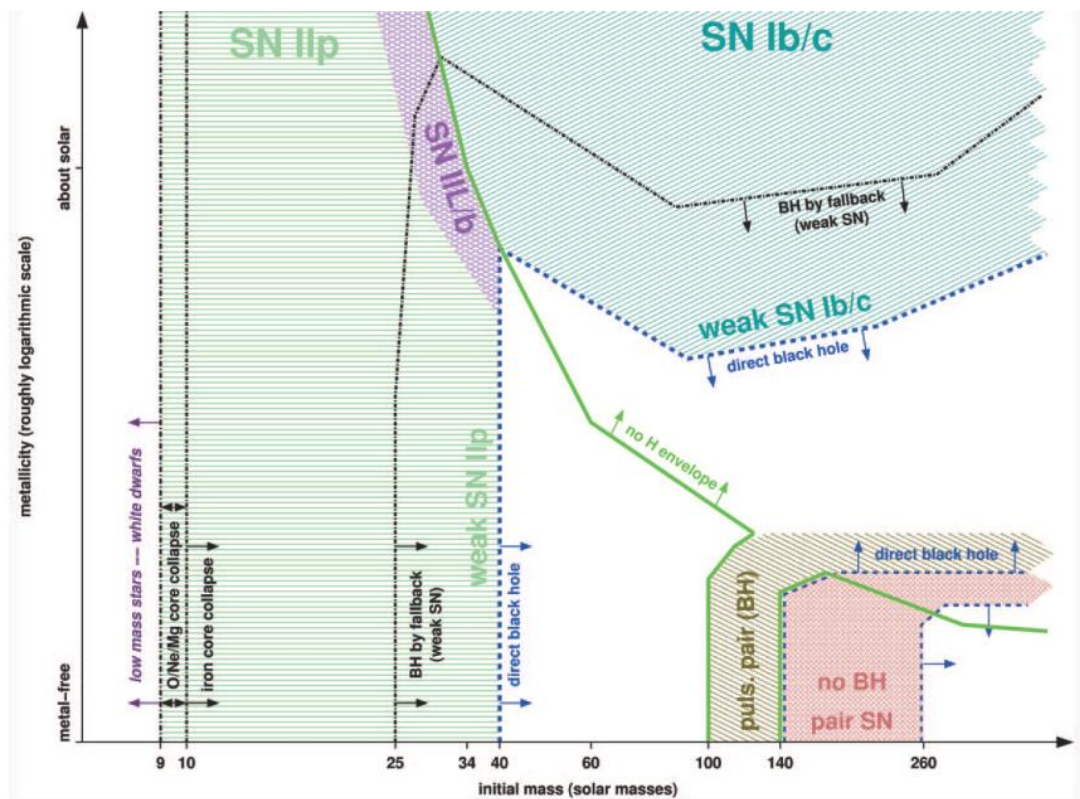
Figure 1-9: The ultimate fate of a massive star depends on its physical properties, primarily mass and metallicity (other important attributes are e.g. rotation and magnetic field). The figure, taken from Heger et al. 2003, shows the resulting types of SNe depending on initial mass and metallicity for non-rotating stars.

Type II SNe also occur in low metallicity environments up to initial mass of about 40 M$_\odot$. According to Figure 1-9, Type Ib,c SNe are not possible in low metallicity environments because the massive stars >40 M$_\odot$ directly collapse to a black hole without a SN event. Only the highest mass stars (>140 M$_\odot$) can explode as pair-instability SNe (e.g. Kozyreva et al. 2014) in such low metallicity environments.

Single massive stars seem to be the "natural" candidates for progenitors of core-collapse SNe. Depending on the violence of their stellar winds and the initial mass, massive stars may keep the hydrogen envelope (=>Type IIP), lose the hydrogen envelope (=> Type Ib) or even lose the remaining helium envelope (=> Type Ic). Radiatively driven stellar winds are the stronger the higher luminosity (and hence initial mass) and metallicity (e.g. Kudritzki and Puls 2000). Thus, the single massive star scenario should observationally result in a sequence of increasing initial progenitor mass and/or metallicity from Type IIP via Type Ib to Type Ic.

In summary, the single massive progenitor evolution (e.g. Crowther et al. 1995) to SN looks as follows (given mass ranges are illustrative only,):

8 M$_\odot$ ≲ M ≲ 25 M$_\odot$: O(B)-star → RSG → SN II

25 M$_\odot$ ≲ M ≲ 40 M$_\odot$: O-star → RSG/LBV → WN → SN Ib

M ≳ 40 M$_\odot$: O-star → LBV → WN → WC → SN Ic

1.2.5 Interacting Binaries

There is a second scenario for massive stars to get rid of their outer envelope(s). Most massive stars are born in multiple systems (e.g. Duchêne and Kraus 2013). For massive stars the fraction of close binaries (separation < 1 AU) increases dramatically (Sana et al. 2012) and the evolution of such close systems is influenced by binary interactions (Sana et al. 2013).

If the more massive primary star of a close binary evolves in the supergiant phase to a size that fills its Roche lobe (Figure 1-10), then mass will be transferred to the companion star and the primary star will lose its outer envelope(s). This progenitor scenario of stripped Type Ib,c SNe works at lower initial masses than the single massive scenario: a star which normally remains a RSG and end its life as a Type II SNe will undergo stripping as a result of the binary interaction, losing its outer layers and becoming a stripped, WR-like star, consequently producing a Type Ib or a Type Ic SNe.
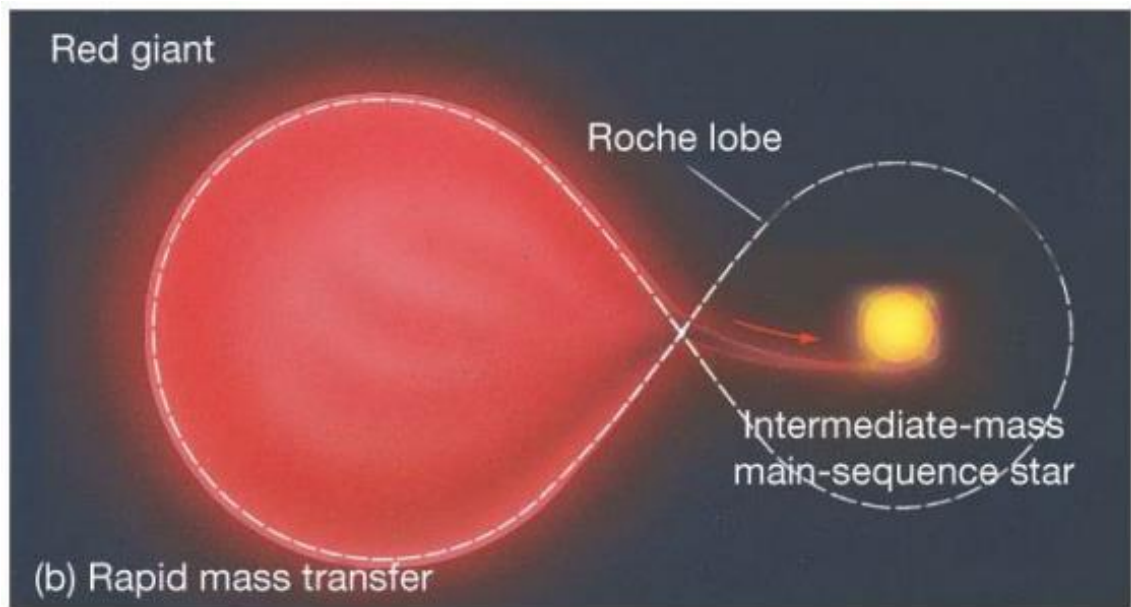
Figure 1-10: Schematic view of an interacting binary system. If the primary star evolves to a size where it fills its Roche lobe, mass is transferred through the inner Lagrange point to the secondary star (image: C.Reynolds[3]).

1.3 Search for Progenitors of Core-Collapse Supernovae

1.3.1 Type IIP Progenitors

The most direct approach to find a SN progenitor is to search in archival pre-explosion images of the SN explosion site. This approach has been successful for SNe Type IIP progenitors (Figure 1-11).

The first progenitor found this way was the progenitor of SN2003gd in M74 (Van Dyk et al. 2003, Smartt et al. 2004). Meanwhile the number of direct identifications increased significantly. Smartt (2015) compiled a list of 26 identified Type II (21 of them classified as IIP) progenitor stars detected from 2003 to 2014 and presented their positions in the HR-diagram (Figure 1-12). All Type IIP progenitors are in the RSG region as expected (recall Figure 1-7).

FORS BVI and ISAAC K

NACO K

WFC F439W, F555W, F814W

ACS HRC F330W, F555W, F814W

WFPC2 F300W, F606W, F814W

ACS HRC F435W, F555W, F814W

5" (95 pc)

1" (41 pc)

1" (45 pc)
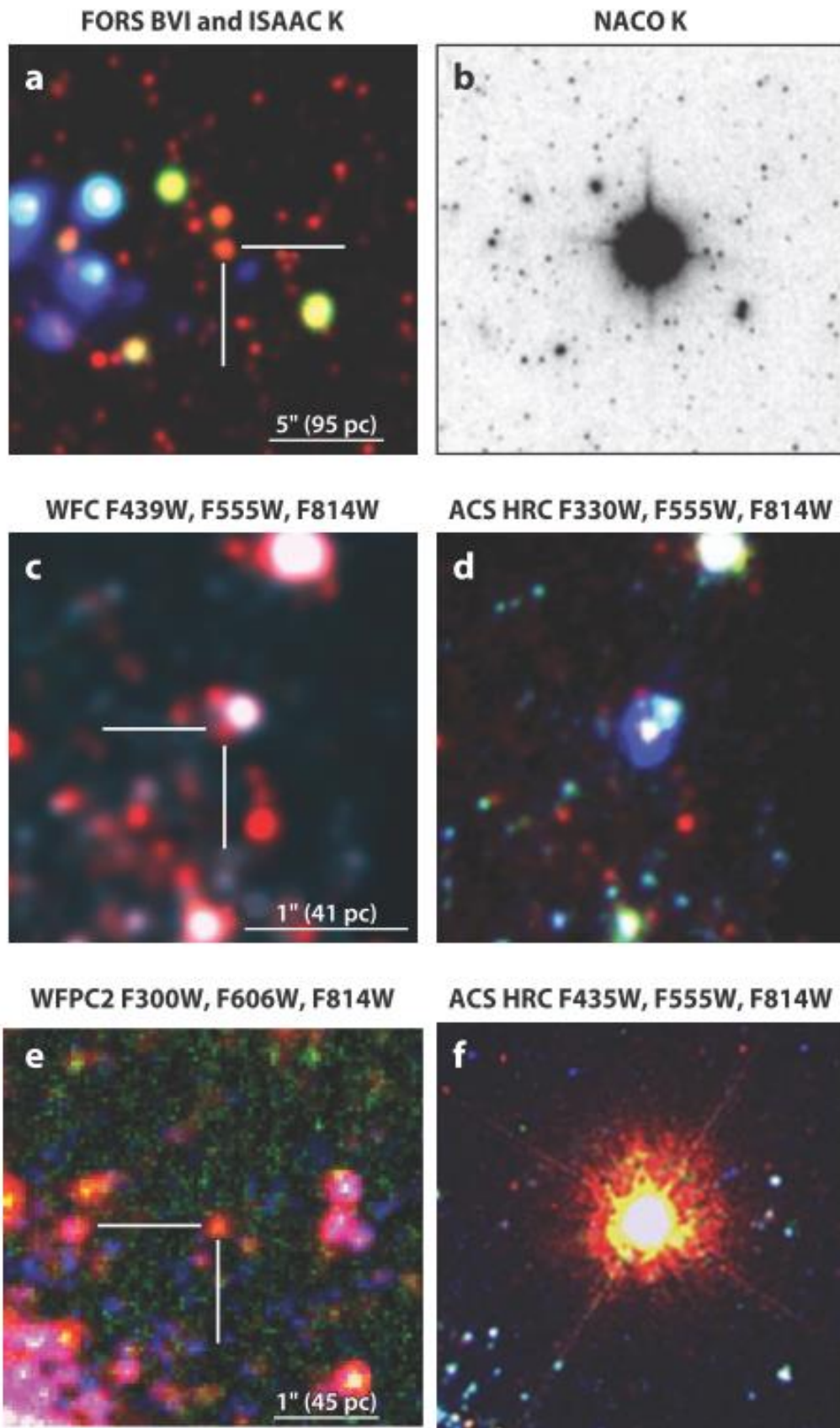
Figure 1-11: Examples for Type II-P progenitors in archival pre-explosion images. The figure shows the pre-explosion (left column) and post-explosion images (right column) of SN2008bk (top), SN2005cs (middle) and SN2003gd (bottom). For all three cases the progenitor star has been identified as a RSG (image: Smartt 2009).
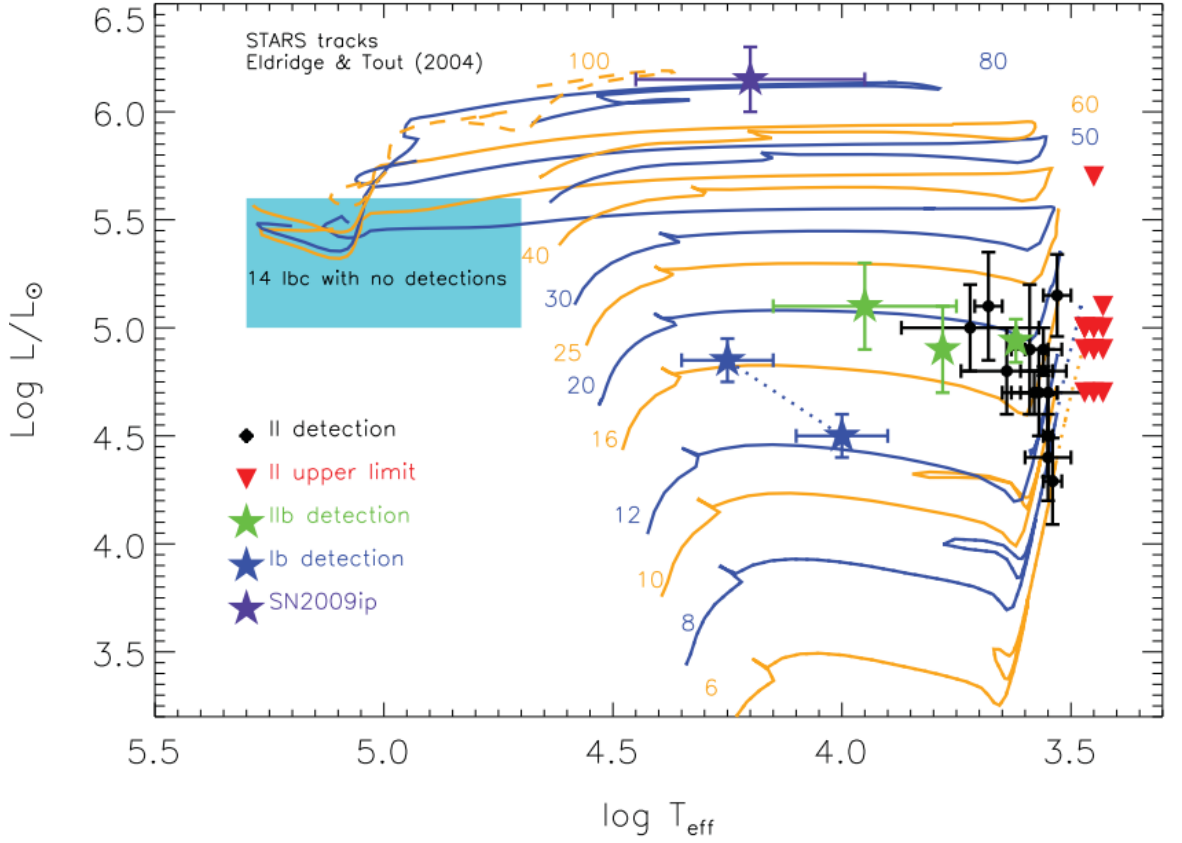
Figure 1-12: Positions of Type II progenitor identifications (black and red symbols) in the HR-diagram. All Type II progenitors have been identified as RSGs. Only Type IIn progenitors have been claimed as high mass LBV stars, e.g. SN2009ip (Mauerhan et al. 2013) and SN2005gl (Gal-Yam et al. 2007) with M > 50 M$_\odot$. The figure shows also the only claimed Type Ib progenitor identification of iPTF13bvn (section 1.3.2) whose physical nature is still under debate. The blue box marks the expected region of Type Ib,c progenitors if the WR hypothesis is right (image: Smartt 2015).

1.3.2 Type Ib/c Progenitors

While the direct search for progenitors in pre-explosion images has been successful for Type IIP SNe, the method produced very elusive results for Type Ib,c SNe.

There is only one claimed progenitor identification for the Type Ib SN iPTF13bvn (Cao et al. 2013). The pre-explosion data obtained from Hubble Space Telescope indicate a blue progenitor star. The nature of the star is still under debate: Cao et al. (2013) and Groh et al. (2013) proposed an initial 30 M$_\odot$ single star evolved to a WN star. Bersten et al. (2014) and Eldridge et al. (2015) proposed binary systems with 20 + 19 M$_\odot$ and 10 + 8 M$_\odot$ components, respectively. From post-SN imaging (Folatelli et al. 2016) it is known that the pre-SN flux in archival images is due to the progenitor rather than any companion. Thus different work supports different progenitor scenarios and further work is required to reveal the nature of the progenitor definitively.
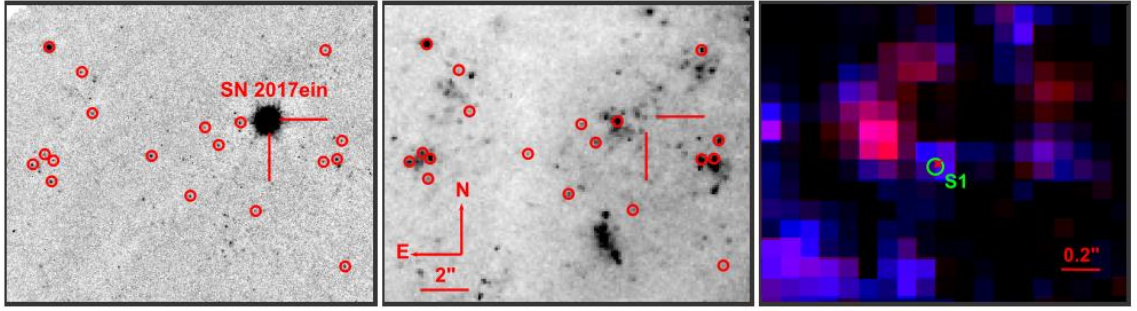
Figure 1-13: Claimed progenitor of Type Ic SN2017ein. Left image is the Keck OSIRIS H-band image of SN2017ein with circled point sources for astrometry. Middle image is the Hubble WFPC2 F814W reference image for astrometry and right is the zoomed F555W/F814W composite of the Hubble/WFPC2 image at the position of SN2017ein (image: Kilpatrick et al. 2018).

Recently, Kilpatrick et al. (2018) and Van Dyk et al. (2018) claimed the first identified candidate of a Type Ic progenitor of SN2017ein (Figure 1-13). First estimations point to a highly massive star (~55 $M_\odot$) or a very massive binary system. Further observations are required to constrain the candidate.

The most extensive search for Type Ib,c progenitors in pre-explosion images has been presented by Eldridge et al. (2013). The analysis of images for progenitors of 14 Type Ib,c SNe revealed no detections.

The lack of direct detections of Type Ib,c progenitors triggered the research by indirect methods to constrain Type Ib,c progenitors. One constraint can be derived from the relatively high rate of Type Ib,c SNe: Smith et al. (2011) looked at the number distribution of SNe in the context of an initial stellar mass function (see e.g. Bastian et al. 2010 for a review) and found that the SNe rate does not meet the expected rate, if Type Ib,c progenitors are massive single stars: The population of massive stars, derived from the initial stellar mass function, does not fit the observed number of SNe of the different subtypes if they would be created just from massive single stars.

This is supported by the larger number of observed Type Ic SNe compared with the number of Type Ib SNe (see Figure 1-3). The single massive star progenitor scenario for Type Ib,c SNe predicts an inverse number ratio: higher mass stars (Type Ic progenitors) are less frequent than lower mass stars (Type Ib progenitors) according to the initial stellar mass function.

A second constraint comes from light curve modelling which points to typical ejecta masses of 1-4 $M_\odot$ (e.g. Eldridge et al. 2013) that is too low for estimated final masses of WR stars of 8 to 20 $M_\odot$ (e.g. Crowther 2007).

Further constraints have been derived from the positions of Type Ib,c SNe within their host galaxies. Anderson et al. (2012) found that Type Ib,c SNe are more closely associated with star forming regions than Type II SNe. This has essentially been confirmed by a study of Crowther (2013) and the conclusion is that Type Ib,c seems to come from younger populations than the majority of Type II progenitors.

Many studies tried to constrain the Type Ib,c progenitors by metallicity estimations. Indirect methods based on the luminosity-metallicity relation (e.g. Arcavi et al. 2010), the extrapolation from galaxy centre metallicity (e.g. Boissier and Prantzos 2009) and the metallicity gradient (e.g. Tsvetkov et al. 2004) have been applied to constrain the progenitors. But these more globally based methods are intrinsically less accurate than methods that try to measure the metallicity at the site of the SN explosion directly. These methods are all based on spectroscopic measurements of strong emission lines (see section 1.4.3) of the HII regions where the SNe exploded. The metallicity estimation in this work relies on this method.

1.4 Metallicity Estimation of Supernovae Environments

During its short lifetime of a few millions years (e.g. Woosley et al. 2002), a massive star will essentially stay at the place of its birth. A massive star with a peculiar velocity of 20 km/s and a lifetime of 5 million years would move about 100pc, which is in the order of the size of HII regions (see Table 1-1). Thus, the metallicity of the SN progenitor star should not differ significantly from the metallicity of the surrounding HII environment and the measurement of this metallicity is a means to constrain the properties of SN progenitors. A number of methods have been developed for such metallicity estimations.

1.4.1 Indirect Methods

Indirect methods of metallicity estimation use properties of the host galaxy to evaluate the metallicity of the SN environment. Such methods are not as accurate as direct measurements at the SN site. But they have the advantage of less observational effort and are often the only way for distant SNe, for which the explosion site could not be resolved.

The most important indirect methods for metallicity estimation are: mass-metallicity relation, luminosity-metallicity relation (both relations e.g. Tremonti et al. 2004) and metallicity gradient (e.g. Henry and Worthey 1999). Mass-metallicity and luminosity-

metallicity are closely related and evaluate the metallicity of the SN site just by a global property of the host galaxy. They are both very inaccurate. A slight improvement can be made by estimating the metallicity via the host galaxy metallicity gradient. Additionally, the metallicity of the indirect methods represents (depending on the method) the stellar metallicity that is usually not the same as the gas phase metallicity of the HII regions.

1.4.2 Electron Temperature

The direct method for metallicity measurement - known as T_e-method - uses observed intensity ratios of emission lines to determine abundances. E.g. the abundance ratio of O^{++}/H^+ ions is given by (Stasinska 2002):

$$O^{++}/H^+ = \frac{[OIII]\lambda 5007/H\beta}{j_{[OIII]}(T_e,n)/j_{H\beta}(T_e)} \qquad \text{(Eq. 1-2)}$$

where [OIII] $\lambda 5007$ and Hß are the line intensities and j are the emission coefficients of [OIII] $\lambda 5007$ and Hβ, respectively. The emission coefficients depend on the electron temperature T_e and the density n of O^{++}. The electron temperature can be estimated by the ratio of two lines of the same element and same ionisation level but very different excitation potential (Stasinska 2002), e.g. [OIII]$\lambda 4363$ and [OIII]$\lambda 5007$.

One issue with the T_e-method is a weak, or not detectable, [OIII]$\lambda 4363$ line. For this reason, statistical methods have been proposed (e.g. Pagel et al. 1979) for metallicity measurements. These methods - known as strong emission line methods - use data of HII regions for which the relation of element line intensity and element abundance is established from a T_e-method. These data are used to derive a calibration statistically, which is applied to determine abundances in HII regions for which the T_e-method fails.

1.4.3 Strong Emission Lines

Several methods using different emission lines and calibrations have been proposed for metallicity measurements by the statistical strong emission line method. An overview of proposed calibrations is given in the paper from Kewley and Ellison (2008).

This work uses two methods proposed by Pettini and Pagel (2004). The first method, abbreviated with N2, uses the ratio of [NII]$\lambda 6583$/Hα for the metallicity measurement. A great advantage of this method is the proximity of the two lines ($\Delta\lambda = 20$ Å) that

make the method robust against observational issues like reddening or flux calibration uncertainties. The original calibration (Figure 1-14) by Pettini and Pagel (2004) between the line intensities and the oxygen abundances (in units 12 + log(O/H)) is given by:

$$PPO4\text{-}N2 = 8.90 + 0.57 \times \log\left(\frac{[\text{NII}]\lambda6583}{\text{H}\alpha}\right) \qquad \text{(Eq. 1-3)}$$

Marino et al. (2013) reviewed the calibration with new data (Figure 1-15) and derived a new calibration to (also in units 12 + log(O/H)):

$$M13\text{-}N2 = 8.743 + 0.462 \times \log\left(\frac{[\text{NII}]\lambda6583}{\text{H}\alpha}\right) \qquad \text{(Eq. 1-4)}$$

The second method, abbreviated by O3N2, applied in this work additionally uses the ratio of the emission lines [OIII]λ5007/Hβ. The original calibration (Figure 1-16) determined by Pettini and Pagel (2004) is given by:

$$PPO4\text{-}O3N2 = 8.73 - 0.32 \times \log\left(\frac{[\text{OIII}]\lambda5007/\text{H}\beta}{[\text{NII}]\lambda6583/\text{H}\alpha}\right) \qquad \text{(Eq. 1-5)}$$

The review by Marino et al. (2013) with new data updated the calibration (Figure 1-17) to:

$$M13\text{-}O3N2 = 8.533 - 0.214 \times \log\left(\frac{[\text{OIII}]\lambda5007/\text{H}\beta}{[\text{NII}]\lambda6583/\text{H}\alpha}\right) \qquad \text{(Eq. 1-6)}$$

The calibrations (Eq. 1-3) to (Eq. 1-6) are the linear fits to large numbers of measurements by the T_e-method and their uncertainties are determined by intervals given by the standard deviations σ. The widths of the 2σ intervals (95% of all measurements are within ±2σ) are given by ±0.41 dex for PP04-N2, ±0.32 dex for M13-N2, ±0.25 dex for PP04-O3N2 and ±0.32 dex for M13-O3N2 calibration. The 1σ intervals (68% of all measurements), usually used for uncertainty estimations of statistical data, are ±0.18 dex for PP04-N2, ±0.16 dex for M13-N2, ±0.14 dex for PP04-O3N2 and ±0.16 dex for M13-O3N2 calibration.
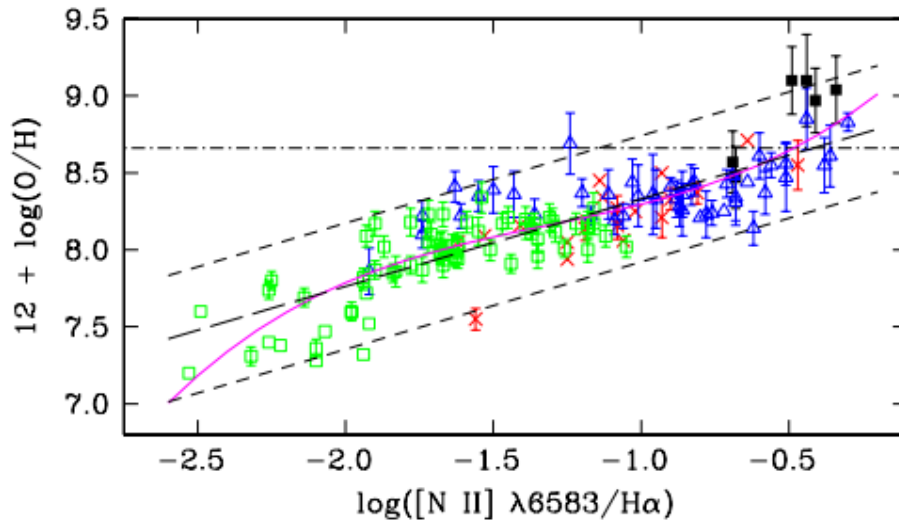
Figure 1-14: Calibration of PP04-N2 method. Oxygen abundance versus N2-index is shown. The coloured symbols are data used for the calibration. The long dashed line is the linear fit (Eq. 1-3) to the data. Short dashed lines mark the 2σ interval (95% of measurements), which is ±0.41 dex. The 1σ interval (68%) is ±0.18 dex. The magenta solid line is the best cubic fit not used in this work and the horizontal line show solar oxygen abundance 12+log(O/H) = 8.66 for comparison (image: Pettini and Pagel 2004).
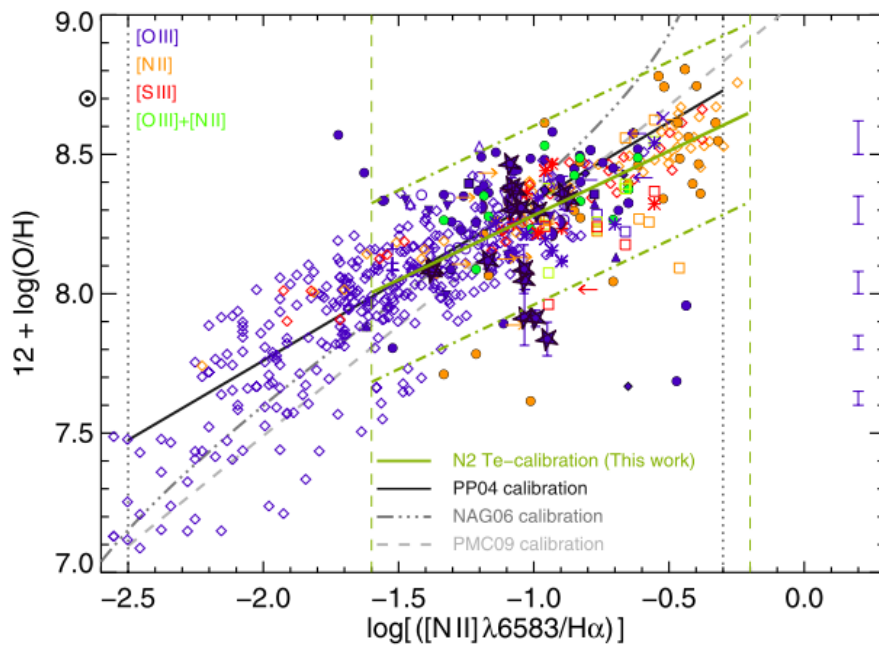
Figure 1-15: Calibration of M13-N2 method. Oxygen abundance versus N2-index is shown. The coloured symbols are data used for the calibration. The solid green line is the new best linear fit (Eq. 1-4) to the data, the black solid line is the old PP04-N2 calibration for comparison. The green dot-dashed lines mark the 2σ interval (95% of measurements), which is ±0.32 dex. The 1σ interval (68%) is ±0.16 dex. Grey lines are other calibrations not discussed in this work (image: Marino et al. 2013).
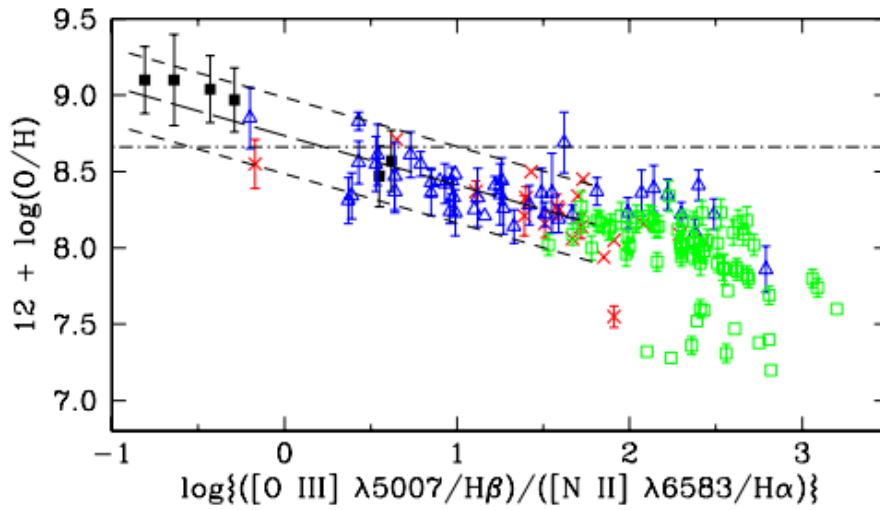
Figure 1-16: Calibration of PP04-O3N2 method (Eq. 1-5). Oxygen abundance versus O3N2-index is shown. Symbols and lines are same as for Figure 1-14. The 2σ interval (95% of measurements) is ±0.25 dex, the 1σ interval (68%) is ±0.14 dex (image: Pettini and Pagel 2004).
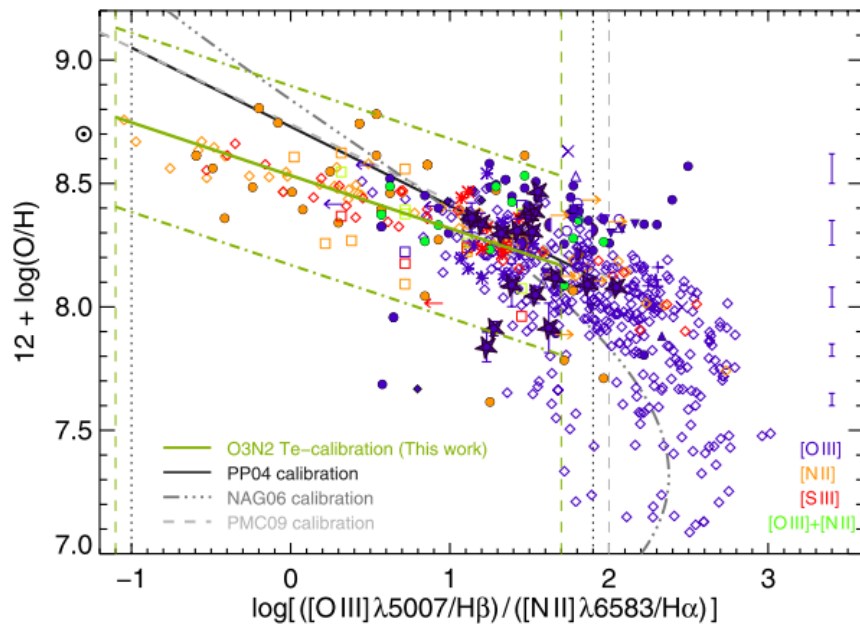
Figure 1-17: Calibration of M13-O3N2 method (Eq. 1-6). Oxygen abundance versus O3N2-index is shown. Symbols and lines are same as for Figure 1-15. The 2σ interval (95% of measurements) is ±0.32 dex, the 1σ interval (68%) is ±0.16 dex (image: Marino et al. 2013).

1.5 Previous Work

The direct metallicity measurement by strong emission lines applying N2 and/or O3N2 calibration has been used in 6 previous studies with inconclusive results. They are briefly described in this section.

Of all Type II SNe, this work uses only Type IIP SNe to obtain the environment metallicities of a SNe sample with known progenitors (see section 1.3.1) to verify the validity of the method used. The previous studies included all Type II SNe. Their progenitors are not unambiguously identified with the exception of the Type IIP SNe. The samples of the previous studies (see Table 1-3) have been reduced to Types IIP, Ib and Ic SNe therefore.

Anderson et al. (2010) was the first study using the method. They analysed spectra of HII environments of 74 core-collapse SNe (55 of them Type IIP, Ib and Ic) and found that the mean metallicity of Type Ib,c SNe environments is higher than that of all Type II environments. But statistical goodness-of-fit test shows that the two metallicity distributions may be drawn from same parent population. They conclude that the progenitor mass and/or binarity play a much more significant role for deciding the observed SN type than the metallicity.

Modjaz et al. (2011) analysed the spectra of 35 (24 of them Type IIP, Ib and Ic) low-redshift stripped envelope SN environments and found, in contrast to Anderson et al. (2010), a very low probability (1%) that the environment abundances of SN Ib and SN Ic are drawn from same parent population.

Leloudas et al. (2011) analysed the locations of 20 core-collapse SNe (15 of them Type Ib and Ic) and found an (statistically not significant) indication that Type Ic environments are more metal rich than that of Type Ib environments. They also estimated the mean stellar age for the SN environments. The results did not favour any of the two formation channels for Type Ib,c SNe (see sections 1.2.4/1.2.5).

Sanders et al. (2012) presented spectroscopic results of 58 core-collapse SNe (33 of them Type Ib and Ic) discovered exclusively by untargeted searches therefore not biased toward high mass, high metallicity host galaxies as in the previous studies. They found different median metallicities for Type Ib and Type Ic but judged the difference as not statistically significant.

Table 1-3: Sample sizes of Type IIP, Ib and Ic SNe of previous work. Given is total number N(total) of the SNe Type IIP, Ib and Ic in the samples of the studies, the number $N(D_L \leq 30 Mpc)$ of these types within a luminosity distance D_L of about 30 Mpc and the split of the ≤ 30 Mpc sample between the three SN types

Authors	N(total)	$N(D_L \leq 30$ Mpc)	Type IIP	Type Ib	Type Ic
Anderson et al. 2010	55	32	16	5	11
Modjaz et al. 2011	24	8	1	4	3
Leloudas et al. 2011	15	3	0	3	0
Sanders et al. 2012	33	1	0	1	0
Galbany et al. 2016	26	12	6	3	3
Kuncarayakti et al. 2018	51	49	29	9	11
This work	110	110	65	21	24

Galbany et al. (2016) used targeted search integral field spectroscopy data of the CALIFA survey to evaluate the metallicity of nearby host galaxies of 74 core-collapse SNe (26 of them Type IIP, Ib and Ic). They confirmed the bias toward higher host masses and metallicities in targeted SN searches. The analysis of combined data of targeted and untargeted searches revealed highest metallicities for Type Ic and Type II which is unexpected given the confirmed lower-mass progenitors of Type II SNe. They found Type II and Ic metallicities significantly higher than for Type Ib SNe which would suggest a binary evolutionary scenario for Type Ib.

Kuncarayakti et al. (2018) analysed integral field spectroscopy data of 83 SNe (51 of them Type IIP, Ib and Ic) explosion sites with a median distance of 18 Mpc. In addition to the metallicity they derived the initial progenitor mass from the estimation of the progenitor age. They used the Hα equivalent width method as age indicator (the emission of Hα declines with increasing age of a stellar population) and estimated the age by best fitting to simple stellar population models. They found no significant metallicity differences for the different core-collapse SN types. The progenitor mass has been found the highest for Type Ic, followed by Type Ib and then Type II SN consistent with the single massive star scenario.

New studies have been published during the runtime of the project: Galbany et al. (2018) presented the metallicities of the environments of 234 SNe (of which 152 are core-collapse SNe) using the strong emission line method calibration by Dopita et al. (2016) that provides slightly different results than the N2 and O3N2 calibrations. The study has not been considered therefore. Most recently, Xiao et al. (2019) published metallicity data of the same observations estimated with the O3N2 calibration of Marino et al. (2013). They defined a fixed spatial size of 1 kpc^2 as environment of a SN

independent of the luminosity distance. Especially for close host galaxies the results are not comparable with the long-slit spectroscopy results of this work.

1.6 Motivation and Thesis Structure

Previous studies were often based on small samples (Table 1-3) drawn from SN catalogues, were potentially biased to searches targeting high metallicity galaxies, included SNe with poor classifications and used relatively high-z SNe increasing the metallicity uncertainty of the SN site because of reduced spatial resolution.

This work aims to address these issues. It estimates the metallicities for a large sample (see Table 2-1) of carefully selected core-collapse SNe environments by the strong emission line method. The differences of metallicities will be checked for statistical significance for different parent populations of the different SNe types. The large number of targets improves the statistical reliability of the results compared with previous work. Further improvement of the statistical reliability will be achieved by supplementing the sample with suitable targets from previous work meeting the selection criteria.

The thesis is structured as follows. Chapter 2 presents the instrumentation and all observations of the selected targets. Chapter 3 describes the data reduction process to obtain the spectrum at SN site from the raw long-slit spectra. Chapter 4 presents the measured metallicities, along with their uncertainties, as well as the statistical goodness-of-fit tests. Discussion of the results is the content of chapter 5.

Chapter 2

Observations

This work is based on long-slit spectra of the host HII regions where the core-collapse SNe exploded. This section presents all of the observational conditions to obtain the data. It starts with the criteria of target selection, followed by a section documenting the instrumentation and technical parameters used to obtain the frames, and finally presenting the lists of the observed targets.

2.1 Target Selection

A sample of 110 SNe has been selected for the project (Table 2-1). It consists of 22 Type Ib, 23 Type Ic and 65 IIP SNe distributed over both hemispheres (Figure 2-1).
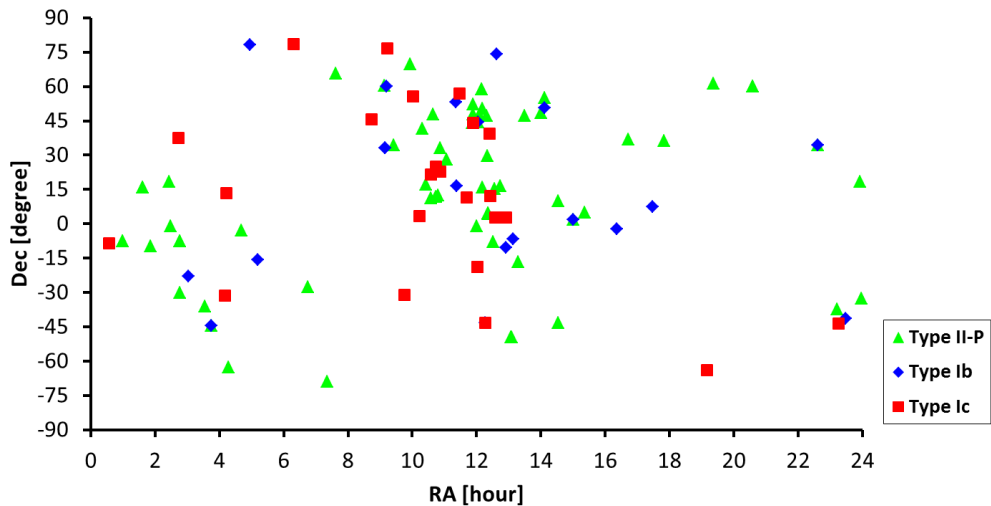
Figure 2-1: Distribution of the SNe sample. With 110 SNe, all within 30 Mpc, the sample is larger than in previous studies (see section1.5).

The SNe have been selected by the following criteria:

- Luminosity distance less than about 30 Mpc. In order to get an appropriate spatial resolution and to avoid greater uncertainties of true local metallicity at higher redshifts.

- Reliable spectral SN classification to avoid any skew in any way by ambiguous classifications.

- The host galaxy should have sufficiently low inclination ($<75°$) to avoid ambiguities of the SN HII region identification and to avoid issues with emission lines detection by high host extinction.

The realisation of the target list according to the criteria above suffers the large uncertainties of astronomical quantities, limiting the strict application of the criteria. Additionally, the number of SNe within 30 Mpc is limited. The strict application of the criteria reduces the number of the remaining targets to a sample size with small statistical significance. Consequently, there must be compromises in the application of the selection criteria and Table 2-1 has been compiled by following approach:

- SNe with luminosity distances up to 33 Mpc have been taken from Open Supernova Catalogue[4] (Guillochon et al. 2017). All SNe up to 27 Mpc have been accepted as target candidate. The luminosity distances of SNe between 27 Mpc and 33 Mpc have been checked for additional distance measurements in the NASA/IPAC Extragalactic Database (NED[5]) and accepted as candidate if there are distances <30 Mpc reported.

- The classifications of the SNe have been taken from Open Supernova Catalogue. All SNe with clear Type Ib, Type Ic and Type IIP have been accepted as candidate. SNe with ambiguous classification as 'Type Ib/c' or just 'Type II' have been checked for the references given in the Open Supernova Catalogue and accepted as candidate if the majority of references claimed Type Ib, Type Ic or Type IIP. Additionally, SNe older than 1990 have been excluded because of uncertainties of the instrumentation and the classification method used; SNe younger than 2017 have been excluded to avoid a potential contamination of the HII region by (residual) light of the SN event itself.

---

[4] https://sne.space/
[5] http://ned.ipac.caltech.edu/

- The inclinations of the host galaxies have been taken from Hyperleda[6]. The inclination of the host galaxy is the weakest criterion. The light of a SN environment in the outskirts of a high inclination galaxy may be less contaminated by stellar radiation as the light of a SN environment close to the centre of a low inclination galaxy. Thus, all SNe in hosts with inclination <75° have been accepted as candidate and SNe in hosts with an inclination >75 have been decided case by case.

The approach above provides 40 Type Ib, 39 Type Ic and 107 Type IIP candidates of which 110 targets have been selected in Table 2-1 taking into account foreseeable observation opportunities and the runtime of the project. The table represents a completeness of about 60% of all selected candidates.

Table 2-1: List of targets and morphology, luminosity distance D_L, radial velocity v_r, absolute magnitude M_V and redshift of their host galaxies. Morphology, radial velocity, absolute magnitude and redshift are taken from NED, SN type and luminosity distance taken from Open Supernova Catalogue. List authors: J.Pledger, S.Habergham-Mawson, A.Brocklebank and R.Ganss

SN	SN type	galaxy	morphology	D_L [Mpc]	v_r [km/s]	M_V	redshift
1998bv	IIP	HS1035+4758	?	23.4	1802	-16.0	0.00530
1998dl	IIP	NGC1084	SA(s)c	16.7	1196	-21.8	0.00469
1999eh	Ib	NGC2770	SA(s)c	26.0	1947	-21.7	0.00649
1999em	IIP	NGC1637	SAB(rs)c	7.7	717	-20.6	0.00239
1999ev	IIP	NGC4274	SB(r)ab	21.0	930	-21.7	0.00310
1999gi	IIP	NGC3184	SAB(rs)cd	11.0	592	-21.0	0.00198
1999gn	IIP	NGC4303	SAB(rs)bc	14.0	1566	-21.8	0.00522
1999gq	IIP	NGC4523	SAB(s)m	6.0	262	-17.5	0.00087
2000db	IIP	NGC3949	SA(s)bc	15.7	800	-21.1	0.00267
2000ds	Ib	NGC2768	E6	17.0	1353	-21.7	0.00451
2000ew	Ic	NGC3810	SA(rs)c	16.0	992	-21.4	0.00331
2001B	Ib	IC391	SA(s)c	25.0	1507	-20.4	0.00519
2001ci	Ic	NGC3079	SB(s)c	15.0	1116	-22.1	0.00372
2001du	IIP	NGC1365	SB(s)b	17.2	1636	-23.0	0.00546
2001fv	IIP	NGC3512	SAB(rs)c	25.0	1376	-20.5	0.00459
2001fz	IIP	NGC2280	SA(s)cd	14.0	1899	-22.1	0.00633
2001X	IIP	NGC5921	SB(r)bc	19.3	1480	-21.1	0.00494
2002hh	IIP	NGC6946	SAB(rs)cd	4.7	40	-14.8	0.00013
2002ji	Ib	NGC3655	SA(s)c	26.0	1473	-21.7	0.00491
2002jz	Ic	UGC2984	SBdm	22.9	1543	?	0.00515
2003B	IIP	NGC1097	SB(s)b	25.0	1105	-23.0	0.00424
2003bg	Ic	ESO420-G09	SB(s)c	20.3	1308	-18.6	0.00456
2003gd	IIP	NGC628	SA(s)c	3.4	657	-20.4	0.00219
2003hn	IIP	NGC1448	SAcd	15.0	1168	-22.0	0.00390
2003ie	IIP	NGC4051	SAB(rs)bc	13.0	700	-21.3	0.00234
2003J	IIP	NGC4157	SAB(s)b	15.7	774	-22.0	0.00258
2003jg	Ic	NGC2997	SAB(rs)c	8.0	1089	-20.9	0.00363

SN	SN type	galaxy	morphology	D$_L$ [Mpc]	v$_r$ [km/s]	M$_V$	redshift
2003Z	IIP	NGC2742	SA(s)c	20.0	1289	-21.6	0.00430
2004A	IIP	NGC6207	SA(s)c	20.0	852	-20.5	0.00284
2004am	IIP	NGC3034	I0	3.1	203	-20.1	0.00068
2004ao	Ib	UGC10862	SB(rs)c	26.0	1691	-19.1	0.00564
2004bm	Ic	NGC3437	SAB(rs)c	21.0	1283	-21.3	0.00428
2004C	Ic	NGC3683	SB(s)c	35.0	1716	-20.8	0.00572
2004cm	IIP	NGC5486	SA(s)m	25.0	1390	-19.0	0.00464
2004cz	IIP	ESO407-G09	SB(s)d	21.0	1296	-19.6	0.00521
2004dg	IIP	NGC5806	SAB(s)b	22.0	1359	-22.0	0.00453
2004dj	IIP	NGC2403	SAB(s)cd	3.5	133	-19.4	0.00044
2004dk	Ib	NGC6118	SA(s)cd	20.0	1573	-21.8	0.00525
2004et	IIP	NGC6946	SAB(rs)cd	4.7	40	-14.8	0.00013
2004ez	IIP	NGC3430	SAB(rs)c	26.0	1586	-21.7	0.00529
2004fc	IIP	NGC701	SB(rs)c	19.0	1831	-20.9	0.00611
2004gk	Ic	IC3311	Sdm	17.0	210	-18.3	-0.00041
2004gn	Ic	NGC4527	SAB(s)bc	12.6	1736	-20.7	0.00579
2004gq	Ib	NGC1832	SB(r)bc	16.0	1939	-21.7	0.00647
2004gt	Ic	NGC4038	SB(s)m	16.0	1642	-21.8	0.00548
2005ad	IIP	NGC941	SAB(rs)c	20.0	1608	-19.1	0.00536
2005af	IIP	NGC4945	SB(s)cd	3.4	563	-20.5	0.00188
2005at	Ic	NGC6744	SAB(r)bc	7.3	841	-21.8	0.00281
2005ay	IIP	NGC3938	SA(s)c	18.0	809	-20.7	0.00270
2005cs	IIP	NGC5194	SA(s)bc	6.1	463	-20.9	0.00154
2005cz	Ib	NGC4589	E2	20.0	1980	-21.6	0.00660
2005kl	Ic	NGC4369	SA(rs)a	21.0	1045	-21.1	0.00349
2005V	Ib/c	NGC2146	SB(s)ab	17.0	893	-22.1	0.00298
2006bc	IIP	NGC2397	SB(s)b	20.0	1363	-21.7	0.00455
2006bp	IIP	NGC3953	SB(r)bc	17.0	1052	-22.3	0.00351
2006my	IIP	NGC4651	SA(rs)c	19.0	788	-22.1	0.00263
2006ov	IIP	NGC4303	SAB(rs)bc	14.0	1566	-21.8	0.00522
2007aa	IIP	NGC4030	SA(s)bc	23.0	1465	-22.3	0.00489
2007av	IIP	NGC3279	Sd	29.0	1394	-21.8	0.00465
2007C	Ib	NGC4981	SAB(r)bc	21.0	1680	-21.5	0.00560
2007gr	Ic	NGC1058	SA(rs)c	10.0	314	-17.5	0.00173
2007od	IIP	UGC12846	Sm	24.0	1734	?	0.00578
2007Y	Ib	NGC1187	SB(r)c	18.0	1390	-21.2	0.00464
2008bk	IIP	NGC7793	SA(s)d	4.0	230	-20.0	0.00077
2008D	Ib	NGC2770	SA(s)c	26.0	1947	-21.7	0.00649
2008in	IIP	NGC4303	SAB(rs)bc	14.0	1566	-21.8	0.00522
2008X	IIP	NGC4141	SBcd	28.0	1897	-18.9	0.00633
2009E	IIP	NGC4141	SBcd	28.0	1897	-18.9	0.00633
2009em	Ic	NGC157	SAB(rs)bc	23.0	1318	-21.7	0.00551
2009G	IIP	IC4444	SAB(rs)bc	28.9	2162	-20.2	0.00654
2009hq	IIP	NGC4152	SAB(rs)c	30.0	2167	-20.4	0.00723
2009ib	IIP	NGC1559	SB(s)cd	14.0	1304	-21.3	0.00435
2009js	IIP	NGC918	SAB(rs)c	16.0	1507	-21.4	0.00503
2009md	IIP	NGC3389	SA(s)c	18.0	1308	-20.9	0.00436
2009N	IIP	NGC4487	SAB(rs)cd	18.0	1036	-19.8	0.00346

SN	SN type	galaxy	morphology	D_L [Mpc]	v_r [km/s]	M_V	redshift
2010br	Ib	NGC4051	SAB(rs)bc	13.0	700	-21.3	0.00234
2010io	Ic	UGC4543	SAdm	29.0	1960	-18.5	0.00654
2011am	Ib	NGC4219	SA(s)bc	29.4	1989	-21.8	0.00664
2011ck	IIP	NGC5425	Sd	30.7	2074	-19.2	0.00692
2011dq	IIP	NGC337	SB(s)d	24.4	1646	-21.1	0.00549
2011hp	Ic	NGC4219	SA(s)bc	29.4	1989	-21.8	0.00664
2011ja	IIP	NGC4945	SB(s)cd	3.4	563	-20.5	0.00188
2011jm	Ic	NGC4809	Im	13.8	915	-17.3	0.00305
2012A	IIP	NGC3239	IB(s)m	8.8	753	-19.7	0.00251
2012au	Ib	NGC4790	SB(rs)c	20.0	1344	-19.4	0.00448
2012aw	IIP	NGC3351	SB(r)bc	11.5	778	-21.7	0.00260
2012bv	IIP	NGC6796	Sbc	32.5	2189	-21.0	0.00730
2012cw	Ic	NGC3166	SAB(rs)a	19.9	1345	-22.6	0.00449
2012dj	Ib/c	NGC7531	SAB(r)bc	23.7	1596	-21.5	0.00532
2012ec	IIP	NGC1084	SA(s)c	16.7	1196	-21.8	0.00469
2012fh	Ic	NGC3344	SAB(r)bc	8.6	580	-20.4	0.00194
2012P	Ib/c	NGC5806	SAB(s)b	22.0	1359	-22.0	0.00453
2013ab	IIP	NGC5669	SAB(rs)d	23.6	1368	-20.5	0.00456
2013bu	IIP	NGC7331	SA(s)bc	12.1	816	-23.0	0.00272
2013dk	Ic	NGC4038	SB(s)m	16.0	1642	-21.8	0.00548
2013ej	IIP	NGC628	SA(s)c	3.4	657	-20.4	0.00219
2013F	Ib	IC5325	SAB(rs)bc	22.0	1257	-20.6	0.00501
2013ff	Ic	NGC2748	SAbc	21.9	1476	-21.0	0.00492
2013ge	Ic	NGC3287	SB(s)d	19.3	1306	-18.4	0.00436
2014A	IIP	NGC5054	SA(s)bc	27.0	1742	-21.4	0.00581
2014bc	IIP	NGC4258	SAB(s)bc	6.6	448	-21.9	0.00149
2014bi	IIP	NGC4096	SAB(rs)c	8.3	566	-21.1	0.00189
2014C	Ib	NGC7331	SA(s)bc	12.1	816	-23.0	0.00272
2014cx	IIP	NGC337	SB(s)d	24.4	1646	-21.1	0.00549
2014df	Ib	NGC1448	SAcd	15.0	1168	-22.0	0.00390
2015aq	IIP	UGC5015	SABdm	24.0	1650	-18.5	0.00550
2015V	IIP	UGC11000	S?	20.3	1369	-18.5	0.00457
2016bau	Ib	NGC3631	SA(s)c	17.1	1156	-19.5	0.00386
2017ein	Ic	NGC3938	SA(s)c	18.0	809	-20.7	0.00270
2017iro	Ib	NGC5480	SA(s)c	27.5	1856	-21.3	0.00619

All but two targets in Table 2-1 are hosted by late-type galaxies. The two exceptions are the Ca-rich transients SN2000ds and SN2005cz (Perets et al. 2010). Their hosts NGC2768 and NGC4589, respectively, show evidence of recent star formation (Suh et al. 2011) explaining the presence of a core-collapse SNe in an early-type galaxy.

primary mirror:[1]	2540 mm
focus:[1]	Cassegrain (f/15)
pointing accuracy:[2]	5 arcsec
guiding accuracy:[2]	0.3 arcsec
camera:	235 mm camera
detector:	EEV10
pixel size:[3]	13.5 µm
spectrograph:	IDS
scale factor:[3]	0.4 arcsec/px
slit length:[4]	3.3 arcmin

Figure 2-2: Isaac Newton Telescope on La Palma (image: R.Ganss) and the most important data of the technical configuration used for all observations (references: 1: INT optics[9], 2: Laing and Jones 1985, 3: INT EEV10[10], 4: INT IDS[11]).

2.2 Instrumentation

The initial project plan intended observations at the Isaac Newton Telescope (INT) (Figure 2-2) on La Palma and at the New Technology Telescope (NTT) in Chile. Unfortunately, available observation data obtained at NTT in 2016 (observer: S. Habergham-Mawson) used a slightly different approach for the observations (slit covered the closest HII region instead the coordinates of the SN as done for the INT observations). Other NTT observation data for the strong emission method could not be obtained during the runtime of the project. Thus, all observation data presented in this thesis are obtained from INT with the technological configuration listed in Figure 2-2.

The observations made use of the IDS spectrograph at the INT. Figure 2-3 schematically shows the construction of a grating spectrograph like the IDS: the collected light entrances the spectrograph through the slit. The collimating mirror parallelises the light and directs it to the diffraction grating that performs the dispersion of the incoming light. The focusing mirror collects the dispersed light and directs it to the CCD detector.

The most important part of the spectrograph determining the optical performance is the diffraction grating. The IDS has 16 different gratings (IDS gratings[12]) of which the grating R400V has been used for the observations. Table 2-2 shows the used technical configuration data of the IDS in combination with EEV10 detector used for the observations.

---

[9] http://www.ing.iac.es/Astronomy/telescopes/int/intoptics.html
[10] http://www.ing.iac.es/Engineering/detectors/ultra_eev10a.htm
[11] http://www.ing.iac.es/astronomy/instruments/ids/ids_eev10.html
[12] http://www.ing.iac.es/astronomy/instruments/ids/idsgrat_tables.html
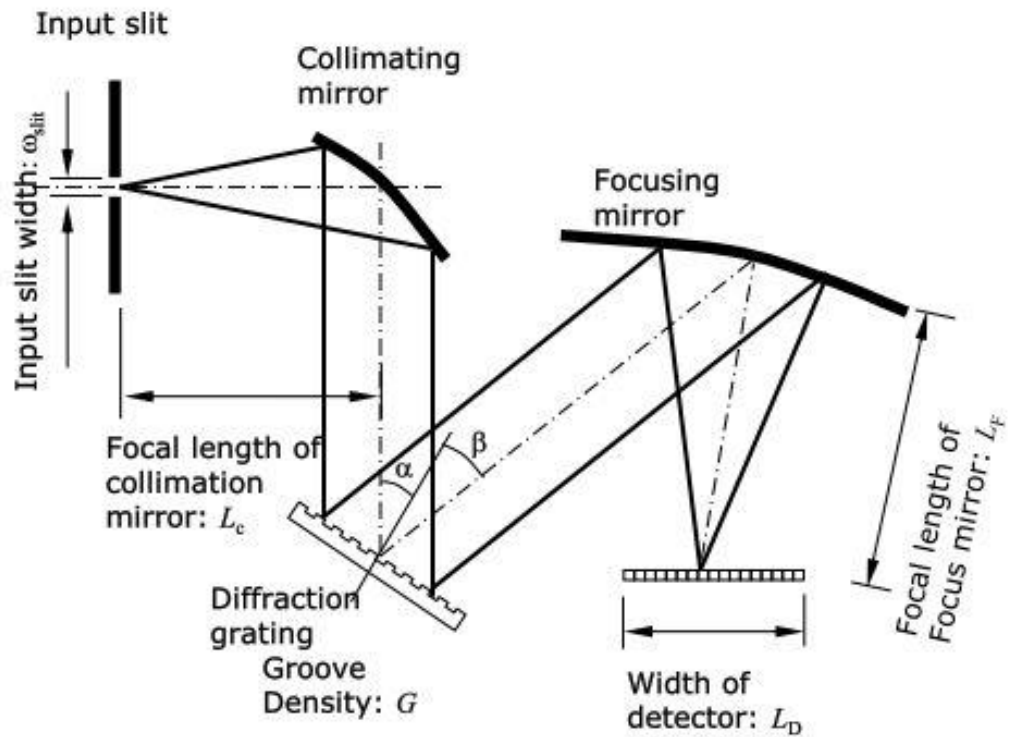
Figure 2-3: Schematic construction of a spectrograph using a diffraction grating (image: Ibsen photonics[13])

Table 2-2: Technical configuration of IDS/EEV10 equipment for taking calibration and science frames. See Figure 2-2 for additional technical data of instrumentation.

slit width	1.5 arcsec
grating	R400V
central wavelength[*]	5802.4 Å
dispersion[1]	1.41 Å/px
resolution ($\lambda/\Delta\lambda$)[1]	1596@4500 Å
readout window[**]	x=740:1235; y=1:4200
frame size[**]	496px × 4200px
readout speed	slow
linearity[2]	±0.2% to 65535 ADU
saturation level[3]	65535 ADU
dark current[2]	4 e/hour @ 153 K
filters	clear
gain factor[3]	1.2 electrons/ADU

[*]slightly different central wavelength for 27-Sep-2016 (5810.7Å) and 18-Feb, 30-Oct, 26 Nov 2018 (5794.2Å)

[**]reduced readout window (785:1150,1:4200) for 26-Nov-2018, 21-Feb-2019 and 22-Feb-2019 resulting in smaller frame size of 366px × 4200px

1: IDS gratings; 2: INT EEV10; 3:FITS file header

Table 2-3: Overview of INT observations. Five observation periods (abbreviated by 'int1' to 'int5') contribute to the project.

name	year	nights	#nights	#observations	INT proposal ID
int1	2016	27-Sep to 01-Oct	5	28	I/2016B/05
int2	2017	27-Dec and 28-Dec	2*	14	I/2017B/01
int3	2018	18-Feb, 13-Jun, 30-Oct, 26-Nov	4	8	SI2018a02**
int4	2019	21-Feb and 22-Feb	2	10	SI2018a02**
int5	2019	23-Feb to 28-Feb	6	39	I/2019A/01

*8 nights were allocated but the run was hindered by technical fault with the telescope for the first 6 nights.
**Director time allocated as payback for 2017B run.

2.3 Observation Data

2.3.1 Overview

Observation data of five observation periods at INT are available for the project (Table 2-3). In total 96 target observations have been obtained over 19 observation nights. Some targets have been observed twice (10 targets) or three times (3 targets) to get an improved signal-to-noise ratio (SNR) by better observation conditions, to have more frames for combining and to check flux calibration between runs.

Taking into account the multiple target observations, data of 80 targets are available for evaluation. This number includes 4 targets (SN1990aa, SN1991ar, SN1996D and SN2009ga) observed by opportunity and not part of the selected target sample (Table 2-1). The data of these targets have been reduced and evaluated but they are not incorporated in the statistical evaluation in chapter 4 because the luminosity distance is significantly larger than 30 Mpc (lower uncertainty range limit >40 Mpc).

2.3.2 Calibration Frames

The quantitative evaluation of scientific frames requires calibration frames for quantitative scaling of the obtained frames and to reduce impacts by atmospheric conditions and imperfections of the optical signal path. This sub-section only documents the technical parameters relating to how the calibration frames are taken; the usage of the calibration frames is described in chapter 3.

Bias frames to remove the bias signal of CCD and electronics were taken with closed shutter at zero second exposure time. For every night two bias frame blocks (one in the evening, one in the morning) were taken with 6-11 frames each.

Table 2-4: List of spectrometric standards used for flux calibration.

name	reference	nights
SP0305+261	Oke and Gunn 1983	30-Oct-2018
SP0401+250	Oke 1974	24to26-Oct-2019
SP0501+527	Oke 1974	27to30-Sep-2016, 01-Oct-2016
SP0644+375	Oke 1974	18-Feb-2018, 30-Oct-2018, 21&22-Feb-2019, 27-Feb-2019
SP0856+331	Oke 1974	28-Feb-2019
SP1134+300	Oke 1974	27&28-Dec-2017
SP1234+254	Massey et al 1988	27&28-Feb-2019
SP1409+503	Stone 1977	23-Feb-2019
SP1436+277	Stone 1977	13-Jun-2018, 24to26-Feb-2019
SP1550+330	Stone 1977	22-Feb-2019
SP1626+368	Oke 1974	21-Feb-2019
SP2148+286	Massey et al 1988	27to30-Sep-2016, 01-Oct-2016, 26-Nov-2018
SP2341+322	Oke 1974	27&28-Dec-2017

Flat frames, created by uniform illumination of the slit by a dome tungsten lamp, were taken with two blocks (6-11 frames each) per night also. The exposure time of flat frames must be sufficiently short to avoid saturation and was typically 3 seconds.

Arc frames for wavelength calibration were obtained by illuminating the slit with CuAr+CuNe arc lamps with typical exposure time of 20s. Two arc frames for each target were taken with same optical configuration (Table 2-2) and position angle (PA) as the corresponding target observations.

Standard star observations for flux calibration were obtained at least two per night. The standard stars (Table 2-4) were chosen from the ING spectrometric standards[14] catalogue depending on time of observation. The number of spectrometric standard star frames varied from 1 to 3 per observation with exposure times from 20s to a few 100s depending on standard star magnitude. Typical slit width for standard star observation was 1.5" with some additional observations with 4" slit in case of bad seeing conditions. For all standard star observations appropriate arc frames have been recorded.

In addition to the calibration frames above, the acquisition images of most targets (some images of Sep 2016 observations were not taken) were saved to help determine the orientation of the slit. The acquisition images were taken by the IDS-AG0[15] acquisition camera with exposure times from 10s to a few 100s.

[14] http://catserver.ing.iac.es/landscape/
[15] http://www.ing.iac.es/Astronomy/telescopes/int/ccdorient.html

2.3.3 Scientific Frames

The 96 INT target observations are listed in Table 2-5 to Table 2-8, one table for each proposal ID. In order to remove cosmic ray hits, it was aimed to take three frames for every target observation, which worked for all but three targets. The exposure time was usually 1200s per frame increased for faint targets and/or high sky brightness conditions up to 1800s per frame. Seeing conditions were between 0.8" to 1.2" for all observation nights.

The optical configuration for all scientific frames is listed in Table 2-2. Three director's time nights used a reduced readout window (366px × 4200px) resulting in a spatial coverage of 2.44 arcmin compared to the normal spatial extent of 3.3 arcmin.

Table 2-5: INT observations in September 2016 (proposal I/2016B/05). The columns of the table are target name, SN type of target, target coordinates, name of host galaxy, position angle PA of SN relative to host centre, angular distance from host centre to SN site, night of observation and the total exposure time. Observers: P. James, S. Percival, A. Brocklebank.

target	type	SN RA	SN Dec	host	PA [°]	angular distance ["]	night	total exp. time [sec]
1990aa	Ic	00 52 59.22	+29 01 48.3	UGC540	125.8	65.52	30-Sep-2016	3600
1991ar	Ib	00 43 56.71	+01 51 13.5	IC49	36.2	15.49	29-Sep-2016	3600
1995bb	Ib/c	00 16 17.64	+12 24 53.4	A001617 +1224	87.6	9.38	29-Sep-2016	4800
1996D	Ic	04 34 00.30	-08 34 44.0	NGC1614	90.0	7.42	27-Sep-2016	2400
2001B	Ib	04 57 19.24	+78 11 16.5	IC391	238.5	6.70	30-Sep-2016	3600
2002hh	IIP	20 34 44.29	+60 07 19.0	NGC6946	207.5	129.63	29-Sep-2016	3600
2002jz	Ic	04 13 12.52	+13 25 07.3	UGC2984	197.5	3.88	28-Sep-2016	3600
2003gd	IIP	01 36 42.65	+15 44 20.9	NGC628	175.6	159.57	29-Sep-2016	3600
2004ao	Ib	17 28 09.35	+07 24 55.5	UGC10862	165.3	26.36	29-Sep-2016	3600
2004dj	IIP	07 37 17.02	+65 35 57.8	NGC2403	94.0	159.14	30-Sep-2016	3600
2004et	IIP	20 35 25.33	+60 07 17.7	NGC6946	115.2	272.73	29-Sep-2016	3600
2004fc	IIP	01 51 03.85	-09 42 06.9	NGC701	19.4	2.23	27-Sep-2016	3600
2007gr	Ic	02 43 27.98	+37 20 44.7	NGC1058	303.1	28.75	27-Sep-2016	3600
2007od	IIP	23 55 48.68	+18 24 54.8	UGC12846	132.7	51.90	28-Sep-2016	3600
2009em	Ic	00 34 44.53	-08 23 57.6	NGC157	251.8	33.90	28-Sep-2016	3600
2009ga	IIP	23 28 26.78	+22 24 50.4	NGC7678	211.2	29.94	27-Sep-2016	4800
2009js	IIP	02 25 48.28	+18 29 25.8	NGC918	240.6	41.15	28-Sep-2016	3600
2010io	Ic	08 43 21.41	+45 44 18.0	UGC4543	333.0	8.98	29-Sep-2016	4800
2011dq	IIP	00 59 47.75	-07 34 20.5	NGC337	300.4	40.51	30-Sep-2016	3600
2012bv	IIP	19 21 30.36	+61 08 12.0	NGC6796	187.4	30.25	01-Oct-2016	4800
2012ec	IIP	02 45 59.88	-07 34 27.0	NGC1084	358.9	15.00	29-Sep-2016	3600
2013bu	IIP	22 37 02.17	+34 24 05.2	NGC7331	204.0	55.62	28-Sep-2016	4800
2013ej	IIP	01 36 48.16	+15 45 31.0	NGC628	134.1	127.87	30-Sep-2016	4800
2014cx	IIP	00 59 47.83	-07 34 18.6	NGC337	303.6	40.51	28-Sep-2016	3600
2015V	IIP	17 49 27.05	+36 08 36.0	UGC11000	142.1	8.87	30-Sep-2016	3600

Table 2-6: INT observations in December 2017 (proposal I/2017B/01). The columns of the table are target name, SN type of target, target coordinates, name of host galaxy, position angle of SN relative to host centre, angular distance from host centre to SN site, night of observation and the total exposure time. Observer: A. Sansom.

target	type	SN RA	SN Dec	host	PA	angular distance	night	total exp. time
					[°]	["]		[sec]
1999em	IIP	04 41 27.04	-02 51 45.2	NGC1637	227.0	23.76	28-Dec-2017	3600
2000ds	Ib	09 11 36.24	+60 01 42.2	NGC2768	196.5	33.17	27-Dec-2017	3600
2001B	Ib	04 57 19.24	+78 11 16.5	IC391	238.5	6.70	28-Dec-2017	3600
2001ci	Ic	10 01 57.33	+55 41 14.6	NGC3079	351.8	27.88	27-Dec-2017	3600
2002ji	Ib	11 22 53.15	+16 35 10.0	NGC3655	236.1	25.11	28-Dec-2017	3600
2004gq	Ib	05 12 04.81	-15 40 54.2	NGC1832	45.0	30.83	27-Dec-2017	3600
2005kl	Ic	12 24 35.68	+39 23 03.5	NGC4369	306.7	7.52	27-Dec-2017	4800
2005V	Ib/c	06 18 38.28	+78 21 28.8	NGC2146	24.8	4.19	27-Dec-2017	3600
2007av	IIP	10 34 43.17	+11 11 38.3	NGC3279	155.0	12.90	27-Dec-2017	3600
2007gr	Ic	02 43 27.98	+37 20 44.7	NGC1058	303.1	28.75	27-Dec-2017	3600
2008D	Ib	09 09 30.65	+33 08 20.3	NGC2770	325.3	67.27	28-Dec-2017	3600
2011jm	Ic	12 54 51.10	+02 39 14.9	NGC4809	93.8	1.50	28-Dec-2017	3600
2012cw	Ic	10 13 47.95	+03 26 02.6	NGC3166	46.3	48.65	28-Dec-2017	4800
2013ff	Ic	09 13 38.88	+76 28 10.8	NGC2748	215.6	24.84	28-Dec-2017	3600

Table 2-7: Director's time observations in 2018 and 2019 (proposal SI2018a02). The columns of the table are target name, SN type of target, target coordinates, name of host galaxy, position angle of SN relative to host centre, angular distance from host centre to SN site, night of observation and the total exposure time. Observers: T. Wilson, T. Zegmott, L. Holden, D. Nespral, T. Davison, A. de Burgos.

target	type	SN RA	SN Dec	host	PA	angular distance	night	total exp. time
					[°]	['']		[sec]
1998dl	IIP	02 46 01.47	-07 34 25.1	NGC1084	54.1	28.82	30-Oct-2018	3600
1999eh	Ib	09 09 32.67	+33 07 16.9	NGC2770	238.0	15.27	18-Feb-2018	3600
1999gi	IIP	10 18 16.66	+41 26 28.2	NGC3184	358.5	61.22	22-Feb-2019	4000
2000ds	Ib	09 11 36.24	+60 01 42.2	NGC2768	196.5	33.17	22-Feb-2019	3600
2003ie	IIP	12 03 18.15	+44 31 34.6	NGC4051	101.4	93.26	22-Feb-2019	1200
2003J	IIP	12 10 57.72	+50 28 31.8	NGC4157	242.5	71.89	21-Feb-2019	5400
2003Z	IIP	09 07 32.46	+60 29 17.5	NGC2742	346.3	32.42	21-Feb-2019	5400
2004C	Ic	11 27 29.72	+56 52 48.2	NGC3683	303.3	20.40	21-Feb-2019	3600
2004ez	IIP	10 52 15.11	+32 57 20.1	NGC3430	68.8	50.08	22-Feb-2019	4600
2004gn	Ic	12 34 12.10	+02 39 34.4	NGC4527	68.9	59.43	13-Jun-2018	3600
2005ad	IIP	02 28 29.45	-01 08 20.0	NGC941	28.3	52.23	30-Oct-2018	3600
2006bp	IIP	11 53 55.74	+52 21 09.4	NGC3953	33.9	112.49	22-Feb-2019	4000
2010br	Ib/c	12 03 10.95	+44 31 43.1	NGC4051	124.4	17.50	22-Feb-2019	4000
2011ck	IIP	14 00 46.24	+48 26 45.4	NGC5425	297.0	16.30	13-Jun-2018	3600
2013bu	IIP	22 37 02.17	+34 24 05.2	NGC7331	204.0	55.62	26-Nov-2018	3600
2013ge	Ic	10 34 48.46	+21 39 41.9	NGC3287	18.7	50.56	13-Jun-2018	2400
2014bc	IIP	12 18 57.71	+47 18 11.3	NGC4258	141.7	3.44	22-Feb-2019	4200
2014C	Ib	22 37 05.60	+34 24 31.9	NGC7331	140.6	31.19	26-Nov-2018	3600

Table 2-8: INT observations in February 2019 (proposal I/2019A/01). The columns of the table are target name, SN type of target, target coordinates, name of host galaxy, position angle of SN relative to host centre, angular distance from host centre to SN site, night of observation and the total exposure time. Observers: J. Pledger, R. Ganss, T. Davison.

target	type	SN RA	SN Dec	host	PA [°]	angular distance ["]	night	total exp. time [sec]
1998bv	IIP	10 38 25.40	+47 42 32.8	HS1035 +4758	215.8	5.18	26-Feb-2019	3600
1999ev	IIP	12 19 48.33	+29 37 22.2	NGC4274	315.6	42.29	25-Feb-2019	3600
2000ew	Ic	11 40 58.52	+11 27 55.9	NGC3810	187.5	20.27	26-Feb-2019	3600
2001B	Ib	04 57 19.24	+78 11 16.5	IC391	238.5	6.70	28-Feb-2019	3600
2001ci	Ic	10 01 57.33	+55 41 14.6	NGC3079	351.8	27.88	28-Feb-2019	3600
2001fv	IIP	11 04 01.66	+28 01 55.7	NGC3512	223.5	23.85	24-Feb-2019	4200
2002jz	Ic	04 13 12.52	+13 25 07.3	UGC2984	197.5	3.88	26-Feb-2019	3600
2004A	IIP	16 43 01.90	+36 50 12.5	NGC6207	305.7	26.59	25-Feb-2019	3600
2004ao	Ib	17 28 09.35	+07 24 55.5	UGC10862	165.3	26.36	28-Feb-2019	3600
2004bm	Ic	10 52 35.33	+22 56 05.5	NGC3437	296.1	5.69	25-Feb-2019	3600
2004dg	IIP	14 59 58.96	+01 53 25.6	NGC5806	261.0	21.85	27-Feb-2019	3600
2004dk	Ib	16 21 48.93	-02 16 17.3	NGC6118	6.6	42.99	27-Feb-2019	3600
2004gk	Ic	12 25 33.23	+12 15 40.1	IC3311	31.6	3.64	28-Feb-2019	3600
2004gn	Ic	12 34 12.10	+02 39 34.4	NGC4527	68.9	59.43	27-Feb-2019	3600
2004gt	Ic	12 01 50.37	-18 52 12.7	NGC4038	255.4	38.57	26-Feb-2019	3600
2005ay	IIP	11 52 48.07	+44 06 18.4	NGC3938	194.2	58.38	26-Feb-2019	3600
2005cs	IIP	13 29 52.78	+47 10 35.7	NGC5194	179.3	67.30	26-Feb-2019	3600
2005cz	Ib	12 37 27.85	+74 11 24.5	NGC4589	119.2	13.34	23-Feb-2019	3800
2007aa	IIP	12 00 27.69	-01 04 51.6	NGC4030	41.9	91.88	27-Feb-2019	3600
2007av	IIP	10 34 43.17	+11 11 38.3	NGC3279	155.0	12.90	25-Feb-2019	4200
2007C	Ib	13 08 49.30	-06 47 01.0	NGC4981	157.9	23.75	24-Feb-2019	4200
2007gr	Ic	02 43 27.98	+37 20 44.7	NGC1058	303.1	28.75	27-Feb-2019	3600
2008D	Ib	09 09 30.65	+33 08 20.3	NGC2770	325.3	67.27	24-Feb-2019	4200
2008X	IIP	12 09 48.33	+58 51 01.6	NGC4141	60.1	9.22	28-Feb-2019	3600
2010io	Ic	08 43 21.41	+45 44 18.0	UGC4543	333.0	8.98	27-Feb-2019	3600
2012A	IIP	10 25 07.39	+17 09 14.6	NGC3239	133.9	49.57	24-Feb-2019	4200
2012au	Ib	12 54 52.18	-10 14 50.2	NGC4790	66.5	4.51	24-Feb-2019	4200
2012cw	Ic	10 13 47.95	+03 26 02.6	NGC3166	46.3	48.65	26-Feb-2019	3600
2012fh	Ic	10 43 34.05	+24 53 29.0	NGC3344	160.1	118.03	23-Feb-2019	4200
2012P	Ib/c	14 59 59.12	+01 53 24.4	NGC5806	256.5	19.73	25-Feb-2019	4000
2013ab	IIP	14 32 44.49	+09 53 12.3	NGC5669	133.1	20.04	25-Feb-2019	3600
2013dk	Ic	12 01 52.72	-18 52 18.3	NGC4038	194.6	15.81	23-Feb-2019	4200
2013ge	Ic	10 34 48.46	+21 39 41.9	NGC3287	18.7	50.56	23-Feb-2019	4200
2014A	IIP	13 16 59.36	-16 37 57.0	NGC5054	57.1	14.72	28-Feb-2019	3600
2014bi	IIP	12 06 02.99	+47 29 33.5	NGC4096	20.4	54.95	25-Feb-2019	4200
2015aq	IIP	09 25 44.53	+34 16 36.1	UGC5015	267.5	43.05	24-Feb-2019	4200
2016bau	Ib	11:20:59.00	+53:10:25.6	NGC3631	293.5	37.95	27-Feb-2019	3600
2017ein	Ic	11:52:53.25	+44:07:26.2	NGC3938	74.2	42.53	28-Feb-2019	3600
2017iro	Ib	14:06:23.11	+50:43:20.2	NGC5480	125.0	17.74	27-Feb-2019	3600

Chapter 3

Data Reduction

The observation data obtained from the telescope must be processed for removing signatures introduced by the instrument itself and observational conditions. Additionally, wavelength and flux of obtained data have to be calibrated for quantitative evaluation. Well proven tools are available to support the data reduction steps but the process itself must always be fitted to the particular conditions of instrument and scientific project.

This section describes the data reduction flow used in this project from raw data as provided from telescope to final estimation of metallicities at SN sites. The first part deals with the 2-dimensional (2D) reduction steps providing cleaned and calibrated 2D long-slit spectra. The second part describes all 1-dimensional (1D) reduction steps done to gain the metallicities of SNe sites finally.

3.1 Data Reduction Flow 2D

The 2D data reduction makes use of two proven major astronomical software packages: IRAF (Image Reduction and Analysis Facility) written at the National Optical Astronomy Observatory (Tody 1986) and Starlink written by UK astronomers (Currie et al. 2014)

The 2D data reduction process consists of following steps (Figure 3-1): bias subtraction, flat correction, rotation and trimming, S-distortion correction, wavelength calibration, sky subtraction, flux calibration and finally frame combining. CCD dark current

39

correction is negligible because of CCD cooling. Details of the single reduction steps are described subsequently.
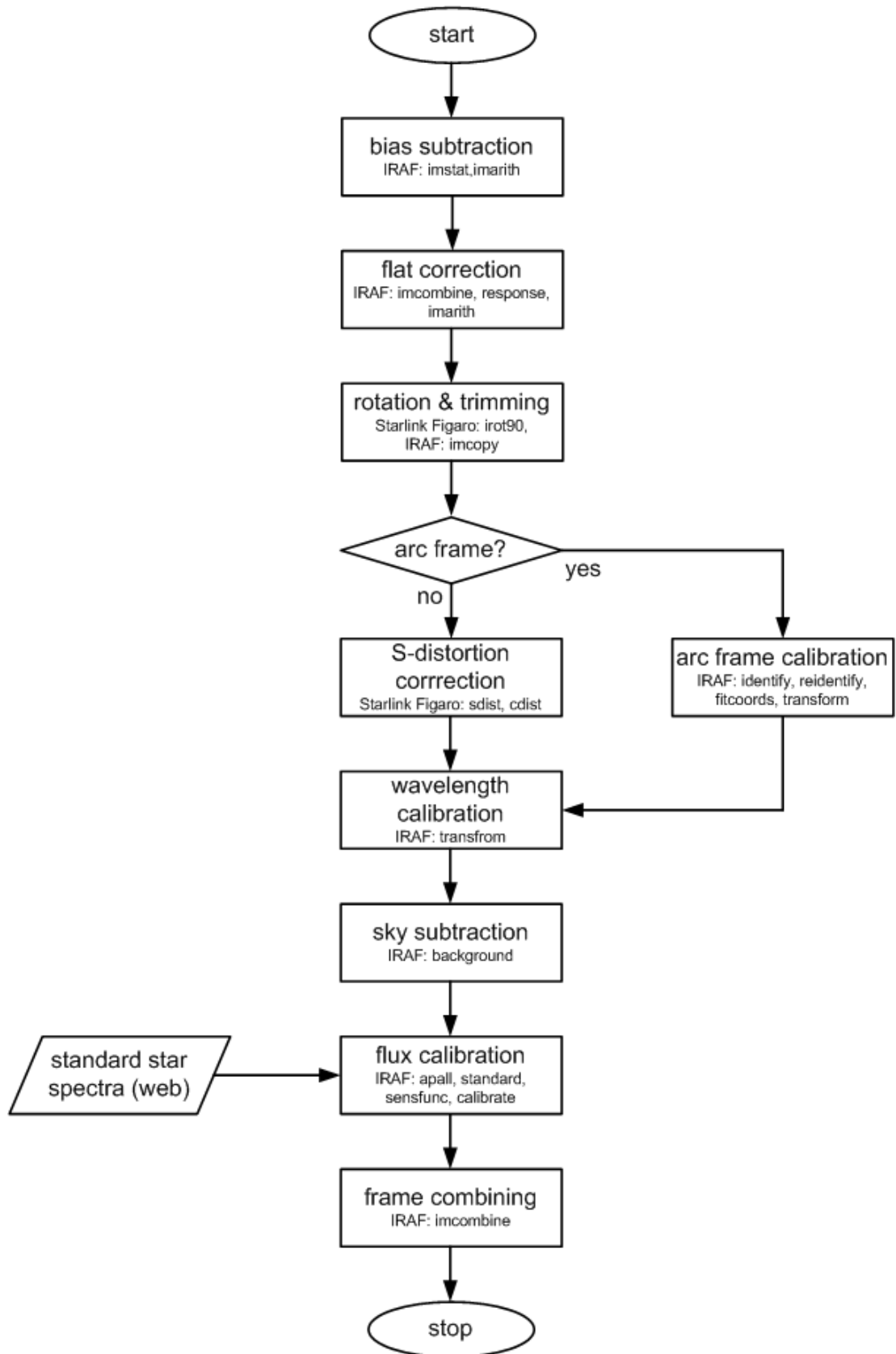
Figure 3-1: Flow chart of 2D data reduction process. Refer to appropriate sub-sections for details.

3.1.1 Bias Subtraction

CCD chip and electronics for signal processing produce a bias signal always present in frames even in the case of no exposure. This additive signal can be eliminated by subtraction of a master bias frame made by median combining of a number of bias frames taken with closed shutter and (almost) zero exposure time.

All INT observations have two bias frame blocks (6 to 11 bias frames each) taken in the evening and the morning of each observation night, respectively. The bias masters from evening and morning have been compared for their statistical properties. A significant difference in the mean values has been found, likely caused by temperature changes over the course of the night especially of the electronics (CCD detector is cooled and temperature stabilised). No significant difference of standard deviation of the masters has been found indicating no significant pixel-to-pixel variation of CCD bias levels.

As a consequence of checking the bias masters it was decided not to make use of the bias masters to avoid uncertainties regarding the correct bias level. Instead the individual bias section (pixel range [1:366,4105:4190] of the CCD not illuminated during observation) of each frame has been used for bias subtraction.

3.1.2 Flat Correction

Caused by intrinsic detector properties and/or optical path, the sensitivity of pixels is not equal across the CCD area. Flat frames, obtained by uniform illumination of the slit by a dome tungsten white lamp, are taken with same optical setup as target observations to correct this variation of pixel sensitivity.

In the case of spectroscopy the flat correction has two steps: a) polynomial or spline fitting of the flat spectrum along dispersion and spatial axis (axis definitions see Figure 3-2) and b) dividing scientific frames by the created master flat frame.

All INT observations have two flat frame blocks (6-11 frames each) taken in the evening and the morning of each observation night. The frames of each block are combined and fitted in both directions by cubic splines with the IRAF task called RESPONSE (see Figure 3-3). Dividing combined flat frames by the spline fits provides a normalised flat frame with pixel values close to unity used for flat correction of scientific frames by division.
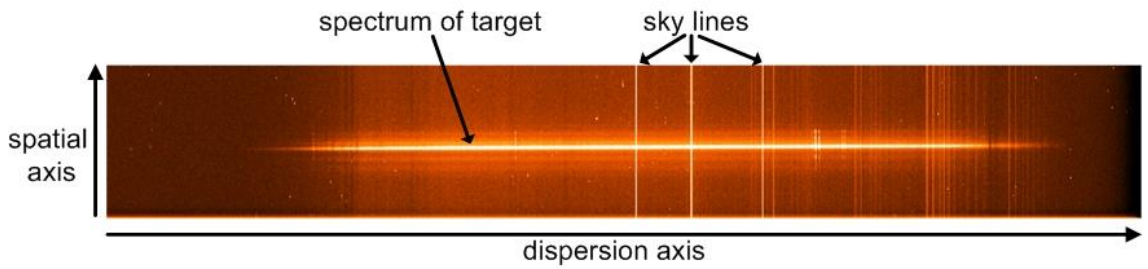
Figure 3-2: Definition of long-slit spectrum axes: dispersion axis (INT IDS: y-axis) runs along spectrum. The spatial axis runs (INT IDS: x-axis) along slit (image: INT frame r1446340 obtained on 2019-Feb-28; rotated by +90°).
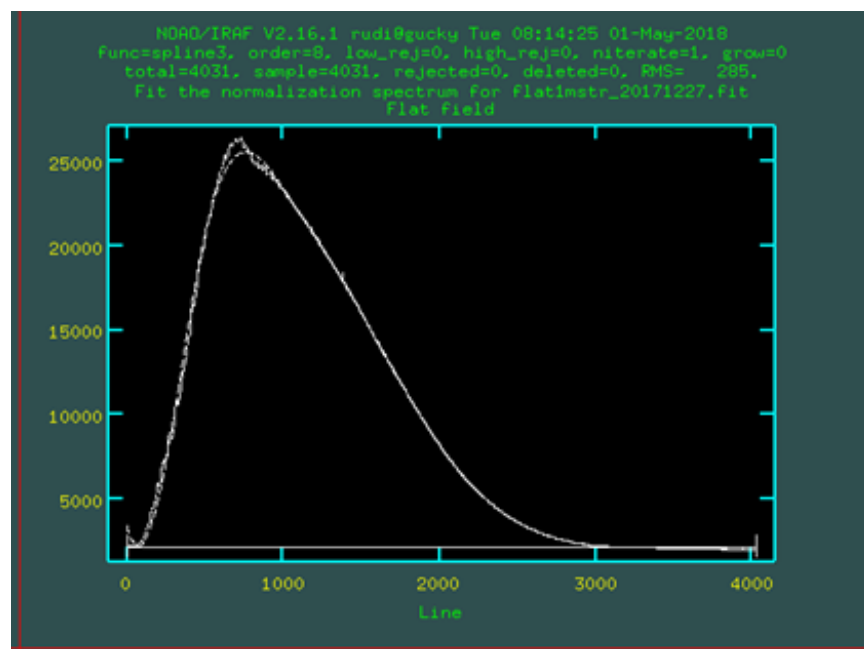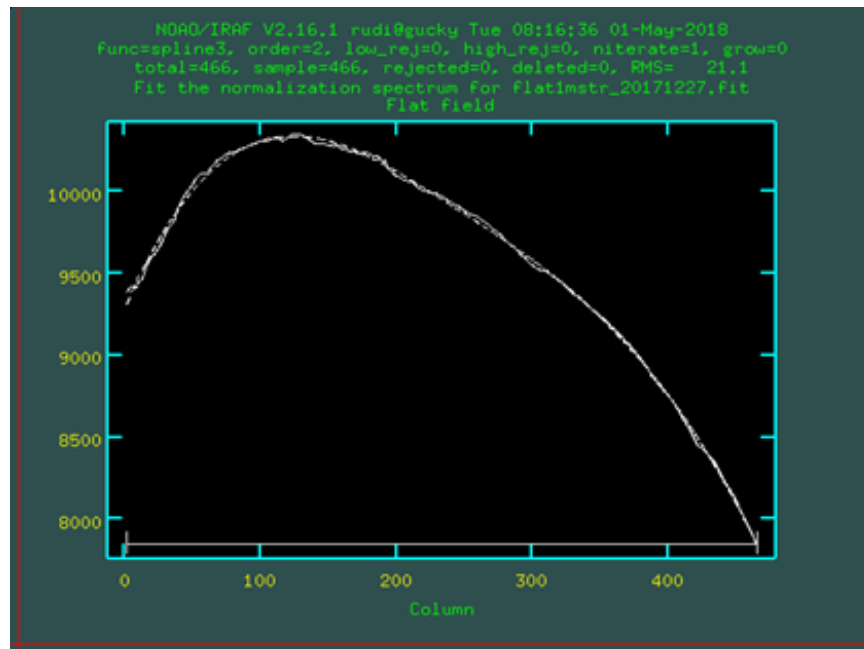
Figure 3-3: Spline fitting of flat frames in spatial (top) and dispersion direction (bottom) by IRAF RESPONSE task. Solid lines are averaged spatial and spectral graphs of flat frame, dashed lines are the cubic spline fits to the data.
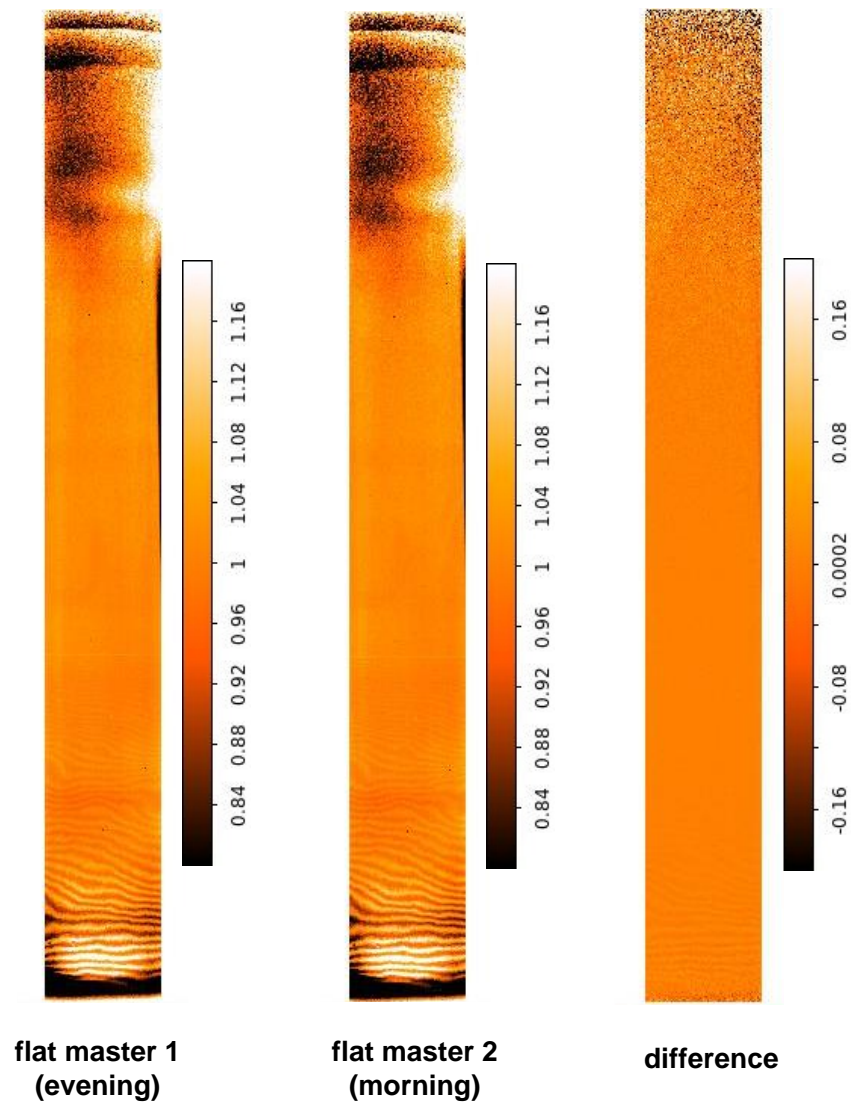
Figure 3-4: Check of evening/morning variation of normalised master flat frames. Masters of evening (left) and morning (middle) have values around unity and exhibit fringing at lower (long wavelength) area. The residual of both (right) is mainly below 1e-3 (except some noise in the shorter wavelength region) and has almost no fringing.

The two normalised flat frames of each night have been compared for changes during the night. Statistical evaluation (mean value, standard deviation) as well as visual inspection (Figure 3-4) has found no significant difference between both normalised masters. Consequently, flat correction has been done with the same master (evening master) for all observations of a night.

INT flat frames of some nights (all nights 2016; nights 2019-Feb-21 to 2019-Feb-24) are affected by dips in spatial direction (Figure 3-5) probably caused by some dirt in the flat illumination path. They have been eliminated by masking and removing with IRAF task FIXPIX.
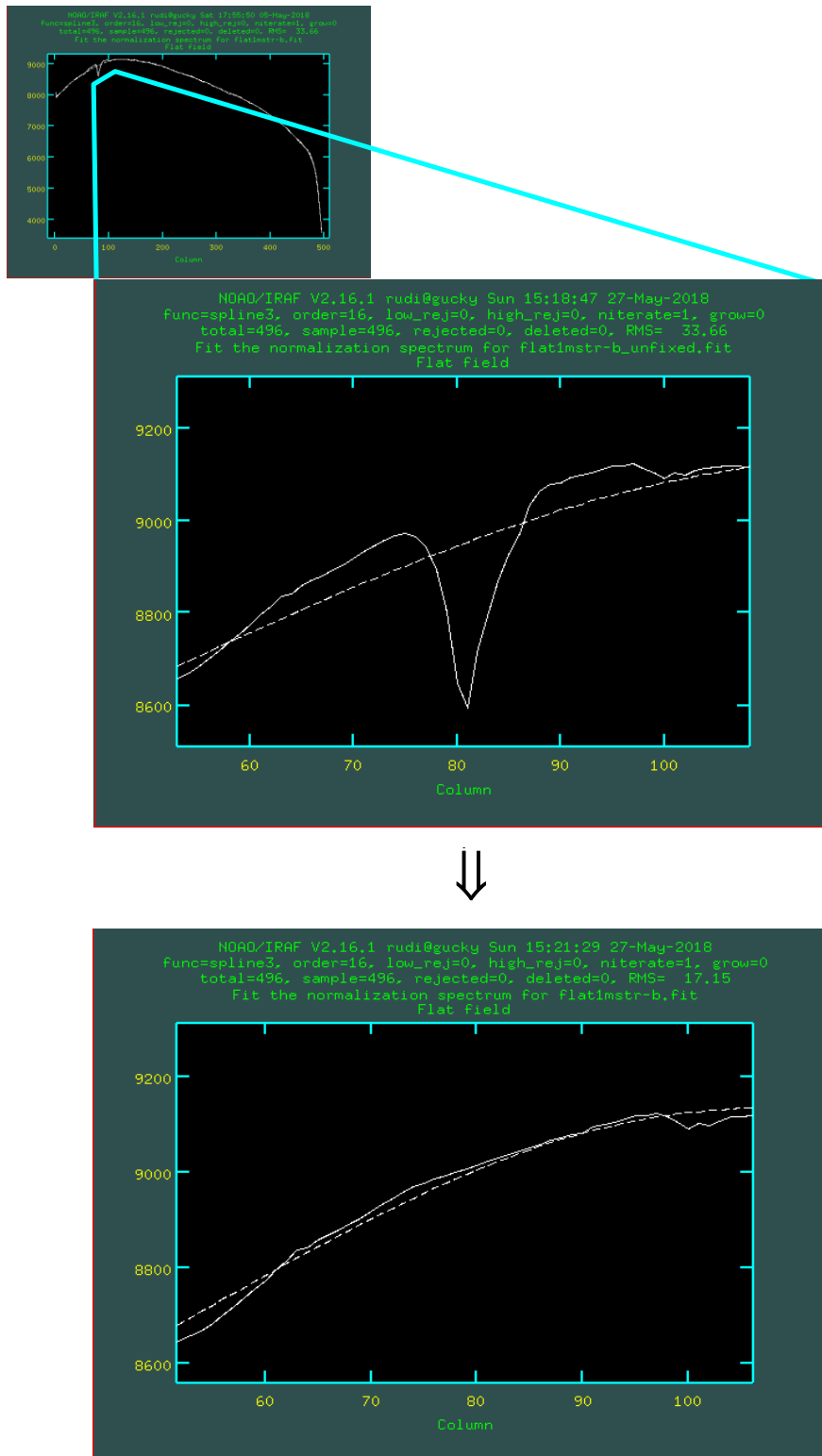
Figure 3-5: Dips in spatial direction (top) in flat frames of some nights must be removed to avoid artificial emphasising of spectral flux in affected regions. IRAF task FIX-PIX replaces dips by unaffected pixel values close to dip (bottom).

3.1.3 Rotation and Trimming

The bias and flat corrected frames are rotated by 90° to have the spectrum parallel to the x-axis (required for e.g. task 'SDIST', section 3.1.4) with short wavelengths to the left.
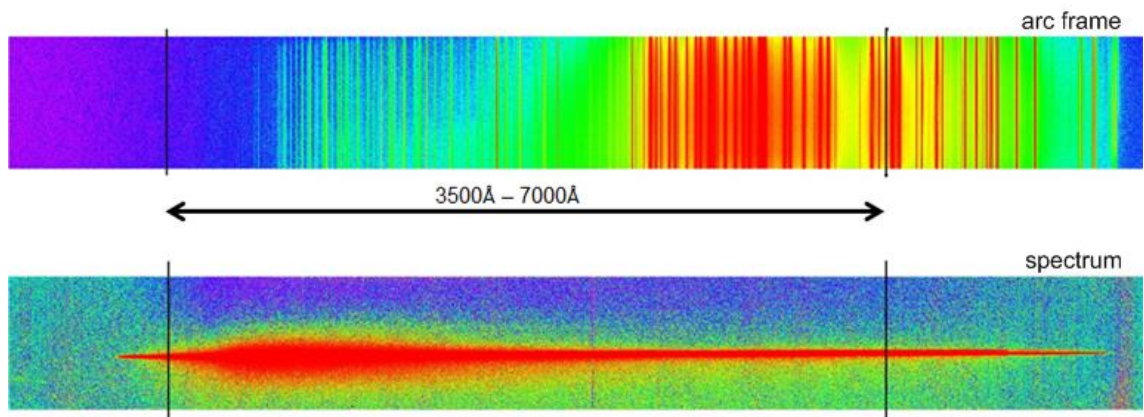
Figure 3-6: Trimming has been chosen to scientifically interesting wavelength range in order to avoid fitting problems of subsequent S-distortion correction.

The frames are trimmed to the scientific relevant range to get rid of the bias section and bad lines/columns at CCD edges. According to the spectral transfer function of the IDS instrument and the wavelength of emission lines used in the project, the wavelength axis has been trimmed to the relevant interval, 3500-7000Å (Figure 3-6).

3.1.4 S-Distortion Correction

Usually, the spectra are not aligned in parallel to the CCD axis and additionally can be curved (Figure 3-7) due to e.g. atmospheric refraction. For a correct 1D-extraction of the target spectrum this S-distortion must be eliminated.
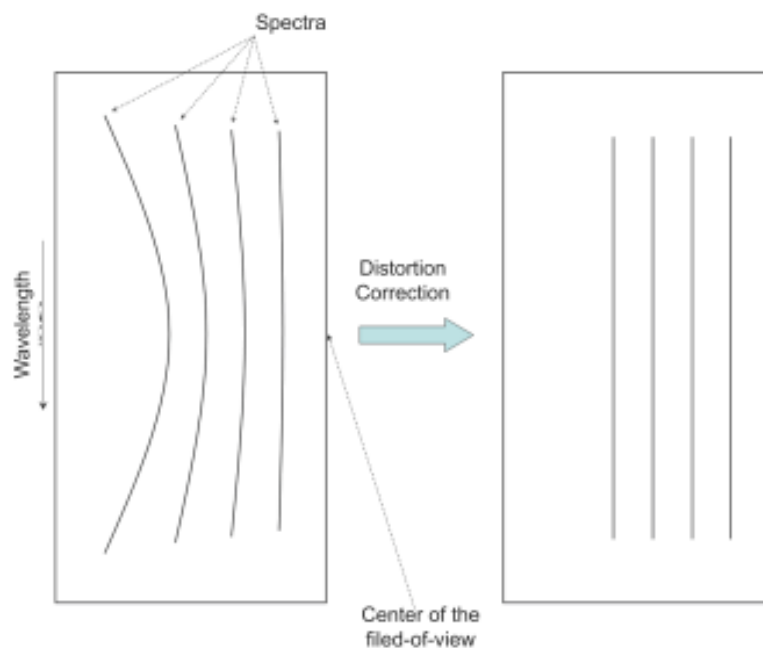
Figure 3-7: Schematic presentation of the S-distortion data reduction step. The spectra are usually curved and not aligned to the CCD wave-length axis. The S-distortion correction removes curvature and aligns the spectra parallel to CCD axis (credit: R.S.Furuya, Subaro Telescope).

45

The Starlink Figaro commands SDIST and CDIST are used to perform the S-distortion correction. Starting at a user specified point of spectrum (usually close to the central wavelength of the trimmed frame), SDIST traces the spectrum along the dispersion axis and provides polynomial coefficients for CDIST to correct all 2D spectra.

The procedure works well for bright spectra but can cause significant distortions (Figure 3-8) if SDIST is not able to trace the spectrum along the (trimmed) CCD wavelength range (usually due to bad SNR). For these few cases the degree of the polynomial fit had to be reduced to 1 to avoid numerical corruption of the spectral data. For good SNR spectra polynomial degrees 3 or 4 worked very well.
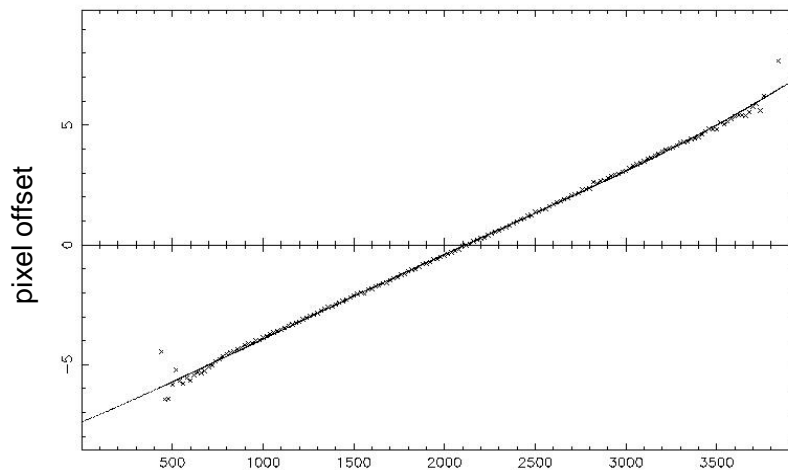
int1_o4_sn2009ga_r1233626-b1ft.jpg
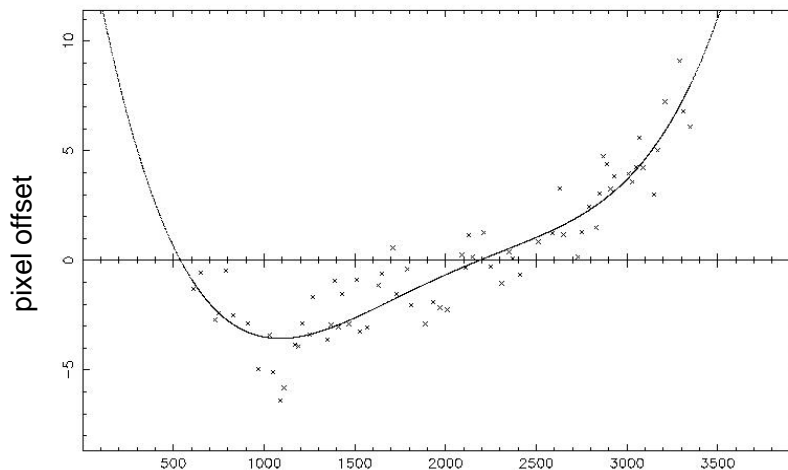
int1_o4_sn2002jz_r1233737-b1ft.jpg

Figure 3-8: Example for S-distortion correction at good SNR (top) and bad SNR (bottom) with a polynomial of degree 4. Crosses are spectral pixels traced by SDIST and solid lines are the polynomial fit. Axis numbers are column and (relative) row number of frame. Observations with good SNR are fitted very well almost independent of the degree of the fitting polynomial. However, S-distortion correction corrupts the spectrum of observations with bad SNR if polynomial degree is too high. It has been reduced to a degree of one for these cases.
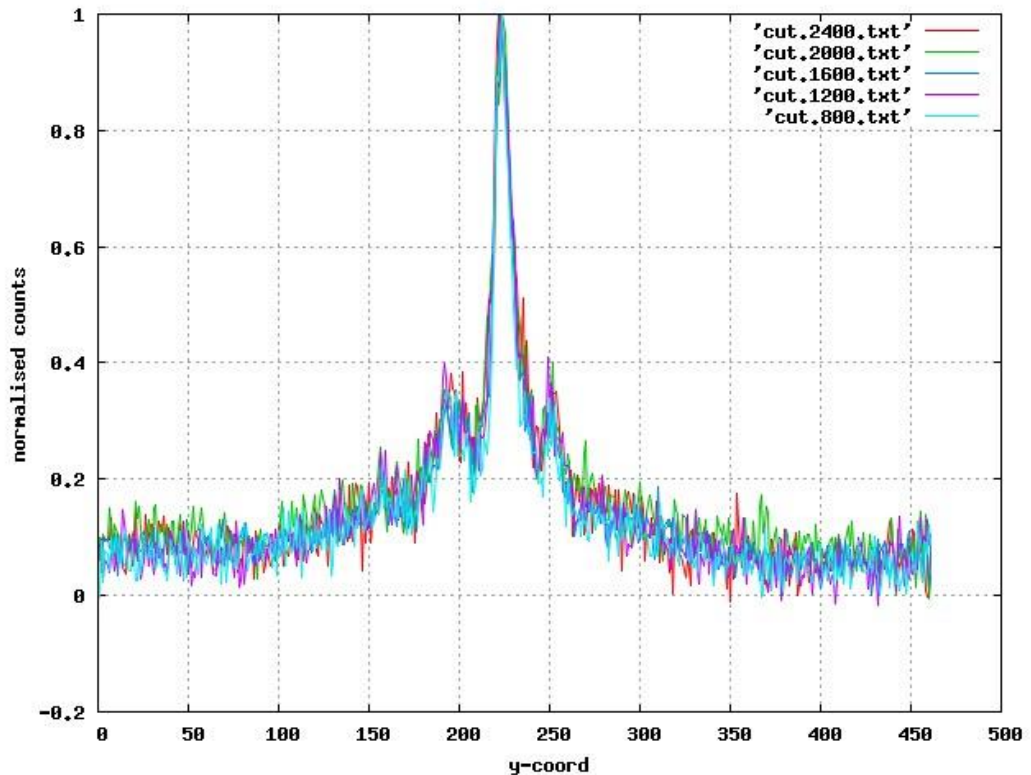
Figure 3-9: Check of S-distortion results by overlaying spatial cuts at different spectral positions. First cut (light blue) is at spectral axis pixel 800, last cut (brown) at pixel 2400. The position of peaks does not vary for different cuts proving that S-distortion worked well.

The results of the S-distortion correction have been checked by stacked plotting of several cuts along the spatial axis (Figure 3-9). The position of a spatial peak does not change even if the peak is located close to an endpoint of the spatial axis, far away from the initial point provided to SDIST to start tracing.

3.1.5 Wavelength Calibration

At least one (usually two) arc frames (for an example see the upper spectrum of Figure 3-6) have been taken for each observation to enable wavelength calibration. All arc frames are taken with the CuAr and CuNe arc lamps providing plenty of lines for calibration (ING Technical Note 133[16]).

The tasks used for wavelength calibration are IRAF tasks IDENTIFY, REIDENTI-FY, FITCOORDS and TRANSFORM. Firstly, IDENTIFY identifies some arc lines providing a 1-dimensional vector with the x-axis coordinates of lines identified. Task REIDENTIFY uses this reference vector to find identified lines at other spatial coordinates to provide enough sampling points for the task FITCOORDS that does a surface

---

[16] http://www.ing.iac.es/astronomy/observing/manuals/ps/tech_notes/tn133.pdf

fit to all of the 2D-spectrum. Finally TRANSFORM maps pixel coordinates of arc and scientific frames to wavelength values.

Check of wavelength calibration by the RMS values logged by REIDENTIFY showed RMS values less than 0.3 Å. A check of wavelength calibration by prominent sky lines (Figure 3-10) results in typical uncertainty better than 1 Å with worst case accuracy about 2 Å. Because DIPSO needs just an estimate of the emission line position for the line fitting (see section 3.2.4), the achieved wavelength accuracy is sufficient.
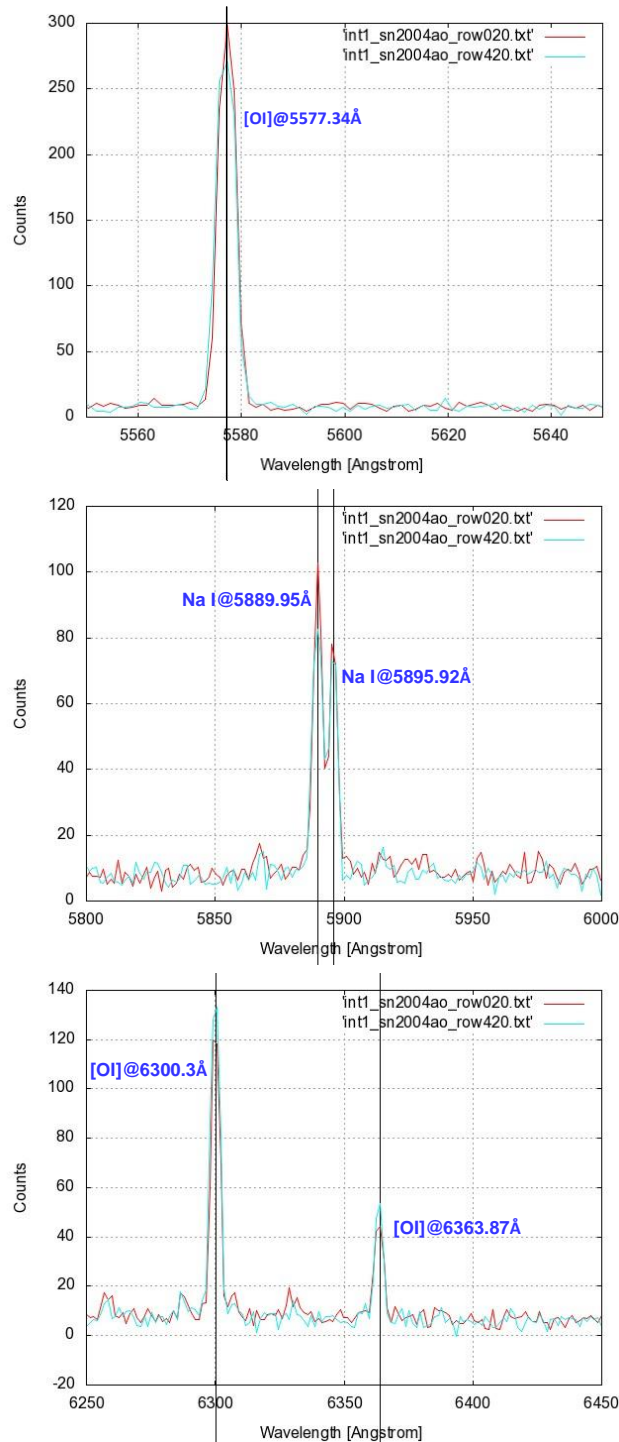
Figure 3-10: Example of wavelength calibration check by prominent sky lines. Plots show cuts along row 20 (red) and row 420 (blue); vertical black lines mark expected positions of the sky lines.

3.1.6 Sky Subtraction

Sky background subtraction removes diffuse scattered background light (moonlight, light pollution) as well as atmospheric emission lines. It has been done by the IRAF BACKGROUND task. The task relies on user defined background area(s) of the spectrum to evaluate background level and sky emission lines. The selected background areas should be free of astronomical signals and the BACKGROUND task works well if such area(s) are available (Figure 3-11).

r1355413 before sky subtraction

r1355413 after sky subtraction
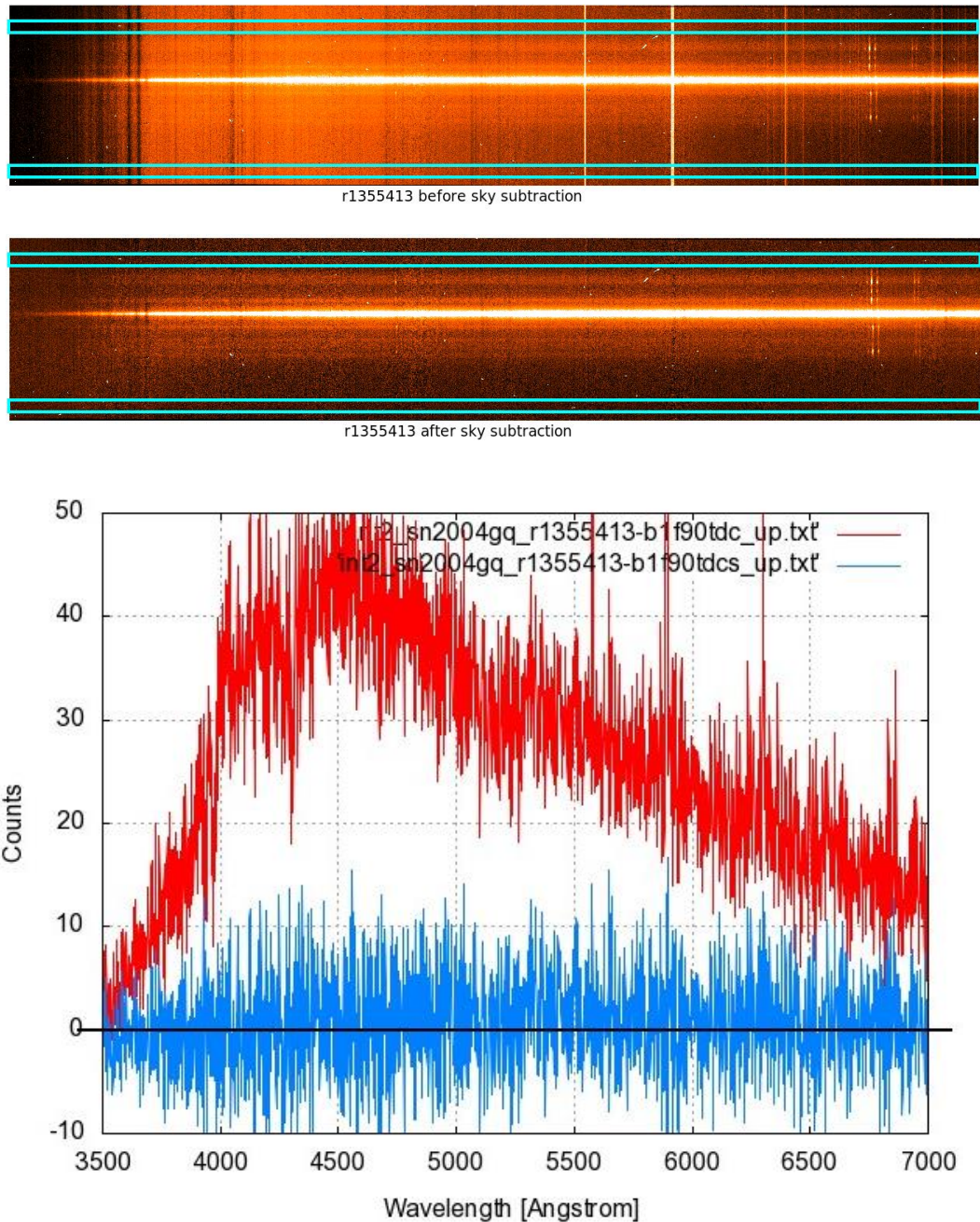
Figure 3-11: Example of sky subtraction: The two frames at top show the spectra before and after sky subtraction, respectively. The light blue boxes indicate the regions selected for IRAF to calculate background levels. The chart at bottom shows cuts along row 420. Before correction (red) the spectrum is contaminated by scattered moonlight and sky lines. The blue curve shows the sky background subtracted result.
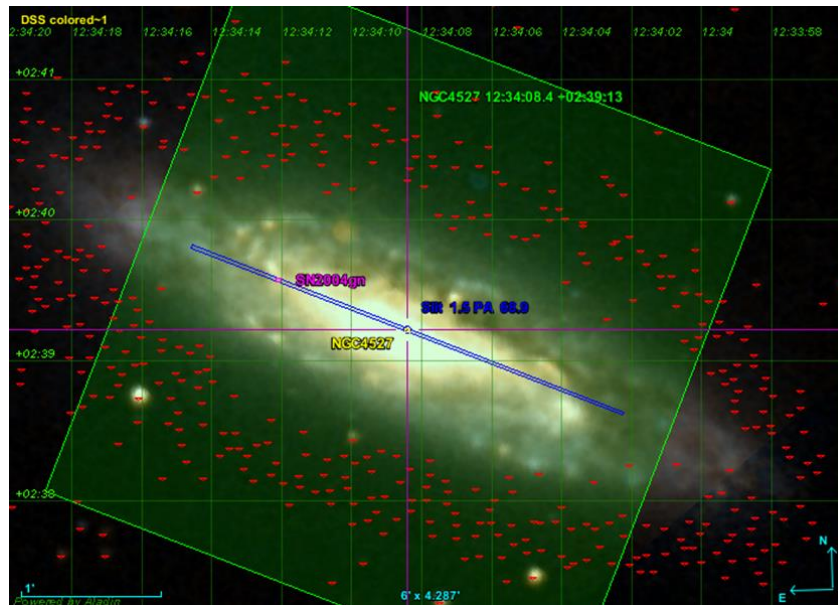
Figure 3-12: Finding chart of SN2004gn. The slit is completely covered by host galaxy NGC4527 and consequently Hα line is present over all the spatial axis causing problems with sky subtraction.

There are some targets where the slit is covered by the host galaxy totally (e.g. SN2004gn, Figure 3-12) and (at least) the Hα line is present all over the spatial axis. Consequently, IRAF BACKGROUND task treats Hα as a sky line and tries to remove it. This results in a wrong evaluation of the Hα/[NII] ratio and creates (in the case of host rotation) artificial absorption lines on one side of host centre (Figure 3-13). It is not possible to mask the Hα region in the BACKGROUND command so sky background subtraction has been omitted for these problematic cases.
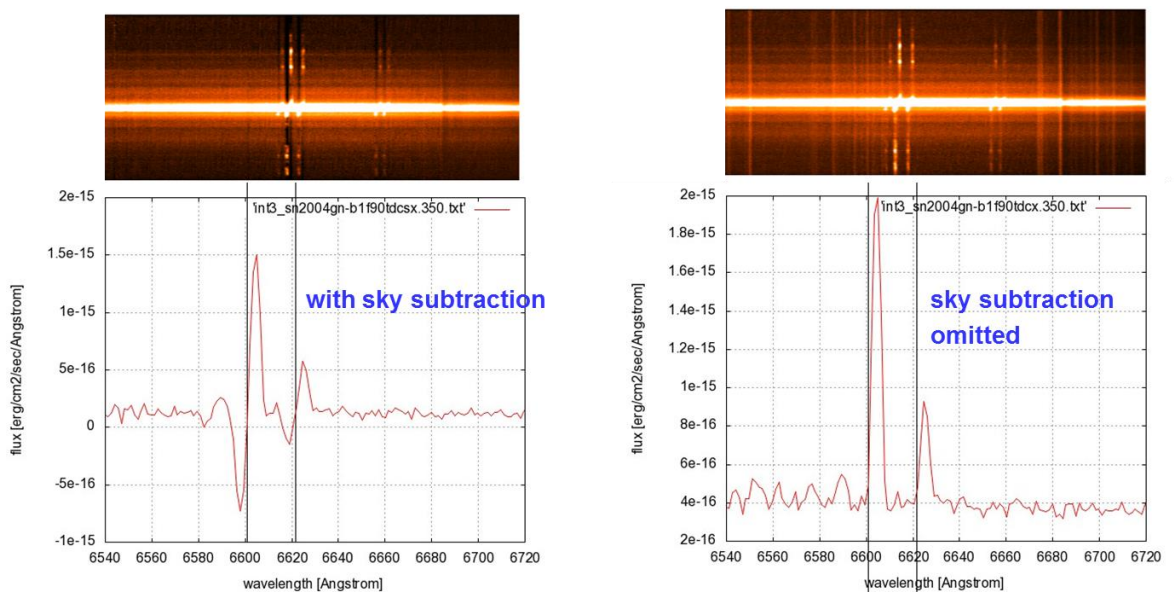
Figure 3-13: Artificial absorption lines (left) as outcome of IRAF sky subtraction if Hα line (and others) is present along all slit and the host galaxy is rotating. Plots show a cut along row 350 in the Hα wavelength region; vertical black lines mark the redshifted position of the Hα and [NII] lines without host rotation. Omitting sky subtraction fixes the issue (right), at the expense of a higher background level.

50

3.1.7 Flux Calibration

Flux calibration is done with a sensitivity function calculated by means of observations of spectrophotometric standard stars (Figure 3-14). At least two observations of standard stars have been done each night. Additionally, flux calibration needs as input the known fluxes of the used standard stars, which have been downloaded from the INT web page (see Table 2-4).
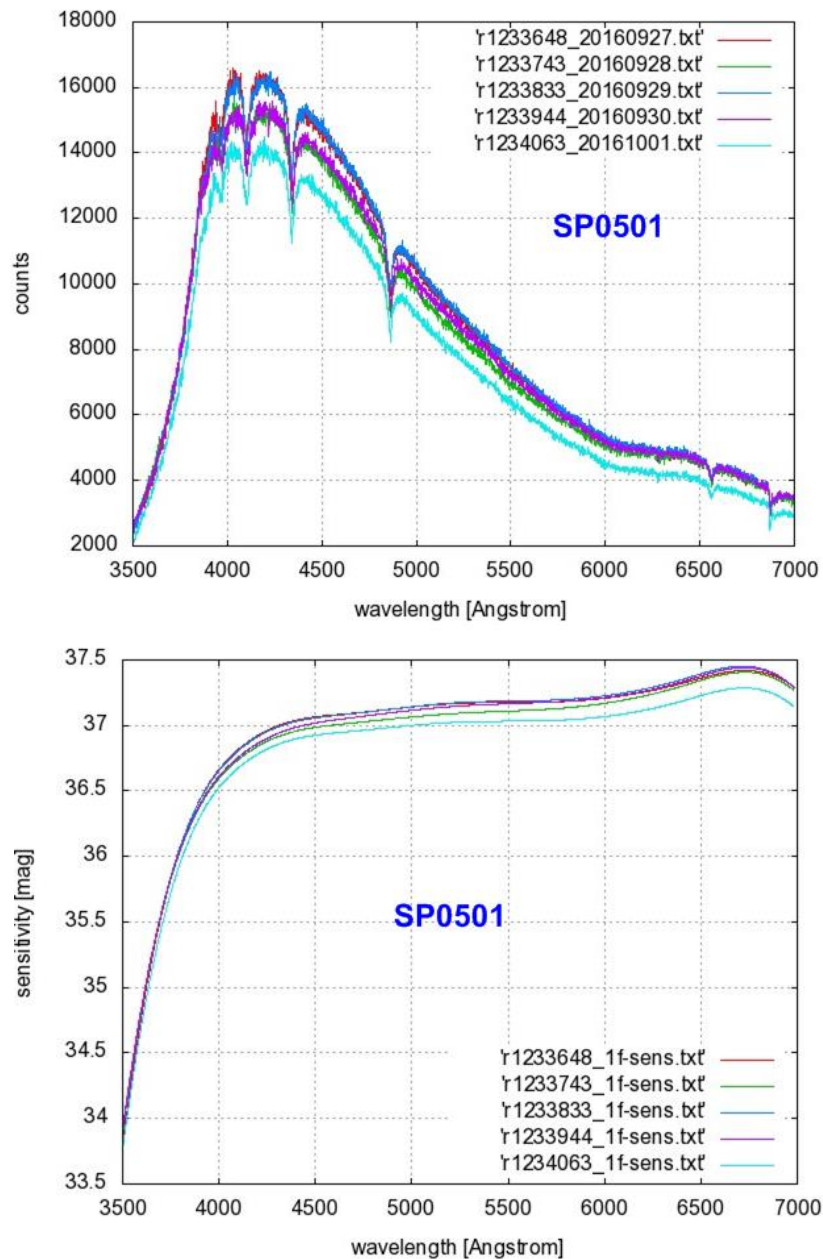
Figure 3-14: Example of standard star observations as basis for flux calibration. The chart on top shows the observed fluxes of standard star SP0501+527 for the five nights in Sep 2016. The variation of fluxes results in variation of the sensitivity function (bottom) for the nights, calculated by IRAF STANDARD & SENSFUNC commands. The flux calibration of observations of a particular night uses the corresponding sensitivity function.

Different flux tables for standard stars are available and it is not obvious which one is the best one. AB magnitude tables with highest cadence have been selected for the flux data calibration.

The IRAF tasks STANDARD, SENSFUNC and CALIBRATE have been used for the flux calibration. STANDARD fits the obtained standard star observations to the bandwidth at which the recorded flux of a standard star was obtained. SENSFUNC calculates with these results (more than one standard star observations is possible) and additional extinction data of the observatory site (La Palma extinctions[17]) the sensitivity function by cubic spline fitting of the ratios of the observed count rate per Å to the expected flux expressed in magnitudes (details see SENSFUNC manual[18]). Finally, CALIBRATE uses the sensitivity function to calculate the flux calibrated spectrum (Figure 3-15). The uncertainty of the flux calibration has been estimated to less than 10% from the scatter of the sensitivity functions (Figure 3-14), good enough for the scientific goals (only ratios of close emission lines are important).
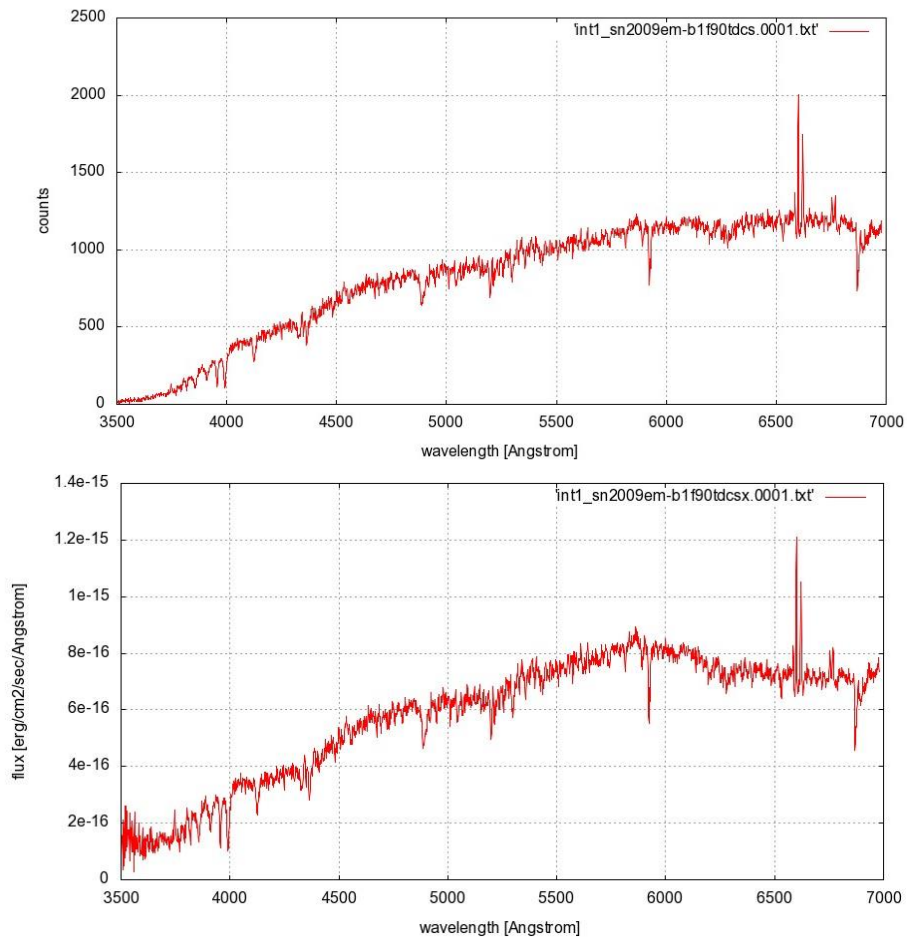
Figure 3-15: Example of spectrum before (top) and after (bottom) flux calibration done by IRAF command CALIBRATE and the sensitivity function (Figure 3-14) of the night of observation.

[17] http://www.ing.iac.es/astronomy/observing/conditions/wlext.html
[18] https://iraf.net/irafhelp.php?val=sensfunc&help=Help+Page

3.1.8 Frame Combining

Three exposures are available for each target. As a last step of 2D data reduction the cleaned and calibrated target frames have been combined by the IRAF IMCOMBINE command using median combining.

3.2 Data Reduction Flow 1D

Based on cleaned and calibrated 2D spectra obtained from the 2D data reduction, the spectra of SN sites must be extracted, extinction corrected and the flux of the emission lines estimated by emission line fitting (Figure 3-16).

These steps of data reduction essentially make use of the same tools as 2D data reduction: IRAF and Starlink. Additional tools have been used for emission line fitting (see 3.2.4).
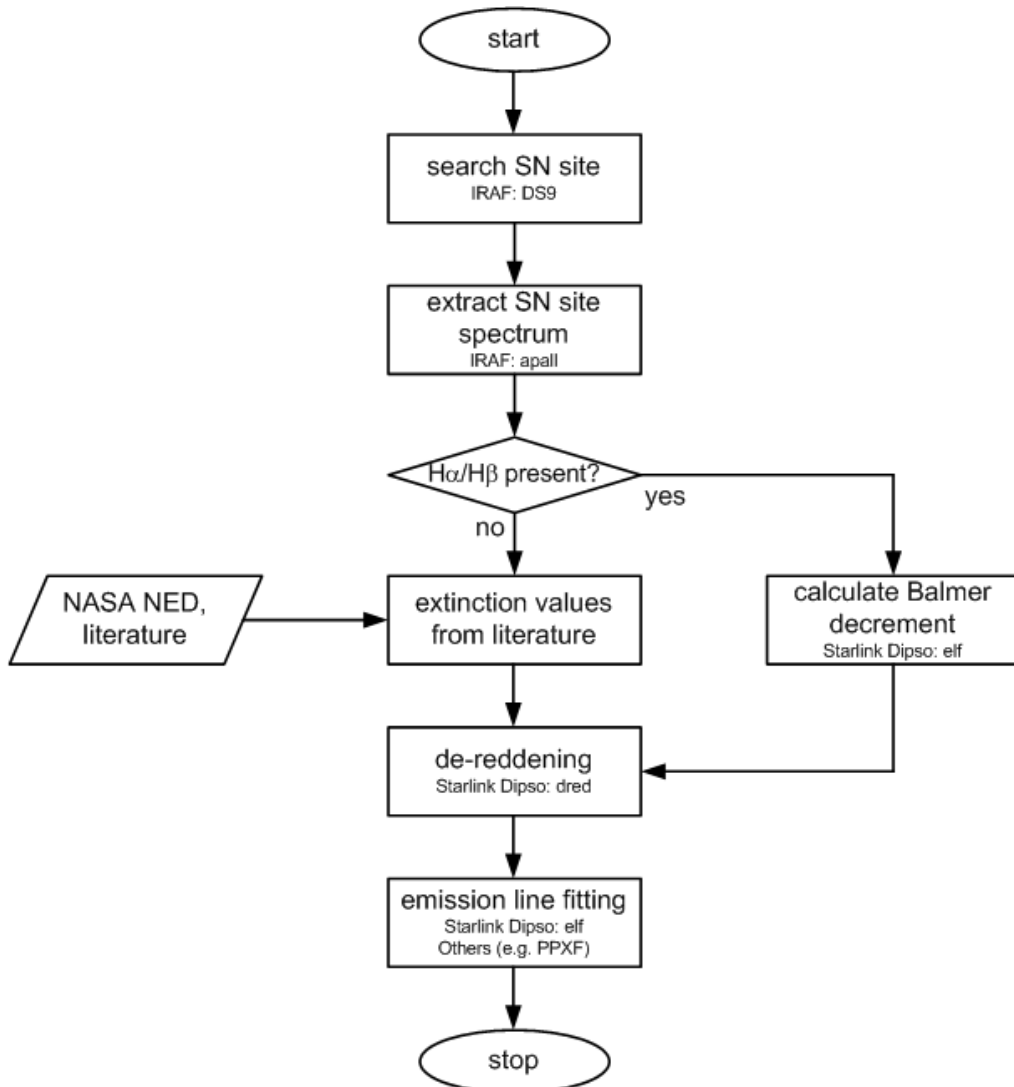
Figure 3-16: Flow chart of 1D data reduction process. Refer to appropriate sub-sections for details.

3.2.1 Finding SN Site

The search for SN sites in 2D-spectra have been complicated for INT observations in Sep 2016 and Dec 2017 because the RA and Dec coordinates recorded in the frame header did not match the host galaxy coordinates. The difference of host galaxies' coordinates and the observations' coordinates documented in the FITS headers is significantly larger than INT pointing accuracy of 5" (Laing and Jones 1985). With recorded header coordinates, the slit would have been partially placed outside host galaxy in obvious contradiction to obtained 2d spectra (Figure 3-17).
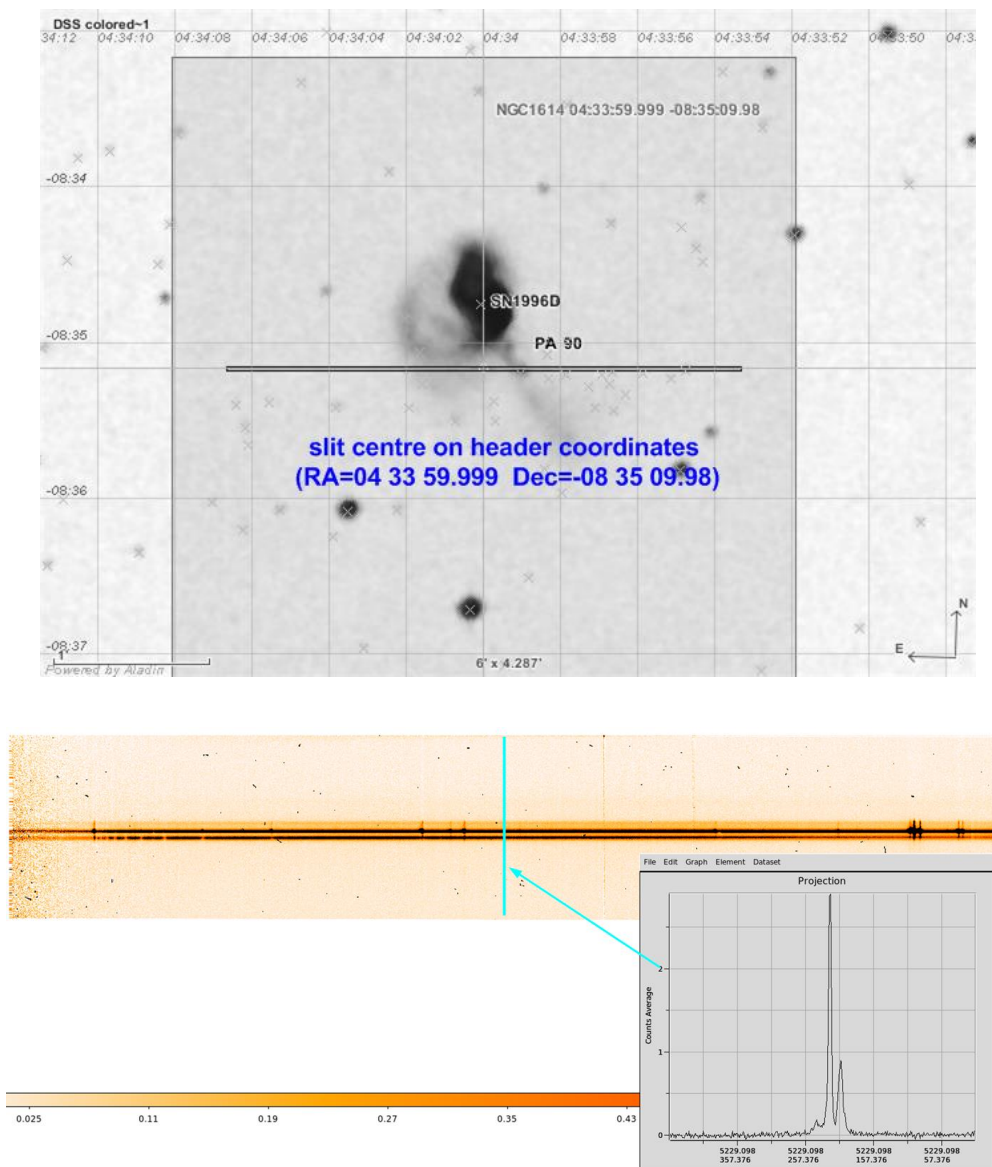
Figure 3-17: Example of wrongly recorded INT pointing coordinates. The chart on top is an image of NGC1614 with target SN1996D almost at the galaxy centre. If the slit is placed according to RA-Dec as recorded in the FITS header of the observation the host galaxy would be missed completely. This is in obvious contradiction to the spectrum (bottom). The cut along the spatial axis clearly shows peaks of the centre and a spiral arm of host NGC1614 as confirmed by contour plot (Figure 3-18).
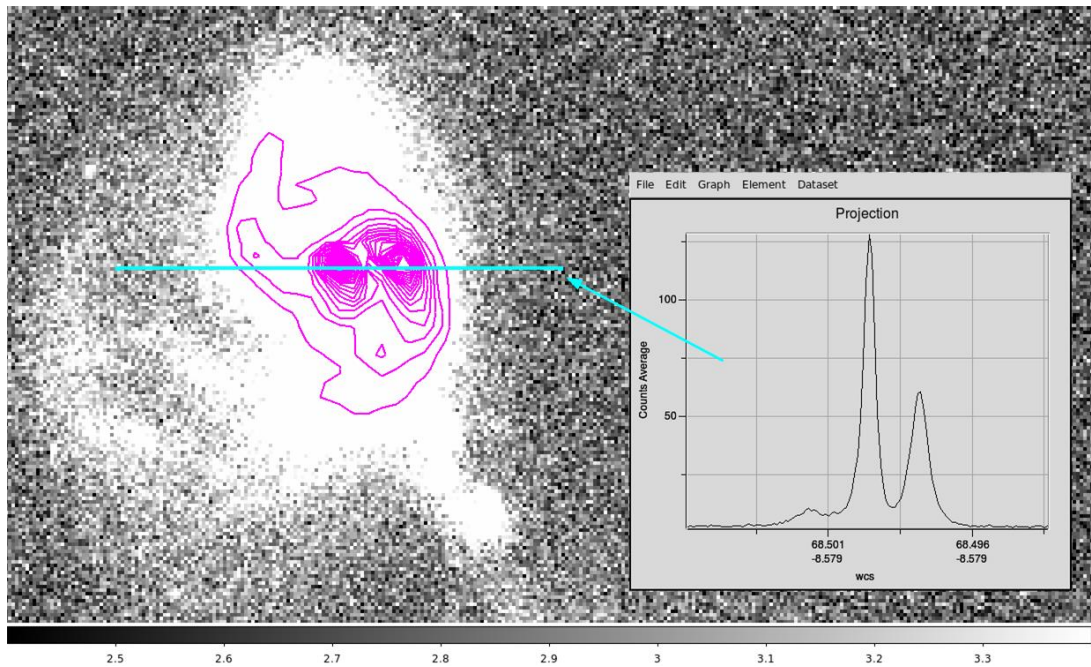
Figure 3-18: Confirmation of spatial profile of Figure 3-17 by contour plot of host NGC1614. The cut along the blue line is consistent with the spatial profile of observed spectrum (photometric image of NGC1614: NGC1614 (NED)[19]).

There must be an error with recorded coordinates and the actual slit position has to be determined by other means. These additional means were acquisition images (e.g. Figure 3-19), contour plots (e.g. Figure 3-18) of photometric observations of host galaxy and - depending on suitable inclination - evaluation of the host galaxy rotation by the change of redshift at host centre.
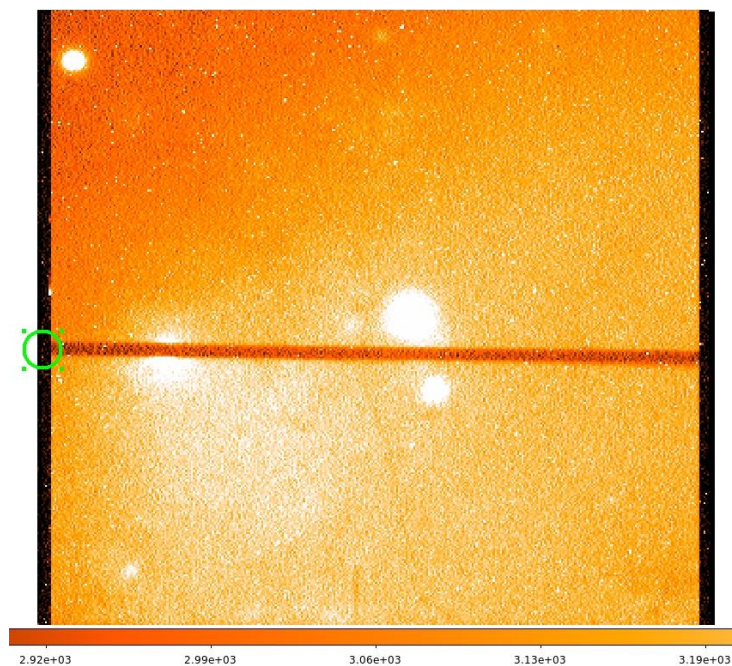
Figure 3-19: Example of INT IDS acquisition image (SN2007gr, frame r1446295 taken on 2019-02-27) with spatial origin on CCD at left (marked by green circle).

[19] http://ned.ipac.caltech.edu/uri/NED::Image/fits/2005ApJ...630..784T/NGC_1614:I:B:tjw2005

55
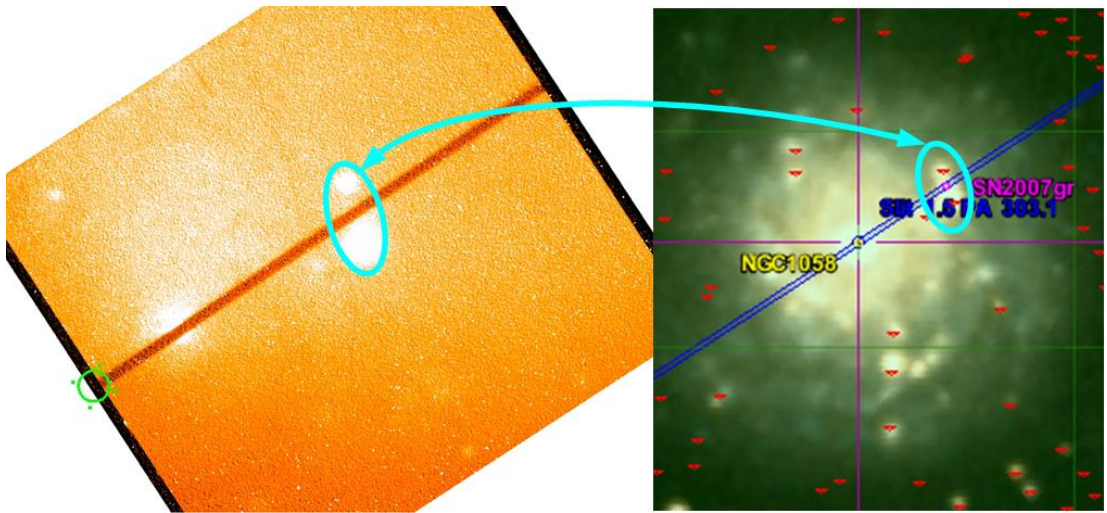
Figure 3-20: Example for slit orientation on sky (left) derived from acquisition image (see example Figure 3-19) by DS9 'Invert Y' command and rotation about recorded position angle plus 90°. Slit orientation matches required angle of the finding chart (right; the finding charts were made by the current author for targets, prior to observing runs, to facilitate the observations).

The target acquisition of INT director's time observations in 2018 and 2019 as well as our own observations in Feb 2019 used blind offset acquisition of host centre proven as very reliable. The recorded target coordinates fit host centre coordinates well within INT pointing accuracy. Additionally, the exposure time of acquisition images has been increased to obtain images with better quality to evaluate slit orientation by acquisition image.

The slit orientation in the INT IDS acquisition images is always horizontal and the spatial origin on CCD is always on left (Figure 3-19). The slit orientation on sky may differ from the position angle of the SN site by ±180°. In order to find the actual slit orientation on sky from INT acquisition image and recorded position angle, the following steps in IRAF image display tool DS9 are required:

- mark left endpoint (=spatial origin of spatial CCD axis) of slit in acquisition image,
- apply DS9 command 'Invert Y' to mirror acquisition image along x-axis,
- rotate inverted image by position angle of target frame header plus 90°.

The example in Figure 3-20 shows that the slit orientation in the processed acquisition image has the same orientation as in the finding chart. Because the spatial CCD origin in Figure 3-20 (green circle) is on the left, the SN site (magenta box in finding chart) in the spectrum is to the right of the host centre peak in this example.

With the steps above the position of the SN site relative to the host centre peak is known. The number of pixels from the host centre peak to SN site is given by the known angular distance divided by INT IDS scale factor 0.4"/px (see section 2.2).

56

3.2.2 Extraction of SN Site Spectrum

Extractions of 1D-spectra of SN sites have been done by the IRAF APALL task. It requires an aperture in the spatial direction over which it integrates the flux at each wavelength. This aperture must be chosen carefully. On one hand, the aperture must be as small as possible to integrate just over the SN site HII region to avoid contamination by other (stellar) sources. On the other hand, the aperture must be large enough to collect all light from HII region taking into account seeing and instrumental imperfections.

An aperture of 1" corresponds to a linear size of about 4.85pc/Mpc giving about 15 pc for the closest host galaxy in sample, exceeding the size of a typical HII region (Table 1-1). But 1" aperture is too small because of seeing (about 0.8"-1.2"; INT seeing[20]), INT guiding accuracy (~0.3", Laing and Jones 1985) and other imperfections of optical path. By checking different sizes, an aperture of 4" has been proven as a reasonable choice. For a host galaxy at 30 Mpc, the 4" corresponds to a size of about 0.6 kpc (see sections 3.2.4 and 5.2.5 for discussion of potential stellar contamination).

3.2.3 Extinction Correction

Flux from a target is absorbed and scattered by the interstellar medium of Milky Way and host galaxy resulting in a line of sight and wavelength dependent extinction. This reddening can be removed by the so-called Balmer decrement if the Hα and Hβ lines are present in the spectrum. Balmer decrement relies on a known intrinsic intensity ratio Hα/Hβ and empirical interstellar extinction curves (Osterbrock & Ferland 2006, Chapter 7). The method is based on the physical extinction relation

$$\frac{I(H\alpha)}{I(H\beta)} = \frac{F(H\alpha)}{F(H\beta)} \, 10^{C(f(H\alpha)-f(H\beta))} \qquad \text{(Eq. 3-1)}$$

where: I(Hα,Hβ) = intrinsic line intensity, F(Hα,Hβ) = observed flux and
f(Hα) = 0.818; f(Hβ) = 1.164 (Osterbrock & Ferland 2006, Table 7.1 with R=3.1)

From quantum physics, for case B recombination (i.e. the nebula is assumed to be optically thick to Lyman photons), the ratio I(Hα)/I(Hβ) is given to be 2.86. By rearranging of (Eq. 3-1) and the data above, the constant C is given. The colour excess E(B-V), as common measure of extinction, is given from C by multiplication with 0.77 (Conti et al. 2012, p.183).

[20] http://www.ing.iac.es/astronomy/observing/conditions/#seeing

With known E(B-V), the extinction correction is performed with Starlink DIPSO command DRED. Targets with a spectrum lacking Hβ emission cannot be extinction corrected by Balmer decrement. Because such targets usually lack other suitable emission lines for extinction correction as well, it is only possible to take into account Galactic reddening by using literature values (e.g. from NED) for Galactic extinction in the direction to target host galaxy. Thus, the extinction of the host galaxy is ignored due to necessity. Because the emission lines of the N2 and O3N2 methods (see section 1.4.3) are close to each other, the resulting error of estimated metallicity is negligibly small.

3.2.4 Emission Line Fitting

Measurement of the SN site metallicity by emission lines requires the calculation of line flux by emission line fitting e.g. with the Starlink DIPSO command ELF. ELF requires an estimate of line peak wavelength and of full width at half maximum (FWHM) as inputs and it fits the lines found by Gaussian fits (default; other fits are possible). It works reliably for lines with good SNR but provides some numerically dubious results for targets with bad SNR (see section 3.2.5).

Targets having a spectrum contaminated by stellar radiation (e.g. Figure 3-21) cause problems also because ELF is not able to disentangle emission lines and stellar absorption at the same wavelength.
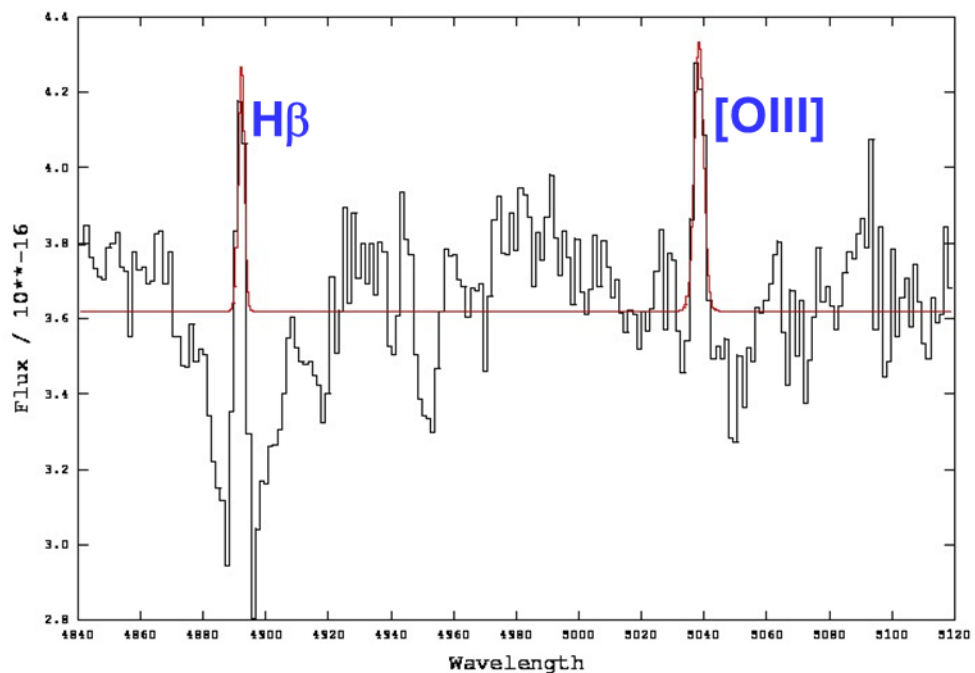
Figure 3-21: Worst case example of a spectrum at Hβ line strongly affected by stellar contamination (target SN2004fc). The black line is the original spectrum and the red line is the ELF result of Hß and [OIII] emission line fit. The calculated line flux of Hβ is obviously wrong as is the inferred metallicity by O3N2 method.
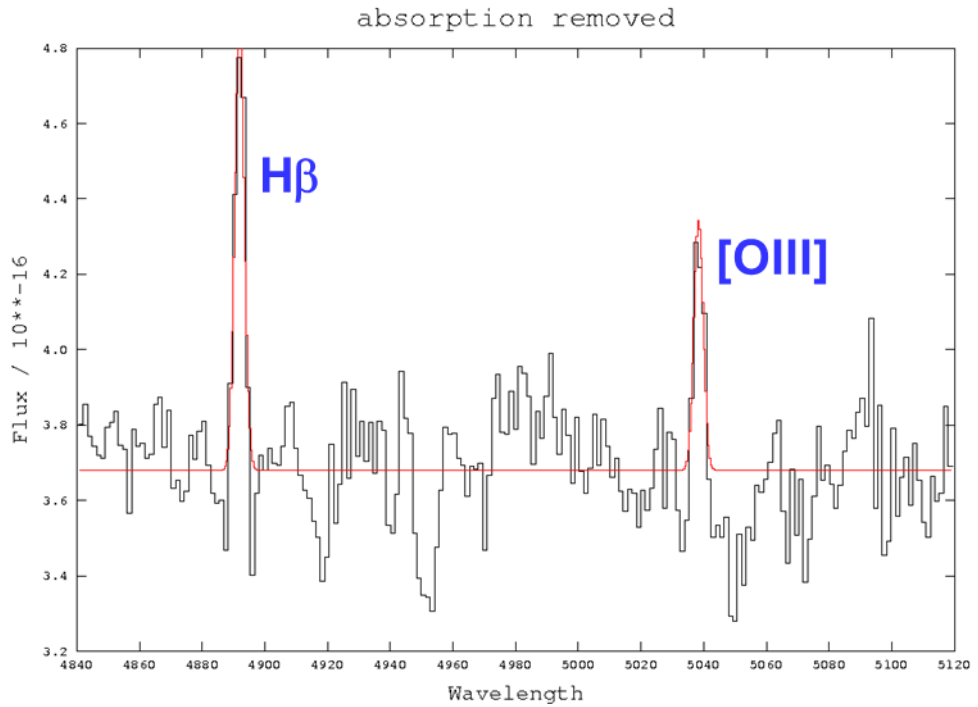
Figure 3-22: Absorption at Hβ line of Figure 3-21 removed by workaround as described in the text. The black line is the corrected spectrum of SN2004fc and the red line is the new ELF result of Hß and [OIII] emission line fit.

For all cases where the stellar absorption is broader than the emission line, the absorption is removable with ELF by a workaround: a) cut the emission line affected by contamination from spectrum; b) fit remaining absorption line by ELF and subtract the Gaussian absorption fit from initial spectrum. The workaround has been applied to 12 targets and worked well (e.g. Figure 3-22).

The DIPSO ELF workaround fails for contaminated targets with narrow underlying absorption lines that are masked by the corresponding emission line. The Penalized PiXel Fitting (PPXF) method (Cappellari 2017) has been used to check all spectra for hidden stellar contamination. PPXF fits the stellar component of a spectrum with a maximum penalised likelihood approach based on a set of synthetic spectra with varying stellar parameters (e.g. age, metallicity). It is able to fit emission lines as well (Figure 3-23). Two different spectral templates (taken from MILES library, Vazdekis et al. 2010) have been applied for the test of the PPXF fitting: The Padova code (Girardi et al. 2000) models with the unimodal[21] and with the Kroupa universal[22] initial mass function.

---

[21] ftp://milespublic:phoShi4v@ftp.iac.es/MILES; file MILES_PADOVA00_UN_baseFe.tar.gz'
[22] ftp://milespublic:phoShi4v@ftp.iac.es/MILES; file 'MILES_PADOVA00_KU_baseFe.tar.gz'
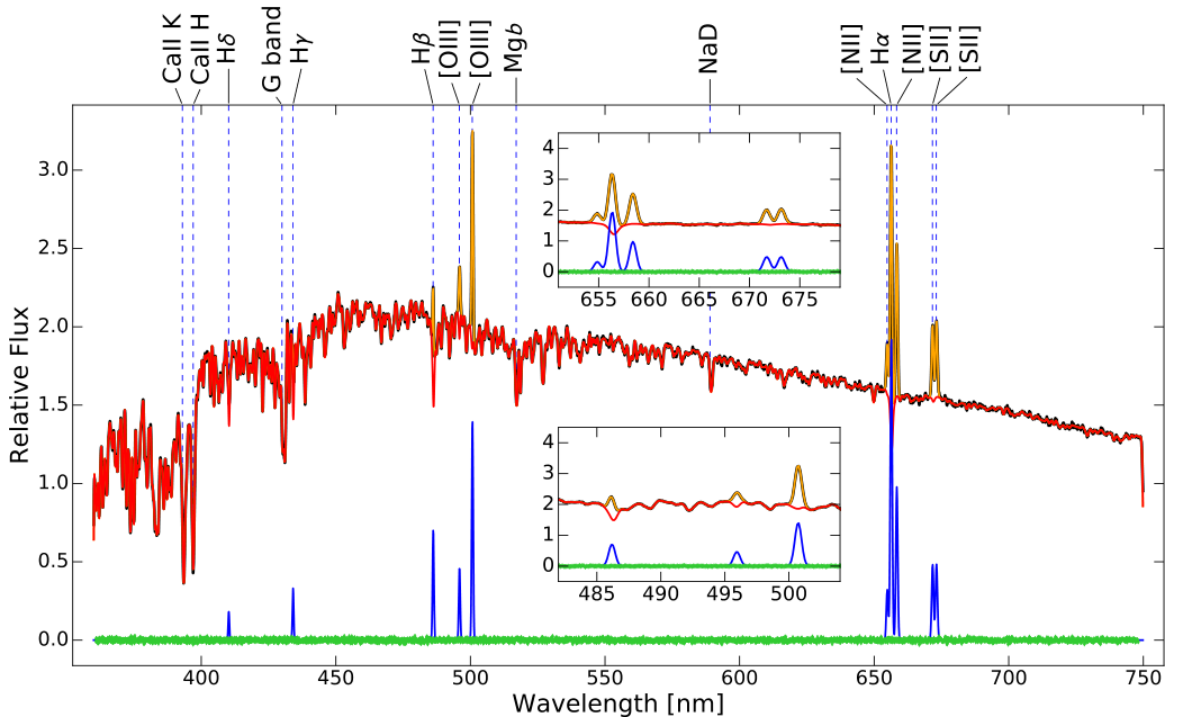
Figure 3-23: Example of a PPXF fit. The red line is the PPXF fit to the stellar component, The black line (hard to see because of the excellent fit) is the initial spectrum. The orange line is the fit to the emission lines. The green line shows the fit residuals and the blue line is the gas-only fit (Image: Cappellari 2017).

The line fluxes of fits by PPXF excellently match DIPSO results for Hα and [NII] (mean deviation <2%). But there are large differences (mean ~20%) in flux values of Hβ and of [OIII] whereas the ratios Hβ/[OIII] match DIPSO ratios so that the inferred metallicities by PPXF fits and DIPSO ELF fits match very well (some numerical issues excepted).

3.2.5 Examples of reduced SN Environment Spectra

This section presents some examples of the reduced spectra of SN sites to provide an impression of the quality range of the obtained spectra. For the quantitative evaluation of the spectra see chapter 4.

Figure 3-24 to Figure 3-26 are typical results of the spectra of the HII region of the SNe, one example for each SN type. The upper panel of the figures show the total spectral range with the most prominent emission lines, the middle panel is the zoomed Hα region with the [NII] doublet and the lower panel is the zoomed Hβ region with the [OIII] doublet. The example spectra of the three different SN types do not differ qualitatively as expected because the spectra are from the HII regions only and not from the SNe itself.
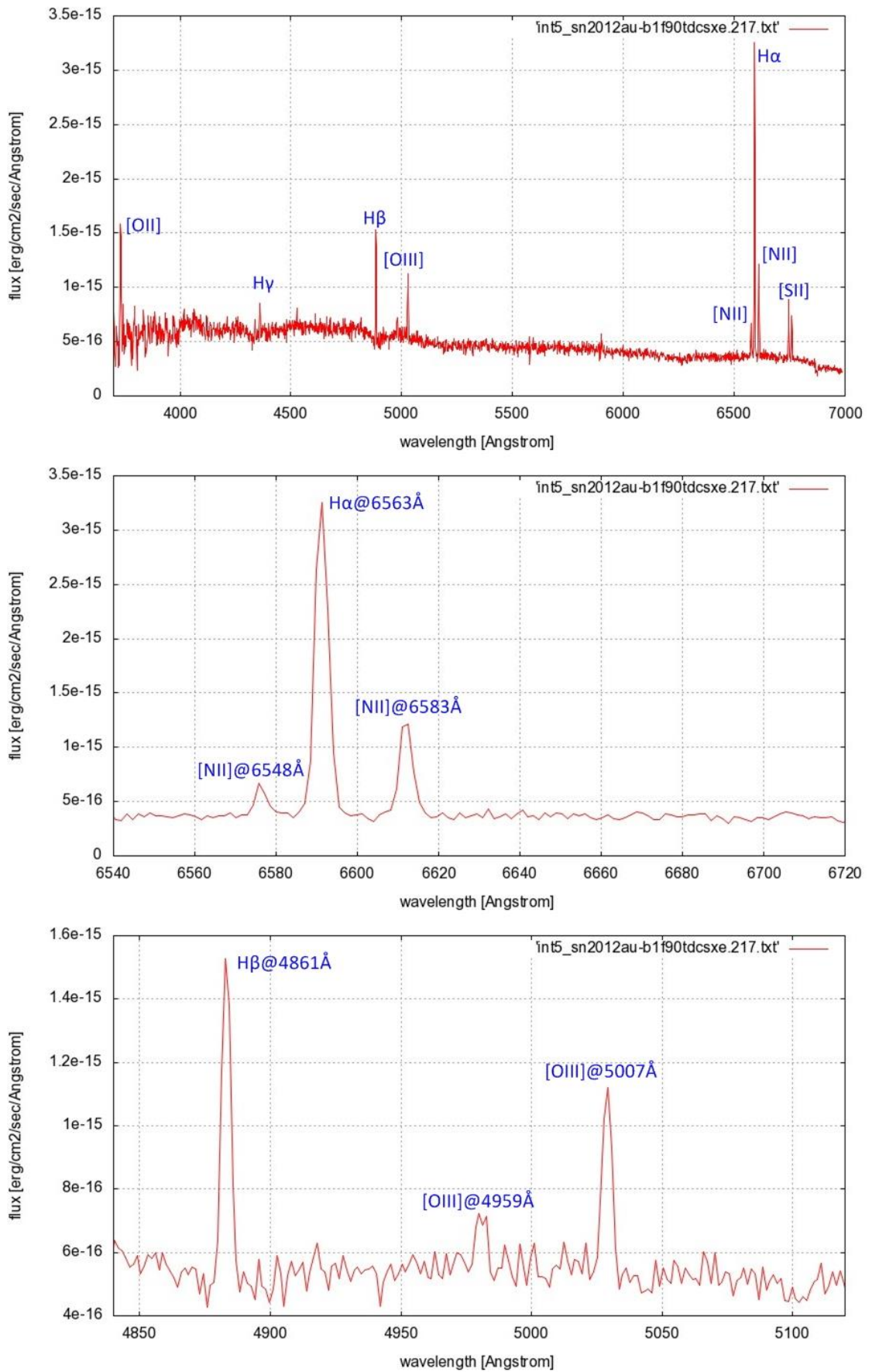
Figure 3-24: Total spectrum of Type Ib SN2012au environment (top), the Hα region (middle) and Hβ region (bottom). The indicated wavelengths are rest frame wavelengths.
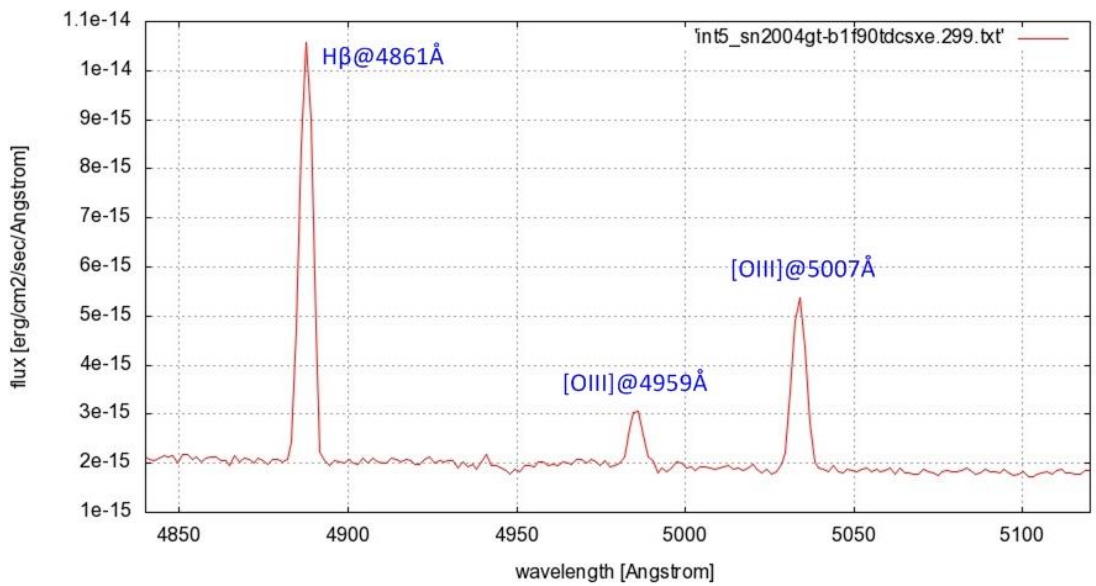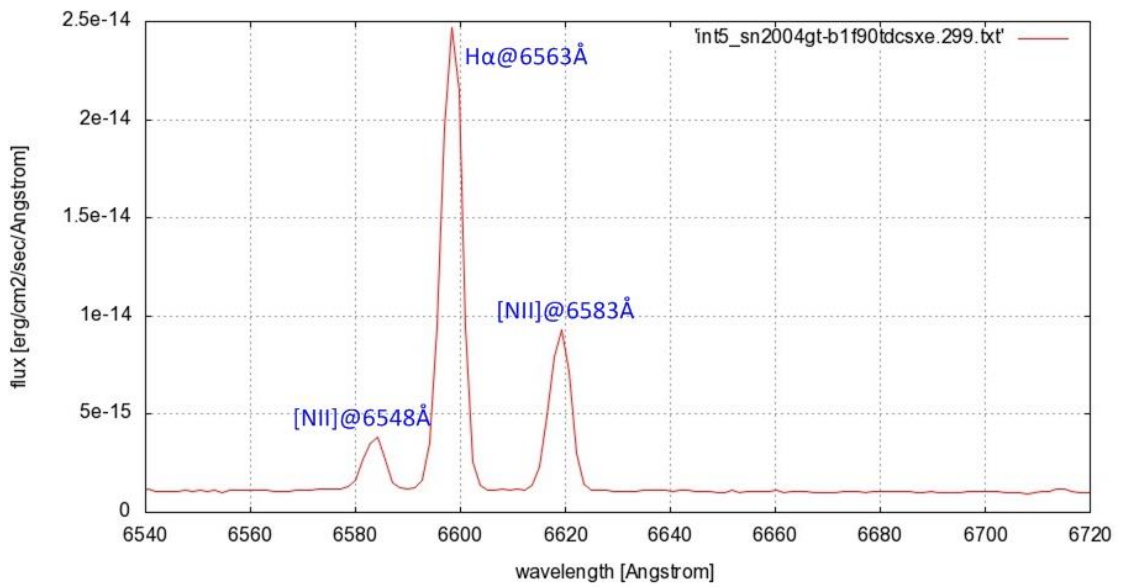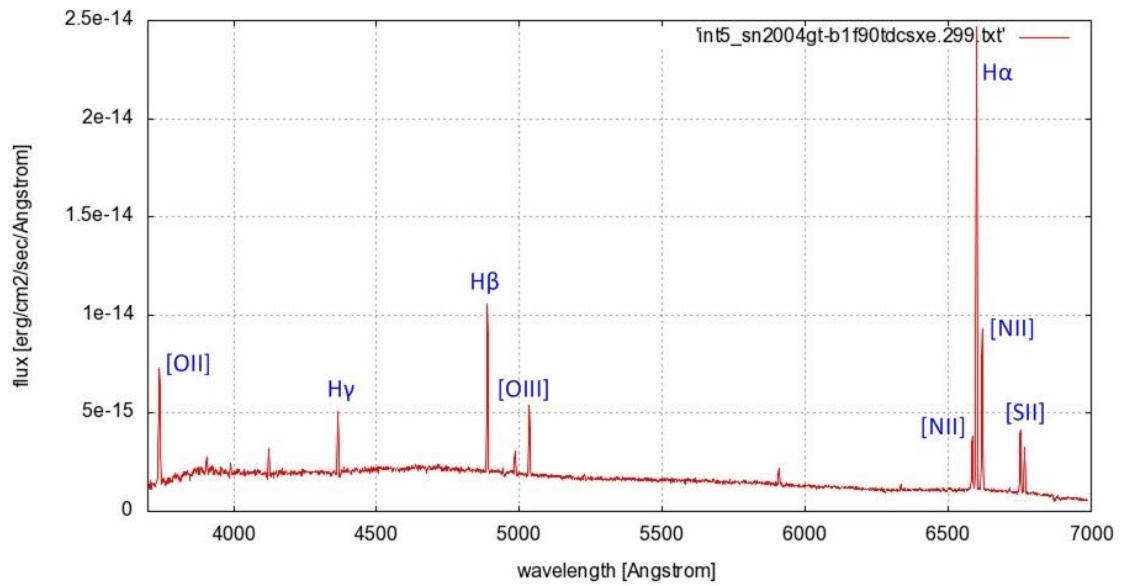
Figure 3-25: Total spectrum of Type Ic SN2004gt environment (top), the Hα region (middle) and Hβ region (bottom). The indicated wavelengths are rest frame wavelengths.
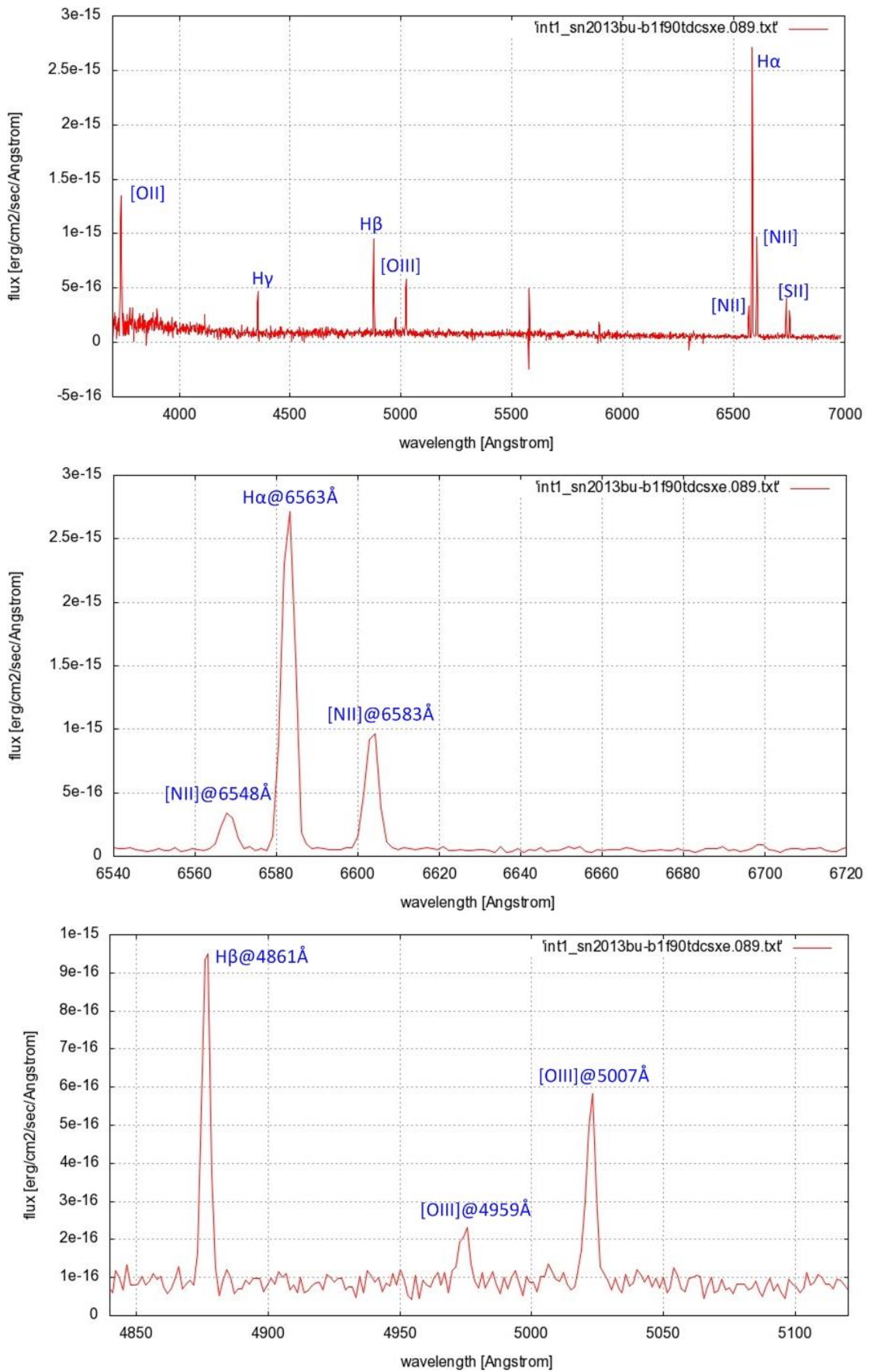
Figure 3-26: Total spectrum of Type IIP SN2013bu environment (top), the Hα region (middle) and Hβ region (bottom). The indicated wavelengths are rest frame wavelengths.

The spectrum of seven targets is peculiar in the sense that the [OIII]@5007Å intensity is greater than the Hβ (and sometimes even Hα) intensity and the [NII]@6583Å intensity is simultaneously very low (see Figure 3-27).

It is out of the focus of this thesis to go deeply in the physical conditions of HII regions, but a simple explanation of such a kind of spectrum could be: a) low density of ionising photons resulting in low hydrogen intensities; b) low density of oxygen and thus only less collisional de-excitation ($\Rightarrow$ high radiation intensity) and c) density of nitrogen higher than the critical density (de-excitation by radiation = de-excitation by collisions) for the [NII] lines ($\Rightarrow$ low radiation intensity).
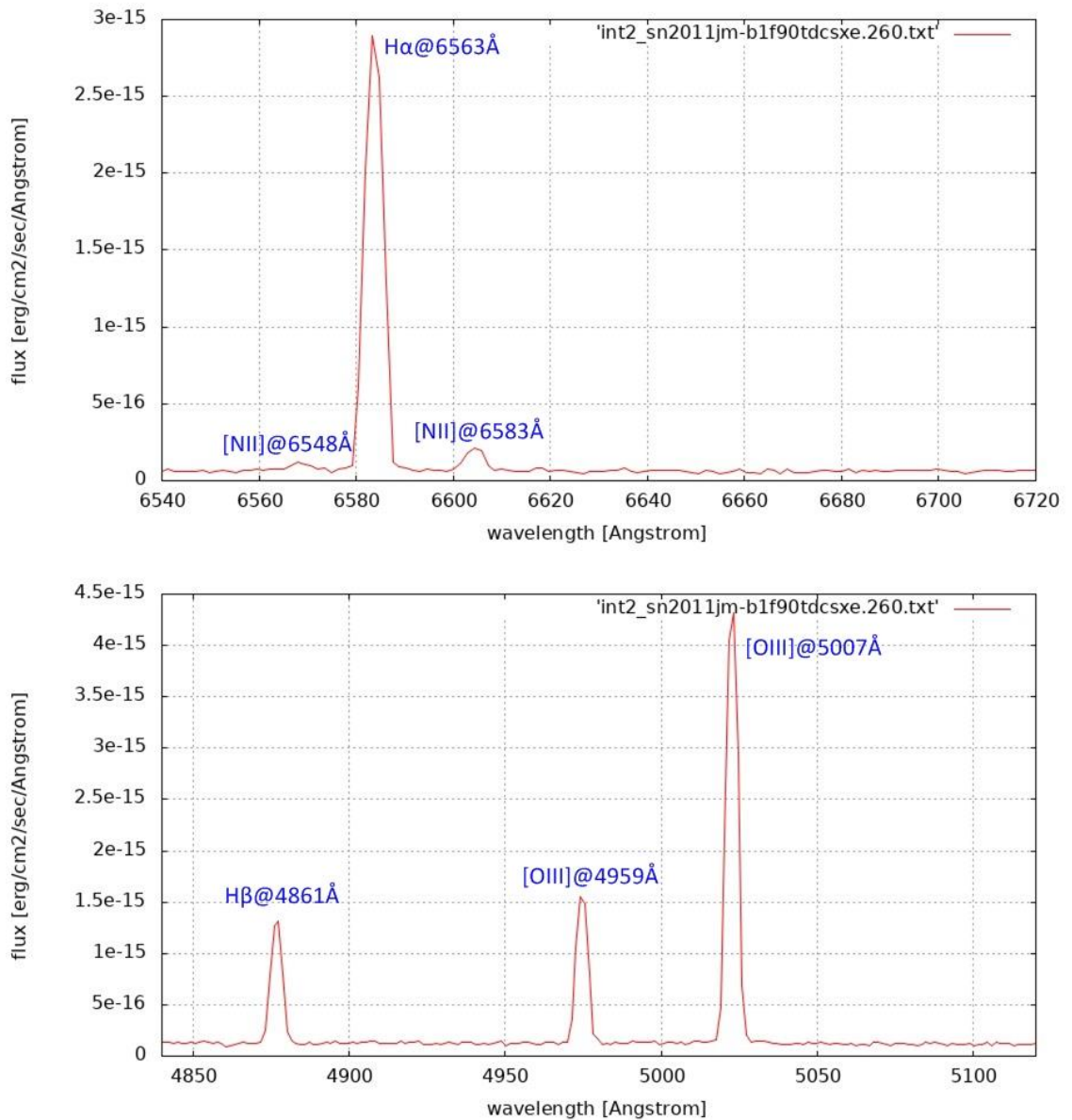
Figure 3-27: Hα region spectrum of Type Ic SN2011hm environment (top) and Hβ region (bottom). The indicated wavelengths are rest frame wavelengths.

The noise level of the observations is typically at about 1e-16 erg/cm^2/sec/Å and can be as low as 1e-17 erg/cm^2/sec/Å for the best observations. The peak intensity values of the Hα line is typically well above 1e-15 erg/cm^2/sec/Å and can be as high as 4e-14 erg/cm^2/sec/Å. Consequently, the SNR of the observations varies significantly. However DIPSO was able to handle this variability without any problems and fits the emission lines very well for the large majority of the observations (see Figure 3-28 as a typical case). The visual inspection of all DIPSO results to check the physical plausibility of the DIPSO fit prevented the evaluation of noise in cases of bad SNR (Figure 3-29).
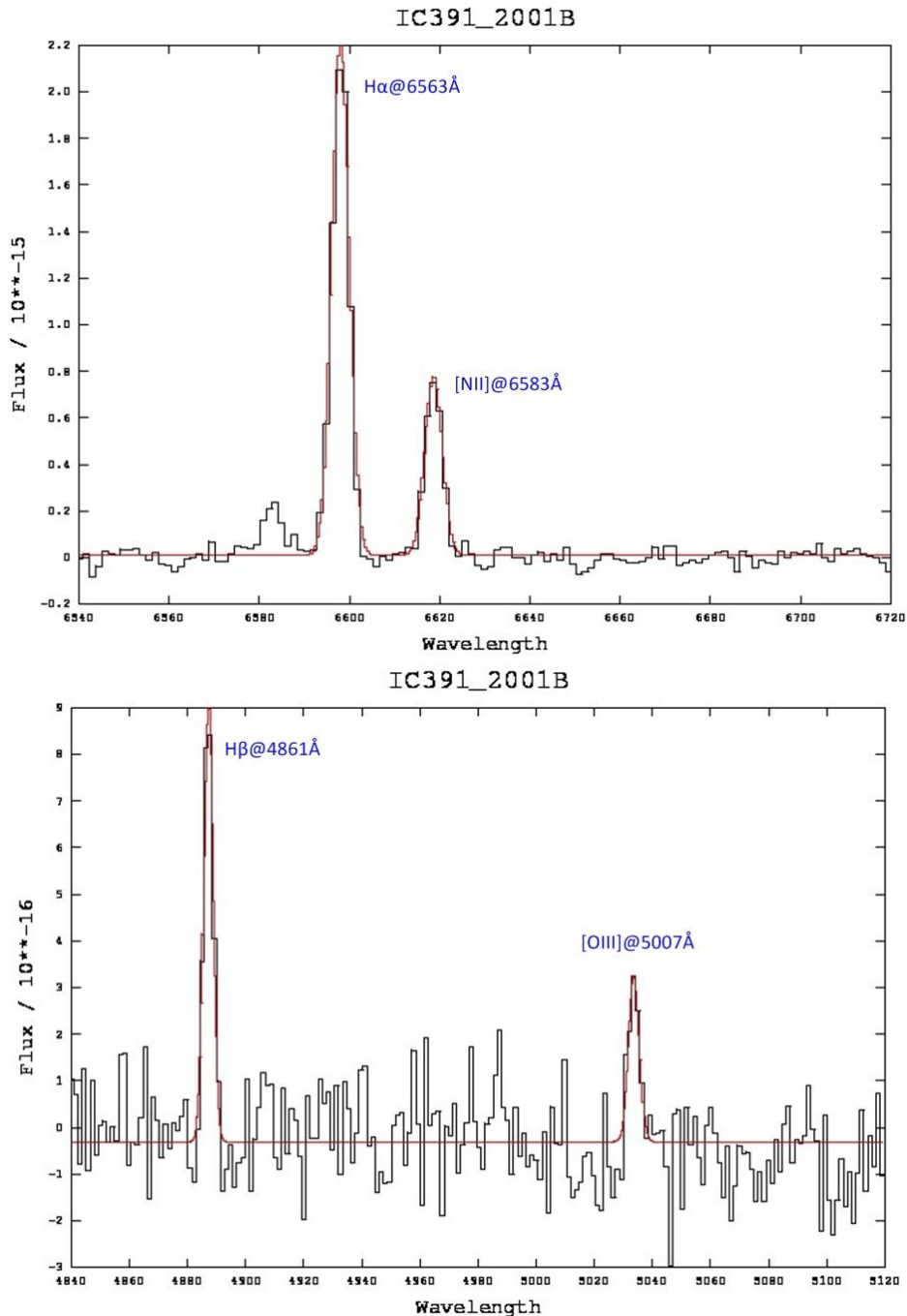
Figure 3-28: Typical example (SN2001B) of a DIPSO fit at good SNR. Top the Hα region spectrum, bottom the Hβ region of the spectrum. All required emission lines are fit very well. Indicated wavelengths are rest frame wavelengths.
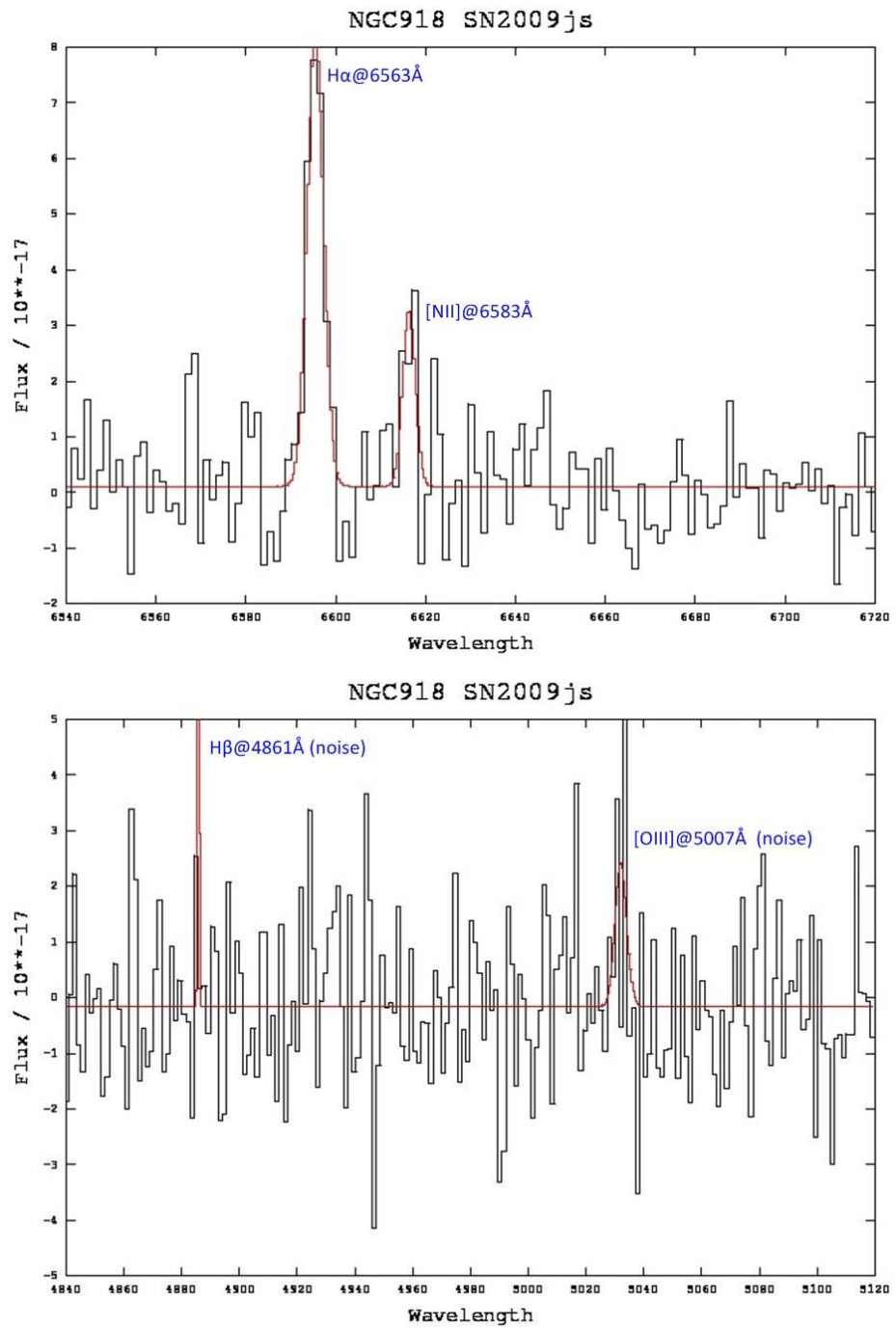
Figure 3-29: Example (SN2009js) of a DIPSO fit at bad SNR (or no emission lines). Top the Hα region spectrum, bottom the Hβ region of the spectrum. While the fit of Hα and [NII] is still reasonable, DIPSO fits to noise for Hβ and [OIII]. Indicated wavelengths are rest frame wavelengths.

Chapter 4

Results

This chapter presents the results inferred from the reduced observational data. After discussion of the uncertainties, the chapter is structured in two major parts: First, the metallicities, the cumulative distributions and statistical tests for the sample of our INT observations (Table 2-5 to Table 2-8) are shown. In the second part, the INT sample is supplemented by results of selected targets (luminosity distances less than about 30 Mpc) from previous work (see section 1.5).

4.1 Observation Statistics

In total 96 INT observations have been obtained for the project. Taking into account double (10) and triple (3) observations, INT data of 80 targets are available, of which 45 were observed first time.

Four targets (SN1990aa, SN1991ar, SN1996D and SN2009ga) do not belong to the initial sample (Table 2-1) and have luminosity distances significantly greater than 30 Mpc. They are excluded from the statistical evaluation but their results are given in Table 4-3 for completeness.

From the remaining 76 observations, five observations (SN1995bb, SN2003ie, SN2004ez, SN2005cz and SN2007od) have no visible emission lines and five targets (SN2005ad, SN2010br, SN1999ev, SN2015aq and SN2017iro) have hydrogen emission line(s) only. As result, metallicity estimation by N2 calibration was possible for 66 targets with additional estimation by O3N2 calibration for 46 of them.

4.2 Uncertainties

The interpretation of measurement results is impossible without a careful estimation of the measurement uncertainties. This section deals with the uncertainty sources and the way to quantify the uncertainties of the metallicity measurements.

4.2.1 Intrinsic Photon Noise

The received photons from the target are created in a discrete statistical process and consequently contaminated with statistical fluctuations resulting in an intrinsic noise - known as 'photon noise' - of the received photon flux. The statistical distribution that describes the photon statistics is the Poisson distribution (e.g. Eversberg and Vollmann 2015, appendix B.2).

The expectation value $E(x)$ and the variance $Var(x)$ of a Poisson process are equal. The SNR of a number of N collected photons is thus given by:

$$SNR = \frac{\text{desired signal}}{\text{noise signal}} = \frac{E(x)}{\sqrt{Var(x)}} = \frac{N}{\sqrt{N}} = \sqrt{N} \qquad \text{(Eq. 4-1)}$$

4.2.2 Detector Noise and Background Light

The CCD detector converts the collected photons to electrons which are read out by the electronics and converted to a digital signal representing the numbers of electrons per pixel. The gain factor, i.e. the conversion factor between the photo electrons and the digital count number, is in the order of unity for all observations (see Table 2-2) and set to unity in the following for simplification. The conversion process and additional background light increase the noise and the SNR after conversion is generally given by (Eversberg and Vollmann 2015):

$$SNR = \frac{N}{\sqrt{N + n(B+D) + nR^2 + Var(nB)}} \qquad \text{(Eq. 4-2)}$$

where N, B and D are the numbers of target photo-electrons, of sky background photo-electrons per pixel and of dark current electrons per pixel, respectively, measured during frame integration time; R is the read-out noise per pixel and n is the number of pixels covered by the target and its spectral range of interest. $Var(nB)$ is the variance of the background signal and represents the uncertainty in determination of the sky back-ground (usually negligible; Eversberg and Vollmann 2015).

For the actual INT/IDS observation data, the dark current D is negligible because of the detector cooling. The read-out noise R of the IDS instrument is recorded in the frame headers to be 4.2 electrons/px. Read-out noise is independent of frame exposure time and negligible if the exposure time has been chosen accordingly.

The sky background brightness at INT is about 22 mag/arcsec^2 (ING Technical Note 115[23]) for dark nights that may increase up to 4 magnitudes for full moon nights. Most of the target host galaxies have surface brightness brighter than 17 mag/arcsec^2 at half-light radius (e.g. 2MASS Galaxy Atlas[24]). Because of these bright targets, the sky background noise is dominated by the photon noise of the target.

In summary, with negligible read-out noise and sky background noise the equation (Eq. 4-2) is reduced to equation (Eq. 4-1) for most observations of the project.

4.2.3 Error Propagation throughout Data Reduction

The uncertainty caused by the noise sources discussed above propagates through all data reduction steps described in chapter 3. Thereby, each data reduction step necessarily modifies the uncertainties and usually add up additional uncertainty. At the end of the data reduction chain all particular uncertainty modifications are reflected into the final uncertainty of the emission line fluxes used to calculate the metallicities.

It is impossible to give an analytical expression that calculates how the noise at the input of the data reduction chain propagates into the uncertainty of the emission line fluxes. Empirically, the estimation of the flux uncertainty has been done by applying the data reduction process to separate error frames built by the square root of the pixel values of the obtained target frames. These error frames represent the photon noise under the condition of negligible read-out and sky background noise. Principally, read-out and sky background could be taken into account if appropriate data are available. For simplicity and lack of appropriate sky background data this has not been done.

Two points are important for reasonable uncertainty estimations by this empirical approach: 1) the data reduction process for the error frames must use exactly the same data reduction parameters as the data reduction process of the corresponding target frames and 2) the square root must not be applied to the raw target frames but to the

---

[23] http://www.ing.iac.es/Astronomy/observing/conditions/skybr/skybr.html
[24] https://irsa.ipac.caltech.edu/applications/2MASS/LGA/atlas.html

bias subtracted target frames (mean bias value comes from electronics and has nothing to do with target photons).

With the uncertainties of the emission line fluxes known by the empirical approach above, the uncertainty of the metallicity can be calculated by the Gaussian error propagation law given for a function $f(x_1,x_2,...,x_n)$ depending on n variables x_i by the equation:

$$\Delta f(x_1,...,x_n) = \sqrt{\sum_i \left(\frac{\partial f(x_1,...,x_n)}{\partial x_i}\Delta x_i\right)^2} \qquad \text{(Eq. 4-3)}$$

Precondition of (Eq. 4-3) is the statistical independence of the variables x_i that is not given because of systematic errors at least in the data reduction process. Consequently, the (Eq. 4-3) has additional covariance term(s), which is(are) negative for N2 and O3N2 calibration because the covariance of the ratio of two variables is negative (e.g. Lee and Forthofer 2006). Thus, (Eq. 4-3) provides a worst case estimation of the uncertainties.

(Eq. 4-3) applied to (Eq. 1-3) to (Eq. 1-6) of the PP04 and M13 calibrations gives:

$$\Delta N2 = \frac{|b_c|}{\ln 10}\sqrt{\left(\frac{-\Delta H\alpha}{H\alpha}\right)^2 + \left(\frac{\Delta [NII]}{[NII]}\right)^2} \qquad \text{(Eq. 4-4)}$$

and

$$\Delta O3N2 = \frac{|b_c|}{\ln 10}\sqrt{\left(\frac{\Delta H\alpha}{H\alpha}\right)^2 + \left(\frac{-\Delta [NII]}{[NII]}\right)^2 + \left(\frac{-\Delta H\beta}{H\beta}\right)^2 + \left(\frac{\Delta [OIII]}{[OIII]}\right)^2} \qquad \text{(Eq. 4-5)}$$

where $H\alpha$, $[NII]$, $H\beta$ and $[OIII]$ are the integrated emission line fluxes and their uncertainties; the constants b_c depend on calibration: $b_c = 0.57$ for PP04-N2, $b_c = 0.462$ for M13-N2, $b_c = -0.32$ for PP04-O3N2 and $b_c = -0.214$ for M13-O3N2.

The empirical error propagation and the Gaussian propagation law have been applied to all INT observations (Table 2-5 to Table 2-8). The metallicity uncertainties for all four calibration methods due to photon noise and data reduction are between 0.01 dex and about 0.11 dex. The mean value of all uncertainties is 0.03 dex, the standard deviation is 0.014 dex.

4.2.4 Calibration Uncertainties

The uncertainties estimated in section 4.2.3 are not the final uncertainties. They must be supplemented by the uncertainties of the calibrations (see section 1.4.3) that are given in the papers of Pettini and Pagel (2004) and Marino et al. (2013) as (68% confidence intervals): $\Delta PP04\text{-}N2_{calib} = 0.18$ dex, $\Delta M13\text{-}O2_{calib} = 0.16$ dex, $\Delta PP04\text{-}O3N2_{calib} = 0.14$ dex and $\Delta M13\text{-}O3N2_{calib} = 0.18$ dex.

Flux uncertainty and calibration uncertainty adds up quadratically and the total uncertainty ΔM_{total} of the metallicity is given by

$$\Delta M_{total} = \sqrt{\Delta M_{flux}^2 + \Delta M_{calib}^2} \qquad \text{(Eq. 4-6)}$$

The results for the total uncertainties of all target metallicities are listed in Table 4-1. The comparison of the calibration uncertainties above with the estimated uncertainties of the flux in section 4.2.3 shows that the total uncertainty is dominated by the calibration uncertainty. According to the calibration uncertainties mentioned above, the PP04-O3N2 method produces the results with smallest uncertainties.

4.3 INT observation results

4.3.1 Metallicities

Table 4-1 shows the calculated metallicities of the observed project targets based on N2 and O3N2 calibrations by Pettini and Pagel (2004) and Marino et al. (2013) (see section 1.4.3). The N2 metallicities for 14 Type Ib, 19 Type Ic and 33 Type IIP SNe are obtained; O3N2 metallicities could be derived for 9 Type Ib, 18 Type Ic and 19 Type IIP SNe. For uncertainty estimations see section 4.2.

Table 4-1: SN environment metallicities derived from the INT observations. PP04 are the calibrations by Pettini and Pagel (2004) and M13 are the calibrations by Marino et al. (2013) (see section 1.4.3). For uncertainty estimation see section 4.2.

SN	SN type	PP04-N2 [12+log(O/H)]	M13-N2 [12+log(O/H)]	PP04-O3N2 [12+log(O/H)]	M13-O3N2 [12+log(O/H)]
1999eh	Ib	8.61 ± 0.19	8.50 ± 0.17	-[a]	-[a]
2000ds	Ib	9.03 ± 0.18	8.85 ± 0.16	-[a]	-[a]
2001B	Ib	8.61 ± 0.18	8.51 ± 0.16	8.65 ± 0.14	8.49 ± 0.18
2002ji	Ib	8.64 ± 0.18	8.53 ± 0.16	8.74 ± 0.14	8.54 ± 0.18
2004ao	Ib	8.59 ± 0.19	8.49 ± 0.17	8.55 ± 0.15	8.41 ± 0.18
2004dk	Ib	8.44 ± 0.18	8.37 ± 0.16	8.63 ± 0.14	8.46 ± 0.18

SN	SN type	PP04-N2 [12+log(O/H)]	M13-N2 [12+log(O/H)]	PP04-O3N2 [12+log(O/H)]	M13-O3N2 [12+log(O/H)]
2004gq	Ib	8.66 ± 0.18	8.55 ± 0.16	8.80 ± 0.14	8.58 ± 0.18
2005V	Ib/c	8.71 ± 0.18	8.59 ± 0.16	8.76 ± 0.14	8.56 ± 0.18
2007C	Ib	8.71 ± 0.18	8.59 ± 0.16	8.80 ± 0.14	8.58 ± 0.18
2008D	Ib	8.55 ± 0.19	8.46 ± 0.16	8.61 ± 0.15	8.45 ± 0.18
2012au	Ib	8.60 ± 0.18	8.50 ± 0.16	8.62 ± 0.14	8.46 ± 0.18
2012P	Ib/c	8.60 ± 0.18	8.50 ± 0.16	-[b]	-[b]
2014C	Ib	8.79 ± 0.18	8.65 ± 0.16	-[a]	-[a]
2016bau	Ib	8.65 ± 0.19	8.54 ± 0.17	-[b]	-[b]
2000ew	Ic	8.60 ± 0.18	8.50 ± 0.16	8.99 ± 0.14	8.71 ± 0.18
2001ci	Ic	8.71 ± 0.18	8.59 ± 0.16	8.79 ± 0.14	8.57 ± 0.18
2002jz	Ic	8.29 ± 0.20	8.25 ± 0.17	8.24 ± 0.15	8.21 ± 0.18
2004bm	Ic	8.68 ± 0.18	8.56 ± 0.16	8.97 ± 0.14	8.69 ± 0.18
2004C	Ic	8.63 ± 0.18	8.52 ± 0.16	8.72 ± 0.14	8.52 ± 0.18
2004gk	Ic	8.60 ± 0.19	8.50 ± 0.16	8.59 ± 0.15	8.44 ± 0.18
2004gn	Ic	8.62 ± 0.18	8.51 ± 0.16	8.89 ± 0.14	8.64 ± 0.18
2004gt	Ic	8.63 ± 0.18	8.53 ± 0.16	8.71 ± 0.14	8.52 ± 0.18
2005kl	Ic	8.61 ± 0.18	8.51 ± 0.16	8.73 ± 0.14	8.53 ± 0.18
2007gr	Ic	8.60 ± 0.18	8.50 ± 0.16	8.77 ± 0.14	8.56 ± 0.18
2009em	Ic	8.63 ± 0.18	8.52 ± 0.16	8.73 ± 0.14	8.53 ± 0.18
2010io	Ic	8.36 ± 0.19	8.31 ± 0.16	8.29 ± 0.14	8.24 ± 0.18
2011jm	Ic	8.17 ± 0.18	8.15 ± 0.16	8.14 ± 0.14	8.14 ± 0.18
2012cw	Ic	9.00 ± 0.19	8.83 ± 0.17	-[a]	-[a]
2012fh	Ic	8.57 ± 0.18	8.47 ± 0.16	8.57 ± 0.14	8.43 ± 0.18
2013dk	Ic	8.70 ± 0.18	8.58 ± 0.16	8.85 ± 0.14	8.61 ± 0.18
2013ff	Ic	8.61 ± 0.18	8.51 ± 0.16	8.64 ± 0.14	8.47 ± 0.18
2013ge	Ic	8.54 ± 0.19	8.45 ± 0.16	8.50 ± 0.15	8.38 ± 0.18
2017ein	Ic	8.63 ± 0.18	8.52 ± 0.16	8.84 ± 0.14	8.61 ± 0.18
1998bv	IIP	8.22 ± 0.19	8.19 ± 0.17	8.21 ± 0.15	8.19 ± 0.18
1998dl	IIP	8.62 ± 0.18	8.52 ± 0.16	8.72 ± 0.14	8.52 ± 0.18
1999em	IIP	8.93 ± 0.18	8.77 ± 0.16	-[a]	-[a]
1999gi	IIP	8.51 ± 0.18	8.42 ± 0.16	-[b]	-[b]
2001fv	IIP	8.86 ± 0.19	8.71 ± 0.16	-[b]	-[b]
2002hh	IIP	8.63 ± 0.18	8.52 ± 0.16	8.74 ± 0.14	8.54 ± 0.18
2003gd	IIP	8.83 ± 0.19	8.68 ± 0.17	-[a]	-[a]
2003J	IIP	8.81 ± 0.18	8.67 ± 0.16	-[a]	-[a]
2003Z	IIP	8.66 ± 0.18	8.55 ± 0.16	8.53 ± 0.14	8.40 ± 0.18
2004A	IIP	8.59 ± 0.18	8.50 ± 0.16	-[a]	-[a]
2004dg	IIP	8.64 ± 0.18	8.53 ± 0.16	8.96 ± 0.14	8.68 ± 0.18
2004dj	IIP	8.61 ± 0.19	8.50 ± 0.16	8.47 ± 0.14	8.36 ± 0.18
2004fc	IIP	8.66 ± 0.18	8.55 ± 0.16	8.78 ± 0.14	8.56 ± 0.18
2005ay	IIP	8.68 ± 0.19	8.56 ± 0.17	8.81 ± 0.15	8.59 ± 0.18
2005cs	IIP	8.52 ± 0.18	8.44 ± 0.16	-[b]	-[b]
2006bp	IIP	8.65 ± 0.18	8.54 ± 0.16	8.75 ± 0.14	8.54 ± 0.18
2007aa	IIP	8.61 ± 0.19	8.50 ± 0.17	8.68 ± 0.15	8.50 ± 0.18

SN	SN type	PP04-N2 [12+log(O/H)]	M13-N2 [12+log(O/H)]	PP04-O3N2 [12+log(O/H)]	M13-O3N2 [12+log(O/H)]
2007av	IIP	8.72 ± 0.18	8.59 ± 0.16	-[b]	-[b]
2008X	IIP	8.33 ± 0.19	8.28 ± 0.17	8.29 ± 0.15	8.24 ± 0.18
2009js	IIP	8.59 ± 0.19	8.49 ± 0.17	-[a]	-[a]
2011ck	IIP	8.55 ± 0.19	8.46 ± 0.16	8.57 ± 0.15	8.43 ± 0.18
2011dq	IIP	8.42 ± 0.18	8.36 ± 0.16	8.38 ± 0.14	8.30 ± 0.18
2012A	IIP	8.23 ± 0.18	8.20 ± 0.16	8.16 ± 0.14	8.15 ± 0.18
2012bv	IIP	8.70 ± 0.19	8.58 ± 0.16	8.66 ± 0.15	8.48 ± 0.18
2012ec	IIP	8.63 ± 0.18	8.52 ± 0.16	8.67 ± 0.14	8.50 ± 0.18
2013ab	IIP	8.69 ± 0.18	8.57 ± 0.16	-[b]	-[b]
2013bu	IIP	8.64 ± 0.18	8.53 ± 0.16	8.67 ± 0.14	8.49 ± 0.18
2013ej	IIP	8.80 ± 0.19	8.66 ± 0.17	-[a]	-[a]
2014A	IIP	8.67 ± 0.19	8.55 ± 0.16	-[b]	-[b]
2014bc	IIP	8.95 ± 0.18	8.78 ± 0.16	-[c]	-[c]
2014bi	IIP	8.72 ± 0.19	8.60 ± 0.16	-[a]	-[a]
2014cx	IIP	8.43 ± 0.18	8.36 ± 0.16	8.35 ± 0.14	8.28 ± 0.18
2015V	IIP	8.42 ± 0.18	8.36 ± 0.16	8.37 ± 0.14	8.29 ± 0.18

notes: O3N2 method not applicable because   a: no Hβ and no [OIII] line
b: Hβ present, no [OIII] line
c: [OIII] line present, no Hβ line

Table 4-2 list the unweighted means (uncertainties for a particular calibration are almost constant) and the standard deviations of the metallicities for the different SN types and for the total sample. The differences in the mean of the metallicities are small for all cases. For the standard deviations of the O3N2 calibrations, a large difference between the value of Type Ib and the two other types is remarkable. This is true for N2 calibration also, especially if the outlier SN2000ds (Ca-rich Type Ib SN, Perets et al. 2010) would be excluded (σ(PP04-N2) would change from 0.13 to 0.09 without SN2000ds; σ(M13-N2) from 0.11 to 0.07). See chapter 5 for a discussion of possible physical reasons of this narrower distribution of the Type Ib SNe metallicities.

Table 4-2: Number of targets N, mean value and standard deviation σ of metallicities for the three SN types derived from INT observations.

SN type	N(N2)	PP04-N2 [12+log(O/H)]		M13-N2 [12+log(O/H)]		N(O3N2)	PP04-O3N2 [12+log(O/H)]		M13-O3N2 [12+log(O/H)]	
		mean	σ	mean	σ		mean	σ	mean	σ
Ib	14	8.66	0.13	8.54	0.11	9	8.68	0.09	8.50	0.06
Ic	19	8.59	0.17	8.49	0.14	18	8.66	0.24	8.49	0.16
IIP	33	8.62	0.17	8.52	0.14	19	8.57	0.22	8.42	0.15
all	66	8.62	0.16	8.52	0.13	46	8.63	0.21	8.46	0.14
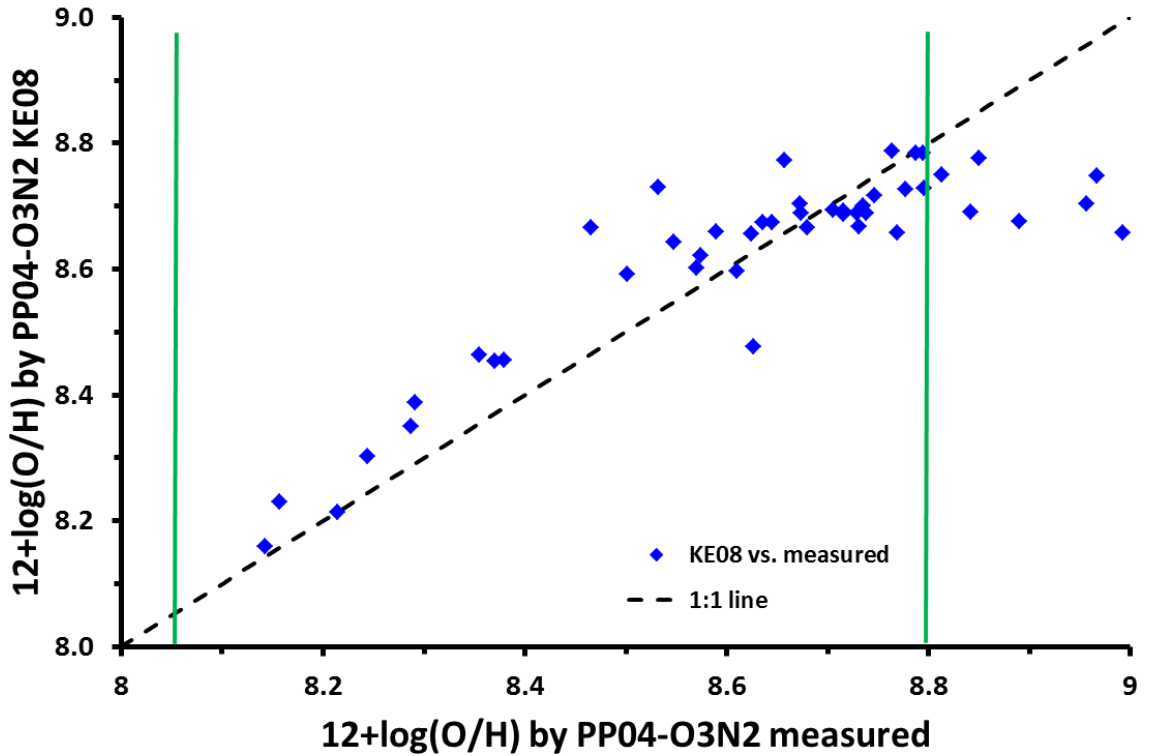
Figure 4-1: Scatter plot of PP04-O3N2 metallicities as predicted by the relation of Kewley and Ellison (2008, KE08) from our PP04-N2 values vs. our measured PP04-O3N2 metallicities. The dashed black line is the 1:1 line and the vertical green lines mark the validity range of the KE08 relation (8.05 - 8.8 dex) between PP04-N2 and PP04-O3N2. Significant deviations from 1:1 line are visible even if mostly within the uncertainty range of the measured values (about ±0.14 dex, see Table 4-1).

Kewley and Ellison (2008) proposed relations between strong emission line calibrations for the conversion of one calibration to another one by cubic polynomials. It has been checked if this works for conversion from N2 to the O3N2 method to estimate missing O3N2 values of targets without Hβ/[OIII] emission. The test using targets with metallicity values inferred from both the N2 and the O3N2 method revealed that the proposed relation fails for many targets (Figure 4-1, deviation up to 0.3 dex). The method by Kewley and Ellison (2008) has therefore not been applied (see also section 5.2.3).

For completeness, Table 4-3 shows the metallicities of the observations of SN1990aa, SN1991ar, SN1996D and SN2009ga excluded from statistics because the luminosity distance significantly larger than 30 Mpc. There is no remarkable difference to the metallicities of Table 4-1.

Table 4-3: For completeness, the metallicities of the four INT observations excluded ($D_L \gg 30$Mpc) from the statistical evaluation.

SN	SN type	PP04-N2 [12+log(O/H)]	M13-N2 [12+log(O/H)]	PP04-O3N2 [12+log(O/H)]	M13-O3N2 [12+log(O/H)]
1990aa	Ic	8.47 ± 0.18	8.40± 0.16	8.49± 0.14	8.37 ± 0.18
1991ar	Ib	8.59 ± 0.19	8.49 ± 0.17	8.56 ± 0.15	8.42 ± 0.18
1996D	Ic	8.65 ± 0.18	8.54 ± 0.16	8.61 ± 0.14	8.45 ± 0.18
2009ga	IIP	8.65 ± 0.19	8.54 ± 0.16	8.74 ± 0.14	8.54 ± 0.18

Figure 4-2 to Figure 4-5 show the normalised cumulative distribution functions (CDFs) of the results of the four calibrations used in Table 4-1. There seems to be clear tendencies in the CDFs estimated by O3N2 calibration (Figure 4-4/Figure 4-5): firstly, the metallicity of Type Ic environments show a tendency to be higher (about 0.1 dex, see Table 4-2) than that of Type IIP and, secondly, the distribution of Type Ib is significantly narrower (spanning about 0.22 dex compared to about 0.55 dex) than the two other types. The first tendency is not confirmed by the N2 calibrations (Figure 4-2/Figure 4-3) but the narrower distribution of Type Ib is still visible especially if the N2-outlier SN2000ds (12+log(O/H): 9.03 and 8.85, respectively) would be excluded.
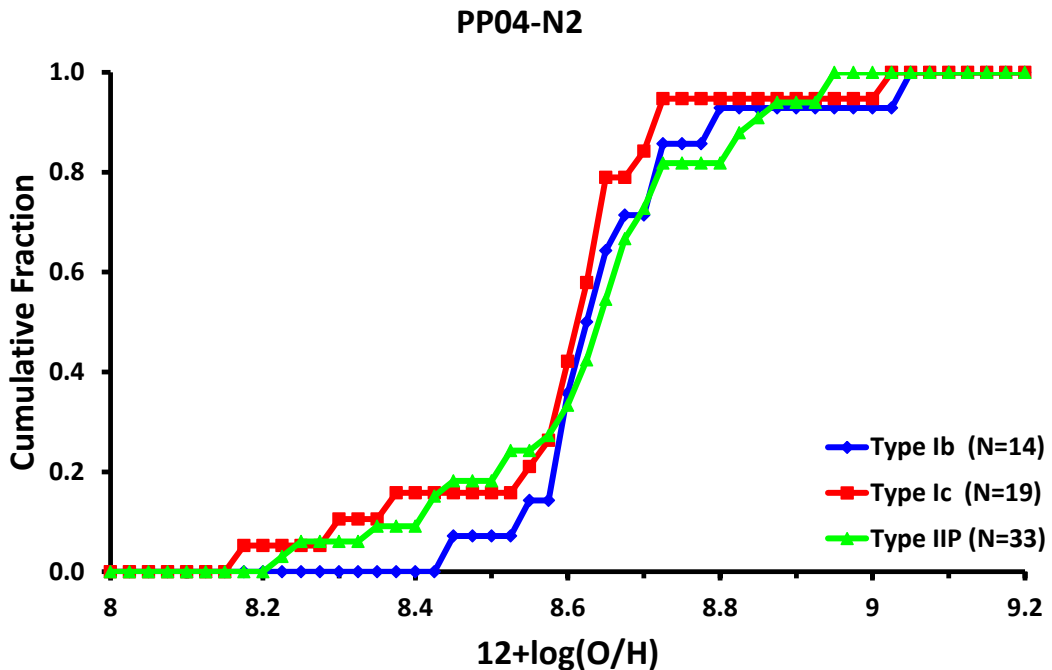
Figure 4-2: CDFs of the SN environment metallicities measured with the N2 calibration of Pettini and Pagel (2004). Binning width for CDF calculation: 0.025 dex.
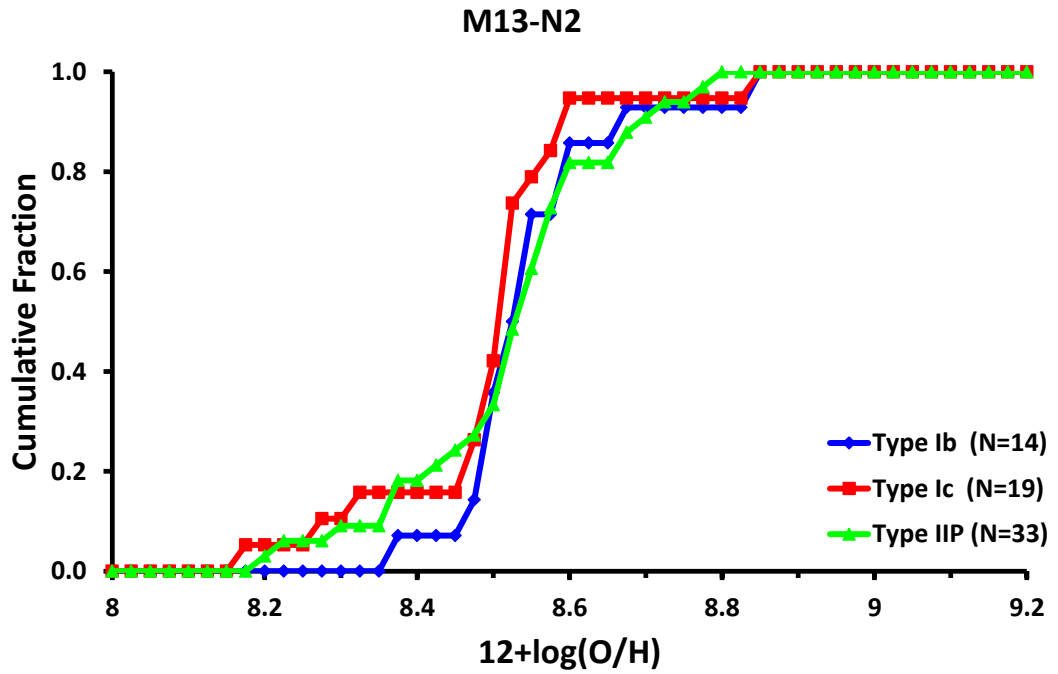
Figure 4-3: CDFs of the SN environment metallicities measured with the N2 calibration of Marino et al. (2013). Binning width for CDF calculation: 0.025 dex.
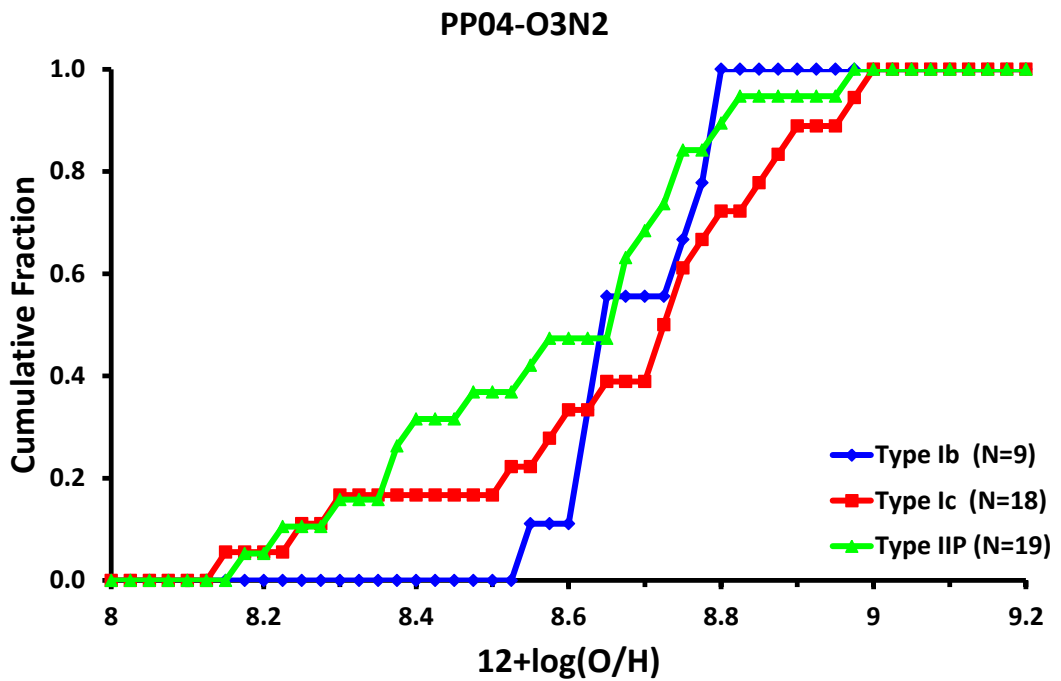
Figure 4-4: CDFs of the SN environment metallicities measured with the O3N2 calibration of Pettini and Pagel (2004). Binning width for CDF calculation: 0.025 dex.
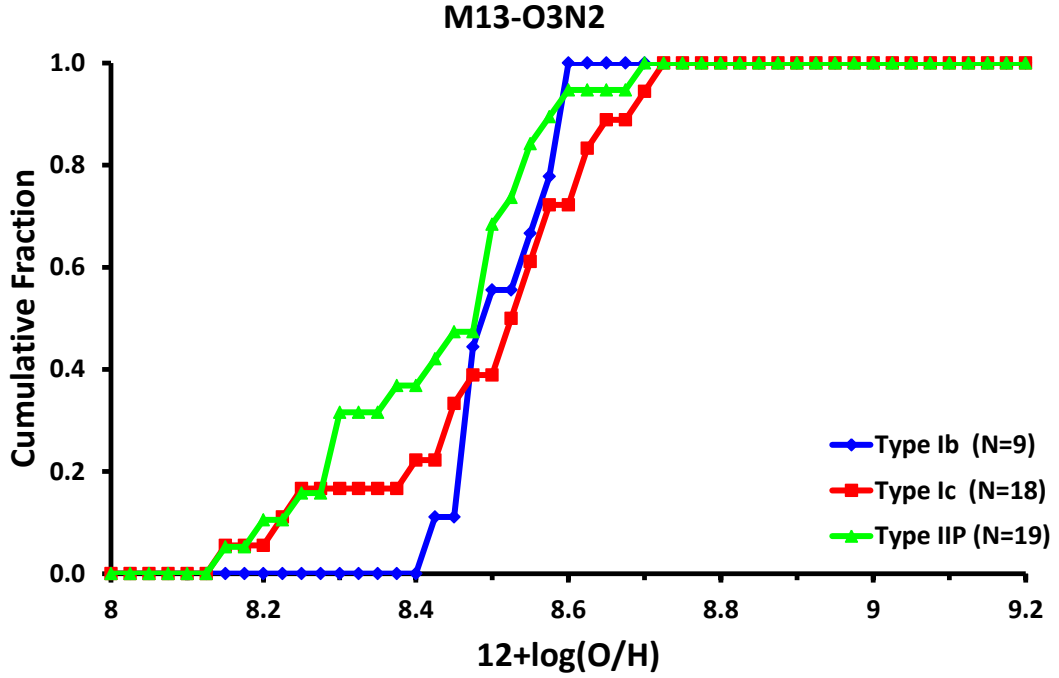
Figure 4-5: CDFs of the SN environment metallicities measured with the O3N2 calibration of Marino et al. (2013). Binning width for CDF calculation: 0.025 dex.

4.3.2 Kolmogoroff-Smirnow Test

In order to check a statistically significant difference between the samples of the different SN-types, two statistical tests have been applied: the two-sample Kolmogorov-Smirnow test (KS-test) and the two-sample Anderson-Darling test (AD-test, section 4.3.3). Both tests are applicable for small samples with single-digit sizes (see e.g. tables in Massey 1952 and Pettitt 1976).

The two-sample KS-test (e.g. Press 1988) checks the null hypothesis that two discrete samples are drawn from same parent population. It checks the differences between the two discrete samples by evaluation of the supremum D of the distances between CDFs $F_n(x)$ and $G_m(x)$ (here these would be e.g. Type Ib and Ic distributions) of two samples with sizes n and m, respectively (Figure 4-6):

$$D = \sup_x |F_n(x) - G_m(x)| \qquad \text{(Eq. 4-7)}$$

If the value of the supremum exceeds a critical value D_{crit}, the null hypothesis will be rejected and the two samples do not have the same parent population at certain significance.
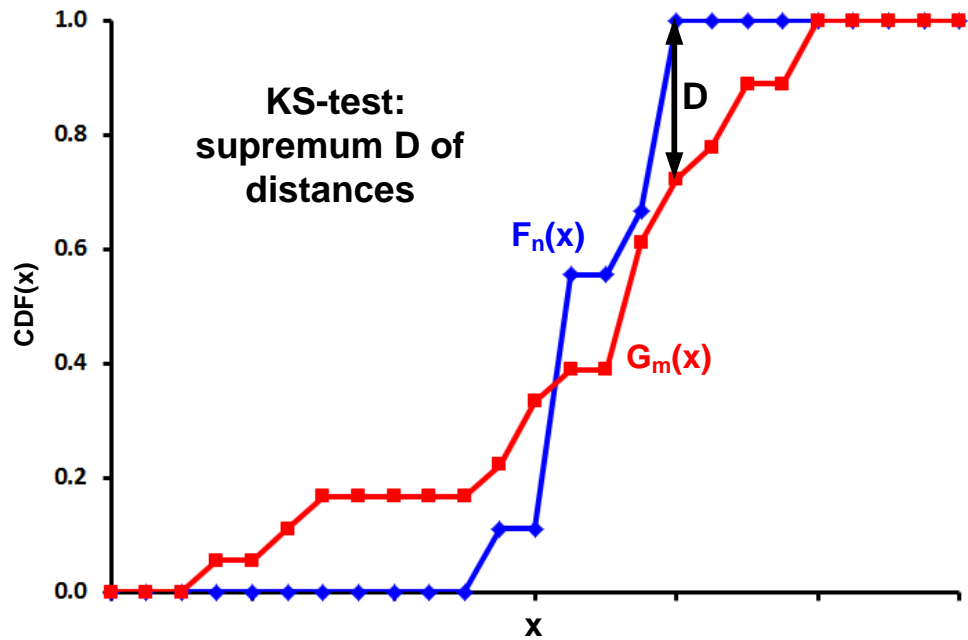
Figure 4-6: Schematic chart for visualisation of the KS-test. It uses just the supremum of the absolute values of the distances between the two CDFs to test the null hypothesis.

The value of D_{crit} is calculated by the Kolmogorov distribution (Marsaglia et al. 2003) and depends on the significance level α (usually 5% or 1%) and the sizes n and m of the two samples. The values for small n,m are tabulated (Massey 1952). For sizes n,m > ~10, D_{crit} can be calculated by the approximation

$$D_{crit} = c(\alpha)\sqrt{\frac{n+m}{nm}} \qquad \text{(Eq. 4-8)}$$

where $c(\alpha) = 1.36$ for significance level $\alpha = 5\%$ and 1.63 for $\alpha = 1\%$ (e.g. Kreyszig 1998).

The two-sample KS-test is implemented in major statistical software packages providing slightly different results depending on implementation. This work uses the implementation of the two-sample KS-test in the package 'twosamples'[25] of the statistical software called 'R' (R-project[26]). The statistical tests of the package 'twosamples' are not based on tables to calculate the p-value of the given samples but perform real permutations between the samples to evaluate the p-value (see appendix A.2 for details). The meaning of the p-value is same as usual in statistics: the null hypothesis (both samples have same parent population) must be rejected if p-value is less than the chosen significance level α.

[25] https://github.com/cdowd/twosamples
[26] https://www.r-project.org/

78

Table 4-4: P-values of the two-sample KS-test for the INT observations calculated by the R-function 'ks_test' (number of permutations: two millions). All p-values exceed the chosen significance level of 5% and the null hypothesis cannot be rejected.

SN types	PP04-N2 p-value	M13-N2 p-value	PP04-O3N2 p-value	M13-O3N2 p-value
Ib-Ic	0.375	0.583	0.726	0.704
Ib-IIP	0.778	0.760	0.139	0.128
Ic-IIP	0.131	0.278	0.316	0.309

Table 4-4 lists the KS-test p-value results of the sample combinations Ib-Ic, Ib-IIP and Ic-IIP for all four metallicity calibrations. The p-value for a significance level of 5% should be <0.05 to reject the null hypothesis. The p-values in Table 4-4 are all significantly greater than 0.05 and thus the null hypothesis (same parent population) must not be rejected. The KS-test detects no statistically significant difference of the SN environment metallicity between the different SN subtypes.

The result of the KS-test is surprising, especially for the case Ib-Ic with obviously different standard deviations and thus widths of the frequency distributions. It raises the question if the KS-test is able to distinguish distributions with same mean but significant different standard deviation (see chapter 5 for further discussion).

4.3.3 Anderson-Darling Test

The two-sample AD-test (Pettitt 1976) is an alternative statistical test to the two-sample KS-test. While the KS-test evaluates just the supremum of the distances between the CDFs of the two samples, the AD-test take into account all distances between the two CDFs (Figure 4-7). Consequently, differences in the tails of the CDFs are more weighted and the AD-test judges more the area between the CDFs than just a maximum value.

Mathematically, the two-sample AD-test calculates a value A_{nm}^2 by (Pettitt 1976):

$$A_{nm}^2 = \frac{nm}{N} \int_{-\infty}^{\infty} \frac{\{F_n(x) - G_m(x)\}^2}{H_N(x)\{1 - H_N(x)\}} \, dH_N(x) \qquad \text{(Eq. 4-9)}$$

where $F_n(x)$ and $G_m(x)$ are the CDFs of the two samples with sizes n and m, $N = n + m$ and $H_N(x)$ is the CDF of the combined sample of the two samples given by (Pettitt 1976):

$$H_N(x) = \{nF_n(x) + mG_m(x)\}/N \qquad \text{(Eq. 4-10)}$$
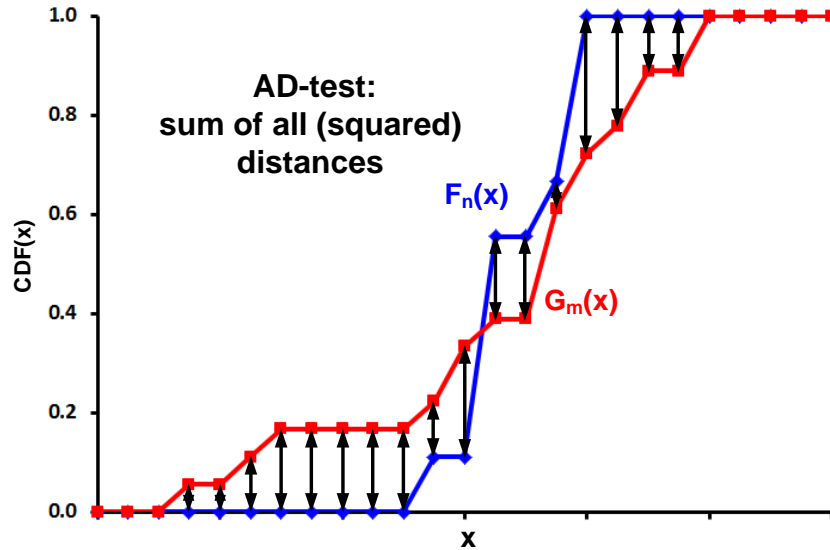
Figure 4-7: Schematic chart for visualisation of the AD-test. It uses the sum of all (squared) distances between the two CDFs to judge the null hypothesis. Compared with KS-test, it is more sensitive to differences in the tails.

Table 4-5: P-values of the two-sample AD-test for the INT observations calculated by the R-function 'ad_test' (number of permutations: two millions). All p-values exceed the chosen significance level of 5% and the null hypothesis cannot be rejected.

SN types	PP04-N2 p-value	M13-N2 p-value	PP04-O3N2 p-value	M13-O3N2 p-value
Ib-Ic	0.434	0.448	0.426	0.484
Ib-IIP	0.625	0.677	0.192	0.138
Ic-IIP	0.413	0.452	0.223	0.257

Like the two-sample KS-test, the two-sample AD-test rejects the null hypothesis of same parent population if the value A_{nm}^2 exceeds a critical value A_{crit} depending on significance level α. Values of A_{crit} for different levels α and sizes n, m are tabulated in the literature (e.g. Pettitt 1976).

The implementation of the two-sample AD-test used in this work is also from R-project package 'twosamples' (see section 4.3.2). Like KS-test the AD-test of 'twosamples' is based on real permutations to evaluate the p-value of the samples.

Table 4-5 lists the estimated p-values of the two-sample AD-tests for all sample combinations Ib-Ic, Ib-IIP and Ic-IIP for all four metallicity calibrations. The calculated p-values are all definitively greater than 0.05 for a significance level of 5%. Thus, again, the null hypothesis of same parent population must not be rejected. There is no

statistical significance that metallicities of the environments of the different SN-types are different. The results of two-sample KS-test and two-sample AD-test are consistent.

4.4 Sample Extension by Previous Results

The sample of SNe obtained by INT observations has been extended by SNe from previous work (see section 1.5). Only targets of previous work which meet the selection criteria of section 2.1 have been selected for the sample extension.

4.4.1 Targets of Previous Work within 30 Mpc

The previous work used for sample extension is listed in Table 1-3. All new targets for the extension had to be Type IIP, Type Ib or Type Ic; all other SN types have been ignored. Also, the maximum luminosity distance was limited to less than 30 Mpc (within the uncertainty range).

Table 4-6: List of additional targets from previous work as extension of Table 2-1. Morphology, radial velocity, absolute magnitude and redshift are taken from NED, SN type and luminosity distance from Open Supernova Catalogue.

SN	SN type	galaxy	morphology	D_L [Mpc]	v_r [km/s]	M_V	redshift
1962L	Ic	NGC1073	SB(rs)c	4.3	1208	-19.0	0.00403
1964L	Ic	NGC3938	SA(s)c	18.0	809	-20.7	0.00270
1982R	Ib	NGC1187	SB(r)c	18.0	1390	-21.2	0.00464
1983I	Ic	NGC4051	SAB(rs)bc	13.0	700	-21.3	0.00234
1983K	IIP	NGC4699	SAB(rs)b	24.0	1394	-22.0	0.00465
1983N	Ib	NGC5236	SAB(s)c	4.3	513	-21.5	0.00171
1984L	Ib	NGC991	SAB(rs)c	18.0	1532	-16.8	0.00511
1985F	Ib	NGC4618	SB(rs)m	7.0	544	-19.4	0.00181
1985G	IIP	NGC4451	Sbc	27.0	864	-20.6	0.00288
1985P	IIP	NGC1433	SB(r)ab	9.0	1076	-20.6	0.00359
1986L	IIP	NGC1559	SB(s)cd	14.0	1304	-21.3	0.00435
1987M	Ic	NGC2715	SAB(rs)c	16.0	1339	-21.4	0.00447
1988L	Ib	NGC5480	SA(s)c	27.5	1856	-21.3	0.00619
1990E	IIP	NGC1035	SA(s)c	18.0	2141	-19.0	0.00414
1990H	IIP	NGC3294	SA(s)c	27.0	1586	-22.2	0.00529
1990K	IIP	NGC150	SB(rs)b	20.0	1584	-21.2	0.00528
1991N	Ic	NGC3310	SAB(r)bc	19.0	993	-20.5	0.00331
1992ba	IIP	NGC2082	SB(r)b	14.0	1184	-19.8	0.00395
1994I	Ic	NGC5194	SA(s)bc	6.1	463	-20.9	0.00154
1996aq	Ic	NGC5584	SAB(rs)cd	19.0	1638	-21.0	0.00546
1996N	Ib	NGC1398	SB(r)ab	8.0	1396	-22.5	0.00466
1997dq	Ic	NGC3810	SA(rs)c	16.0	992	-21.4	0.00331
1997X	Ib	NGC4691	SB(s)a	5.2	1110	-20.4	0.00370
1999bg	IIP	IC758	SB(rs)cd	26.0	1275	-18.5	0.00425
1999br	IIP	NGC4900	SB(rs)c	20.0	960	-20.6	0.00320

SN	SN type	galaxy	morphology	D_L [Mpc]	v_r [km/s]	M_V	redshift
1999dn	Ib	NGC7714	SB(s)b	36.0*	2798	-21.1	0.00933
1999ec	Ib	NGC2207	SAB(rs)bc	16.0	2741	-21.3	0.00914
1999eu	IIP	NGC1097	SB(s)b	25.0	1105	-23.0	0.00424
2000cb	IIP	IC1158	SAB(r)c	24.0	1927	-21.0	0.00643
2001ef	Ic	IC381	SAB(rs)bc	25.0	2476	-20.8	0.00826
2003gf	Ic	MGC-04-52-26	IB(s)m	38.8*	2600	-18.1	0.00867
2003hl	IIP	NGC772	SA(s)b	18.0	2472	-22.9	0.00825
2005at	Ic	NGC6744	SAB(r)bc	7.3	841	-21.8	0.00281
2005az	Ic	NGC5194	SA(s)bc	6.1	463	-20.9	0.00154
2007oc	IIP	NGC7418A	SA(rs)d	25.0	2102	-21.2	0.00701
2007uy	Ib	NGC2770	SA(s)c	26.0	1947	-21.7	0.00649
2009jf	Ib	NGC7479	SB(s)c	31.0	2381	-22.6	0.00794
2010F	IIP	NGC3120	SAB(s)bc	38.0*	2791	-21.2	0.00931
2011cj	IIP	UGC9356	S?	32.9	2224	-20.0	0.00742
2011gv	IIP	IC4901	SAB(rs)c	31.6	2138	-21.6	0.00713
2012ho	IIP	MGC-01-57-21	SB(s)bc	44.1*	2970	-21.1	0.00991

*large uncertainty with lower limit of distance range <30Mpc

Table 4-6 shows the targets from previous work meeting the selection criteria. The additional targets extend the target list (Table 2-1) of chapter 2 by 41 new targets: 11 Type Ib, 12 Type Ic and 18 Type IIP SNe. The total sample size of selected targets increases from 110 to 151 (33 Type Ib, 35 Type Ic and 83 Type IIP SNe). The number of observed targets increases from 76 to 117 (28 Type Ib, 32 Type Ic and 57 Type IIP SNe) improving the statistical validity of the sample.

4.4.2 Metallicities

Table 4-7 presents the metallicities of SNe environments found in previous work. It includes results of the 41 new targets above plus results of 10 southern hemisphere targets listed in Table 2-1 that could not be observed at the INT.

The previous work used PP04 or M13 calibration for metallicity measurement. Some work used N2 or O3N2 only, others N2 and O3N2. Rearrangement of equations (Eq. 1-3) and (Eq. 1-4) gives a relation between PP04-N2 and M13-N2 calibration to convert the results from one calibration to the other:

$$M13\text{-}N2 = 1.529 + 0.811 \times PP04\text{-}N2 \qquad \text{(Eq. 4-11)}$$

$$PP04\text{-}N2 = -1.887 + 1.234 \times M13\text{-}N2 \qquad \text{(Eq. 4-12)}$$

Analogue rearrangement of equations (Eq. 1-5) and (Eq. 1-6) gives the relation:

$$M13\text{-}O3N2 = 2.695 + 0.669 \times PP04\text{-}O3N2 \qquad \text{(Eq. 4-13)}$$

$$PP04\text{-}O3N2 = -4.030 + 1.495 \times M13\text{-}O3N2 \qquad \text{(Eq. 4-14)}$$

Equations (Eq. 4-11) to (Eq. 4-14) have been used to fill missing PP04/M13 results of same method (N2 or O3N2) in Table 4-7. All black values are metallicities as found in the previous work; all blue values are converted values according the equations above. A conversion between N2 and O3N2 according Kewley and Ellison (2008) has not been applied for same reason as discussed in section 4.3.1.

The results in Table 4-7 are split in results of 9 Type Ib, 10 Type Ic and 27 Type IIP SNe for the N2 method, and 8 Type Ib, 4 Type Ic and 10 Type IIP SNe for the O3N2 method. In total (INT observations plus previous work) N2 metallicities of the environments of 23 Type Ib, 29 Type Ic and 60 Type IIP SNe are available; the numbers for the O3N2 method are 17 Type Ib, 22 Type Ic and 29 Type IIP.

Table 4-7: SN environment metallicities from previous work. PP04 are the calibrations by Pettini and Pagel (2004) and M13 are the calibrations by Marino et al. (2013). Black values are the measured values as published in the papers; blue values are converted values according to equations (Eq. 4-11) to (Eq. 4-14).

SN	SN type	PP04-N2 [12+log(O/H)]	M13-N2 [12+log(O/H)]	Source[1]	PP04-O3N2 [12+log(O/H)]	M13-O3N2 [12+log(O/H)]	Source[1]
1982R	Ib	8.65	8.54	Ku18	-	-	-
1983N	Ib	8.68	8.56	Ku18	-	-	-
1984L	Ib	8.31	8.26	Ku18	8.57	8.43	Ga16
1985F	Ib	8.43	8.37	An10	-	-	-
1988L	Ib	-	-	-	8.80	8.58	Ga16
1996N	Ib	8.54	8.45	Ku18	-	-	-
1997X	Ib	8.65	8.54	Ku18	8.68	8.50	An10
1999dn	Ib	-	-	-	8.32	8.26	Mo10
1999ec	Ib	8.53	8.44	Ku18	8.45	8.35	An10
2007uy	Ib	-	-	-	8.60	8.45	Mo10
2007Y	Ib	8.60	8.50	Le11	8.74	8.54	Le11
2009jf	Ib	8.55	8.46	Sa12	8.47	8.36	Sa12
1962L	Ic	8.36	8.31	An10	8.33	8.27	An10
1964L	Ic	8.59	8.50	An10	-	-	-
1983I	Ic	8.73	8.61	An10	-	-	-
1987M	Ic	8.65	8.54	An10	-	-	-
1991N	Ic	8.49	8.41	An10	8.44	8.34	An10
1994I	Ic	8.58	8.48	Ku18	-	-	-
1996aq	Ic	-	-	-	8.54	8.41	Mo10

SN	SN type	PP04-N2 [12+log(O/H)]	M13-N2 [12+log(O/H)]	Source[1]	PP04-O3N2 [12+log(O/H)]	M13-O3N2 [12+log(O/H)]	Source[1]
1997dq	Ic	8.60	8.50	Ku18	-	-	-
2001ef	Ic	8.84	8.70	An10	-	-	-
2003gf	Ic	8.01	8.02	Ku18	-	-	-
2005at	Ic	8.74	8.61	Ku18	-	-	-
2005az	Ic	-	-	-	8.66	8.49	Ga16
1983K	IIP	8.66	8.55	Ku18	-	-	-
1985G	IIP	8.65	8.54	Ku18	-	-	-
1985P	IIP	8.77	8.64	Ku18	-	-	-
1986L	IIP	8.52	8.44	An10	8.51	8.39	An10
1990E	IIP	8.57	8.48	An10	-	-	-
1990H	IIP	8.68	8.57	An10	-	-	-
1990K	IIP	8.63	8.53	An10	8.63	8.47	An10
1992ba	IIP	8.55	8.46	Ku18	8.66	8.49	An10
1999bg	IIP	-	-	-	8.45	8.35	Ga16
1999br	IIP	8.59	8.49	Ku18	-	-	-
1999eu	IIP	8.61	8.51	Ku18	-	-	-
1999gn	IIP	8.68	8.56	Ku18	-	-	-
2000cb	IIP	8.53	8.45	An10	8.70	8.52	An10
2001X	IIP	8.70	8.58	Ku18	-	-	-
2003B	IIP	8.66	8.55	Ku18	8.79	8.58	An10
2003hl	IIP	8.66	8.55	An10	8.87	8.63	An10
2003hn	IIP	8.46	8.39	An10	8.46	8.35	An10
2003ie	IIP	8.63	8.52	Ku18	-	-	-
2004am	IIP	8.79	8.65	Ku18	-	-	-
2006my	IIP	8.74	8.61	Ku18	-	-	-
2006ov	IIP	8.66	8.55	An10	8.50	8.38	An10
2007oc	IIP	8.56	8.48	Ku18	-	-	-
2009ib	IIP	8.53	8.44	Ku18	-	-	-
2009md	IIP	8.61	8.51	Ku18	-	-	-
2009N	IIP	8.45	8.38	Ku18	-	-	-
2010F	IIP	8.64	8.53	Ku18	-	-	-
2011cj	IIP	-	-	-	8.53	8.40	Ga16
2011gv	IIP	8.64	8.53	Ku18	-	-	-
2012ho	IIP	8.53	8.44	Ku18	-	-	-

1) References: An10 = Anderson et al. 2010; Ga16 = Galbany et al. 2016; Ku18=Kuncarayakti et al., 2018); Le11 = Leloudas et al. 2011; Mo10 = Modjaz et al. 2011; Sa12 = Sanders et al. 2012.

Table 4-8 lists the mean and standard deviations of the metallicities for the different SN types and for the total extended sample. Again, the differences in the mean of the metallicities are small for all cases. There is still a remarkable difference in the standard deviations between Type Ib and the two other types for the O3N2 method. This is no longer true for the N2 method.

Table 4-8: Number of targets N, mean value and standard deviation σ of metallicities for the three SN types derived from the extended sample, INT plus previous work, results.

SN type	N(N2)	PP04-N2 [12+log(O/H)]		M13-N2 [12+log(O/H)]		N(O3N2)	PP04-O3N2 [12+log(O/H)]		M13-O3N2 [12+log(O/H)]	
		mean	σ	mean	σ		mean	σ	mean	σ
Ib	23	8.61	0.14	8.51	0.11	17	8.63	0.14	8.47	0.09
Ic	29	8.58	0.19	8.48	0.16	22	8.63	0.23	8.47	0.16
IIP	60	8.62	0.14	8.52	0.11	29	8.58	0.20	8.43	0.13
all	112	8.61	0.15	8.51	0.12	68	8.61	0.20	8.45	0.13

Figure 4-8 to Figure 4-11 show the CDFs of the results of the four calibrations for the extended sample. There seems no tendency in the CDFs estimated by N2 calibrations (Figure 4-8/Figure 4-9): all CDFs look very similar with a slight tendency to lower metallicities for Type Ic. For the O3N2 calibrations, the tendencies of the CDFs of the INT sample only (Figure 4-4/Figure 4-5) are kept: the narrower Type Ib distribution and the tendency to higher metallicities for Type Ic compared with Type IIP.

Figure 4-8: CDFs of the extended sample. SN environment metallicities measured with the N2 calibration of Pettini and Pagel (2004). Binning width for CDF calculation: 0.025 dex.
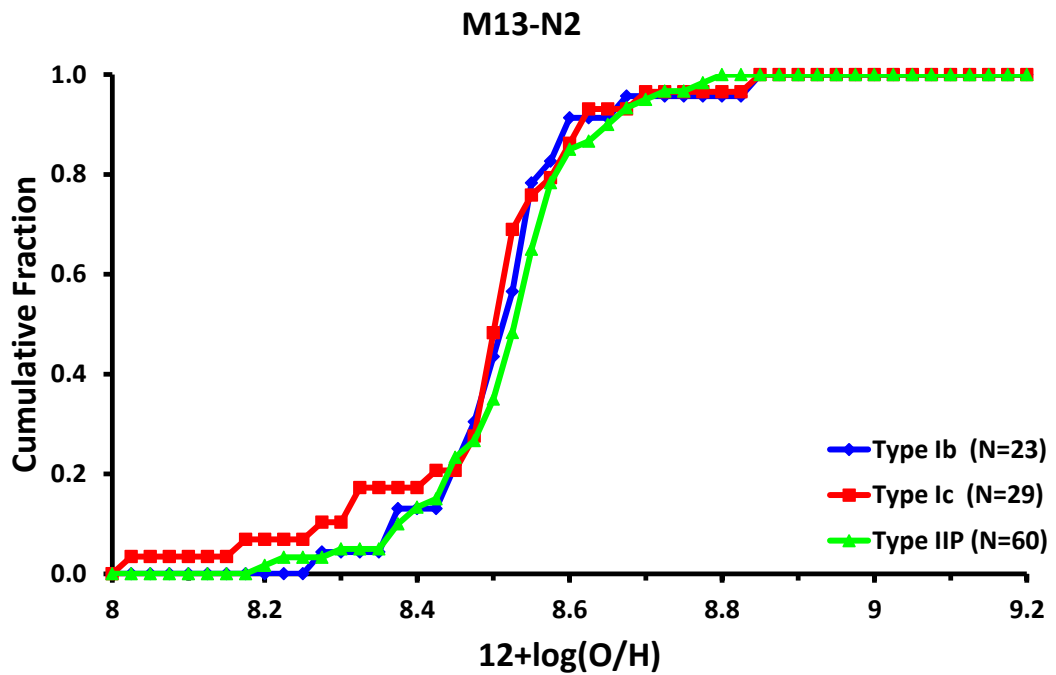
Figure 4-9: CDFs of the extended sample. SN environment metallicities measured with the N2 calibration of Marino et al. (2013). Binning width for CDF calculation: 0.025 dex.
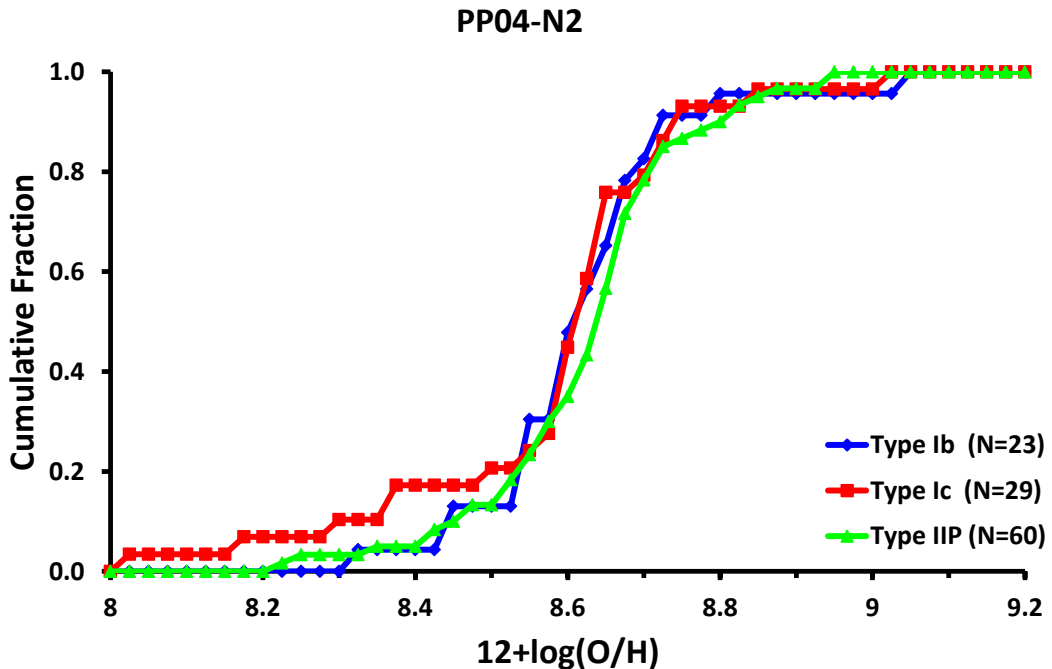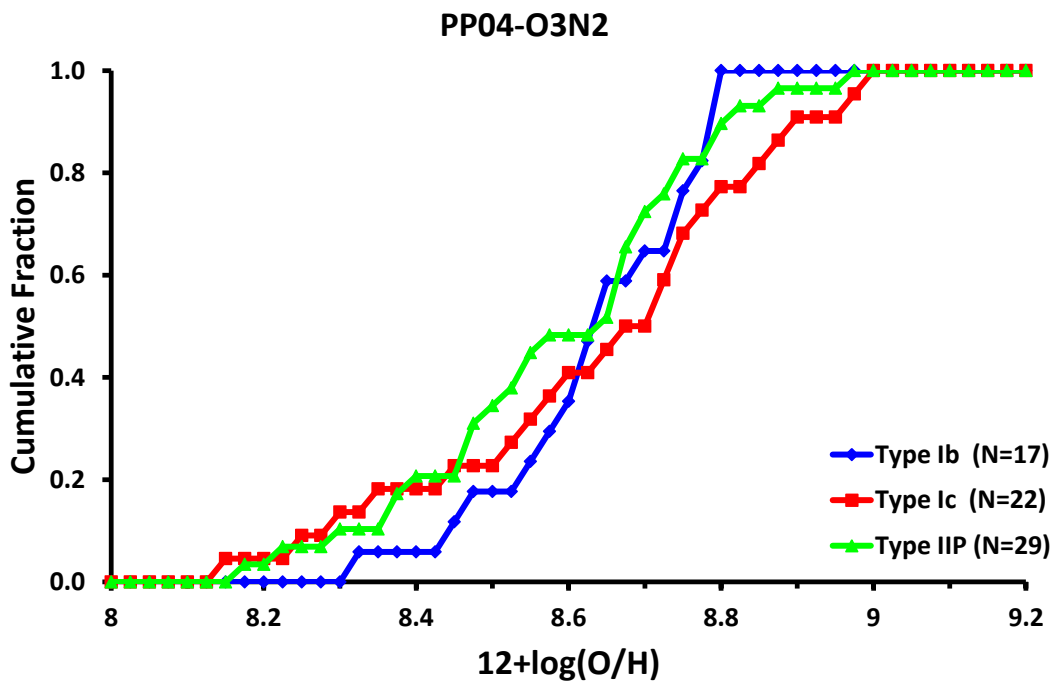

Figure 4-10: CDFs of the extended sample. SN environment metallicities measured with the O3N2 calibration of Pettini and Pagel (2004). Binning width for CDF calculation: 0.025 dex.
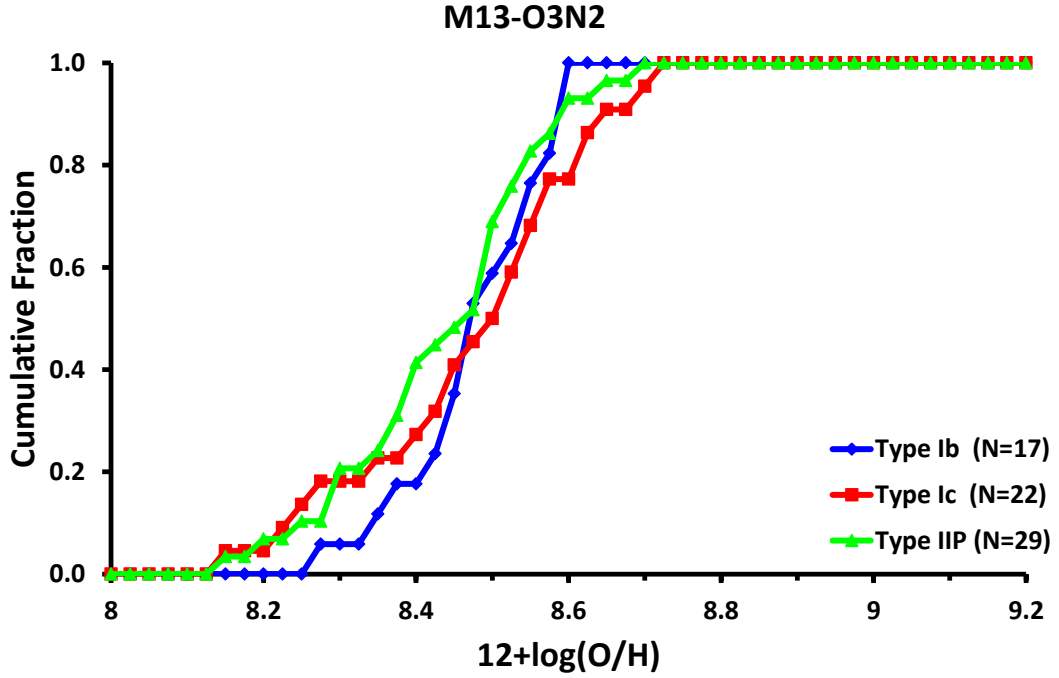
Figure 4-11: CDFs of the extended sample. SN environment metallicities measured with the O3N2 calibration of Marino et al. (2013). Binning width for CDF calculation: 0.025 dex.

4.4.3 Kolmogoroff-Smirnow Test

In order to check a statistically significant difference between the samples of the different SN-types, the two-sample KS-test and the two-sample AD-test have been applied to the extended sample also.

Table 4-9 lists the KS-test p-values results of the extended sample combinations Ib-Ic, Ib-IIP and Ic-IIP for all four metallicity calibrations. Again, the p-values are all significantly greater than a significance level of 5%. Consequently, there is no statistical significance that the metallicities of the environments of the different SN-types are different.

Table 4-9: P-values of the two-sample KS-test for the extended sample calculated by the R-function 'ks_test' (number of permutations: two millions). All p-values exceed the chosen significance level of 5% and the null hypothesis cannot be rejected.

SN types	PP04-N2 p-value	M13-N2 p-value	PP04-O3N2 p-value	M13-O3N2 p-value
Ib-Ic	0.736	0.876	0.582	0.532
Ib-IIP	0.697	0.691	0.301	0.261
Ic-IIP	0.186	0.248	0.455	0.620

4.4.4 Anderson-Darling Test

Table 4-10 lists the estimated p-values of the two-sample AD-tests for all extended sample combinations Ib-Ic, Ib-IIP and Ic-IIP and all four metallicity calibrations. Again, the calculated p-values are all definitively greater than 0.05 for a significance level of 5%. Thus the null hypothesis of same parent population must not be rejected. There is no statistical significance that the metallicities of the environments of the different SN-types are different. The results of two-sample KS-test and two-sample AD-test are consistent.

Table 4-10: P-values of the two-sample AD-test for the extended sample calculated by the R-function 'ad_test' (number of permutations: two millions). All p-values exceed the chosen significance level of 5% and the null hypothesis cannot be rejected.

SN types	PP04-N2 p-value	M13-N2 p-value	PP04-O3N2 p-value	M13-O3N2 p-value
Ib-Ic	0.835	0.833	0.415	0.431
Ib-IIP	0.888	0.885	0.449	0.370
Ic-IIP	0.487	0.489	0.441	0.501

Chapter 5

Discussion

This chapter draws together and discusses the results obtained in the previous chapter. After an introductory summary of the results, the reliability of the different strong emission line calibrations is debated, followed by a discussion on the sensitivity of the statistical tests. Potential observational biases of the sample are the objective of the fourth section and the discussion of constraints for SNe progenitors based on the obtained results completes the chapter.

5.1 Summary of Results

5.1.1 Summary of O3N2 calibration results

Figure 5-1 gives an overview of the results of the O3N2 calibration metallicities. Three features are clearly visible in all CDFs:

- The distribution of Type Ib is narrower than the distribution of the other two SNe types.

- Type Ic SNe environments have the same lower metallicity limit as Type IIP.

- The CDFs of Type Ic and Type IIP start at about same metallicity but begin to diverge at about 8.3 dex with trend to higher metallicity for Type Ic SNe.

Figure 5-1: CDFs of the metallicities based on the O3N2 calibrations. Left column shows the CDFs for the INT sample, the right one for the extended sample. Upper panel shows the PP04 based results, the M13 based results are in the lower panel. All four CDFs exhibit the features discussed in the text more or less distinctive.

These features are reflected in the characteristic statistical data of the CDFs (Table 4-2 and Table 4-8): the mean values for Type Ib and Ic are higher than the mean values of Type IIP by about 0.07 to 0.1 dex for the INT sample (0.05 dex for the extended sample). The standard deviations of Type Ib are about 0.12 (0.07) dex less than the standard deviations of Type Ic and Type IIP. Regardless of these differences, the KS-test and the AD-test revealed no statistical significance to reject the null hypothesis that all samples are drawn from same parent population.

5.1.2 Summary of N2 calibration results

The features clearly visible in the O3N2 calibration results disappear in the N2 results for both the INT as well as for the extended sample almost completely (Figure 5-2). Just the low metallicity limit of Type Ic SNe remains. The differences in the characteristic data of the CDFs are also significantly lower: the mean values differ less than about 0.03 dex as well as the standard deviations (0.03 - 0.05 dex). With these data, it is not surprising that the statistical tests do not reject the null hypothesis.
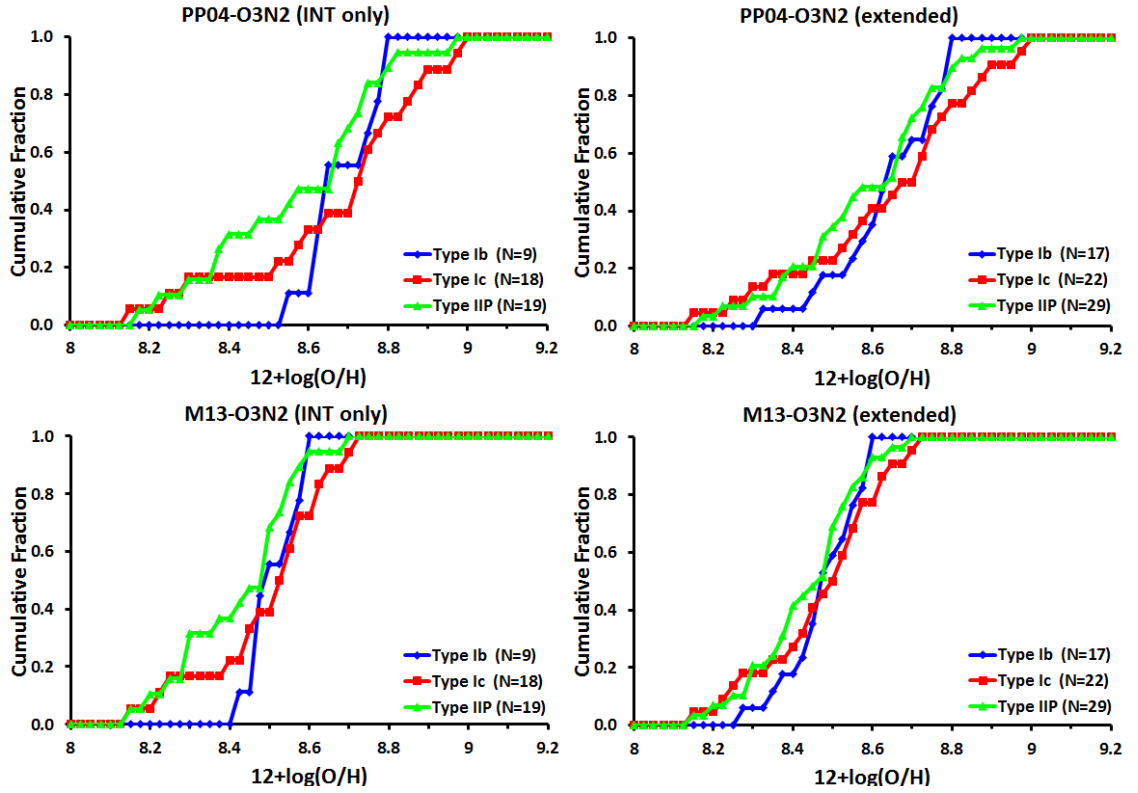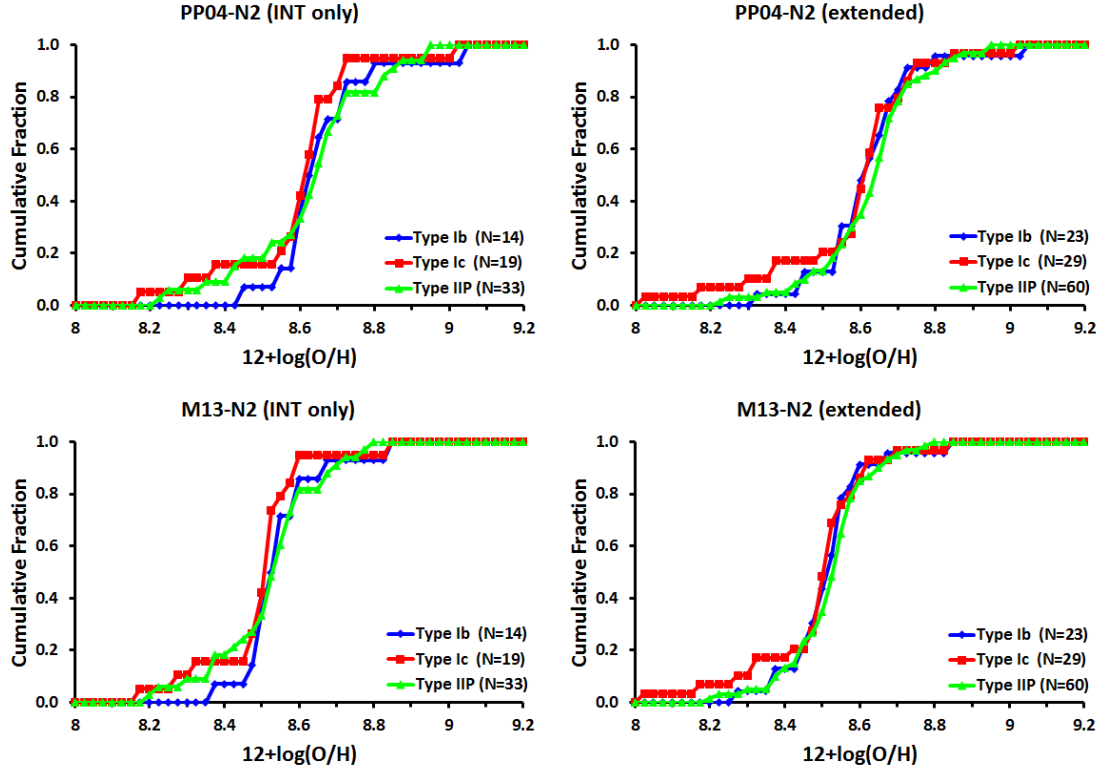
Figure 5-2: CDFs of the metallicities based on the N2 calibrations. Left column shows the CDFs for the INT sample, the right one for the extended sample. Upper panel shows the PP04 based results, the M13 based results are in the lower panel. The features clearly visible in the CDFs of the O3N2 calibrations have disappeared almost completely. Just the low metallicity limit of Type Ic has remained.

5.2 Reliability of Strong Emission Line Results

The significant qualitative differences between O3N2 and N2 calibration results described above need discussion. The section is structured in checks of calibration validity limits, comparison of results of targets with multiple observations, discussion of statistical correlations, observational issues and physical differences between the two calibration methods.

Table 5-1: Validity limits of PP04 and M13 calibrations as given in Pettini and Pagel (2004) and Marino et al. (2013), respectively. $N2 = \log([NII]\lambda6583/H\alpha)$ and $O3N2 = \log\{([OIII]\lambda5007/H\beta)/([NII]\lambda6583/H\alpha)\}$.

calibration	validity limits	$12 + \log(O/H)$ validity limits
PP04-N2:	$-2.5 < N2 < -0.3$	$7.475 < 12 + \log(O/H) < 8.729$
M13-N2:	$-1.6 < N2 < -0.2$	$8.004 < 12 + \log(O/H) < 8.651$
PP04-O3N2:	$-1.0 < O3N2 < 1.9$	$8.122 < 12 + \log(O/H) < 9.050$
M13-O3N2:	$-1.1 < O3N2 < 1.7$	$8.169 < 12 + \log(O/H) < 8.768$

5.2.1 Check of Validity Range

The N2 as well as the O3N2 calibration are derived from empirical data resulting in validity limits of the calibrations. The check of the limits (Table 5-1) revealed that all targets with O3N2 calibration results (in total 46, $-0.82 <$ O3N2 < 1.84) of the INT sample meet the limits of PP04-O3N2. All but two targets meet the limits of M13-O3N2 with a deviation of less than 0.15 for the two failed targets at the upper validity limit. From the 66 INT targets with N2 calibration results ($-1.27 <$ N2 < 0.23), in total 9 targets exceed the upper limit for PP04-N2 calibration, 4 of them significantly (>0.15); the numbers for M13-N2 are 8 and 4, respectively. The four targets with a significant deviation are SN1999em, SN2000ds, SN2012bc and SN2014bc. The number of these outliers (6% of total sample) is too small to explain the differences between the N2 and O3N2 results because the CDFs do not change significantly if the outliers are removed from sample.

5.2.2 Targets with Multiple Observations

Confidence in the results of the calibrations may be improved by comparing the results of targets with multiple observations. There are 10 targets observed twice and three targets observed three times at the INT during the project. The difference of the results for a target with multiple observations is in worst case about 0.06 dex (independent of calibration method), well within the uncertainty ranges (see Table 4-1). The only exception is the Ca-rich Type Ib SN2000ds with a difference of 0.3 dex likely caused by the low SNR of the observations or by an intrinsic physical difference of Ca-rich Type Ib SNe compared to normal Type Ib SNe. The scatter plot in Figure 5-3 shows the small deviations from the 1:1 line.

Multiple observations are available from previous work also. In total 32 INT targets were previously observed by other instruments (see Table 5-2 and Figure 5-4). The metallicities of just 5 of them are outside the uncertainty range of the INT observations. This is a remarkably good result taking into account the different instrumentations and the different data reduction processes.
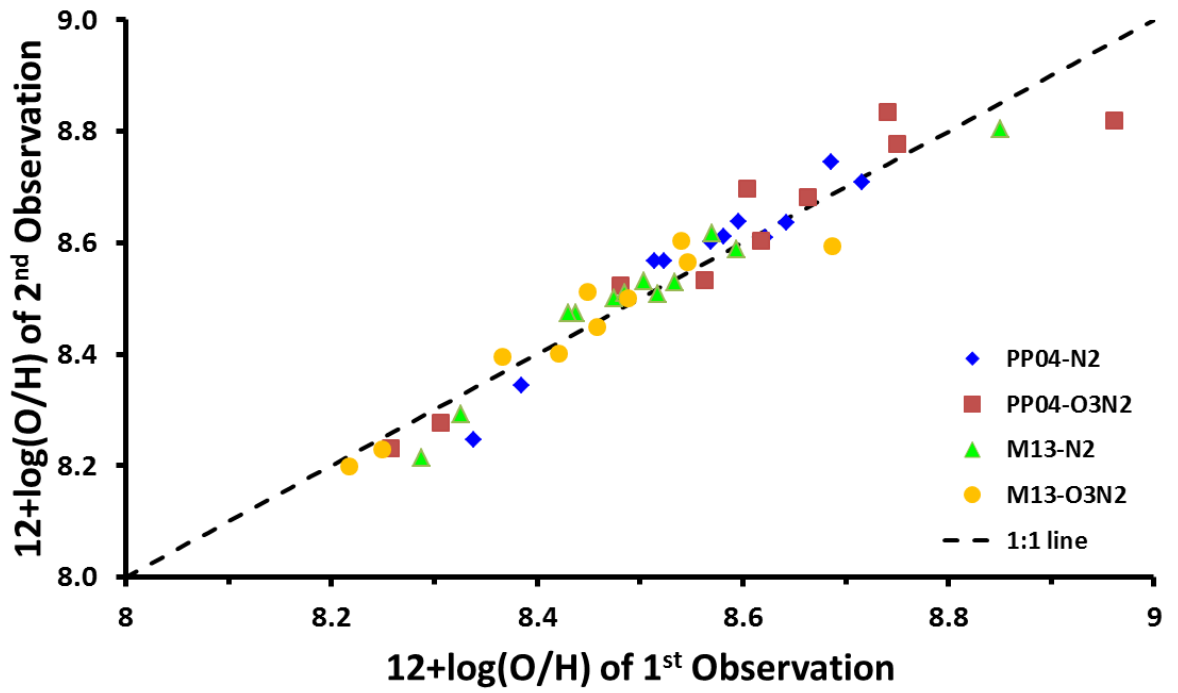
Figure 5-3: Scatterplot of multiple observed INT targets. The figure shows metallicities of 1st observations vs. 2nd observations. For targets with three observations, the worst case difference has been taken.
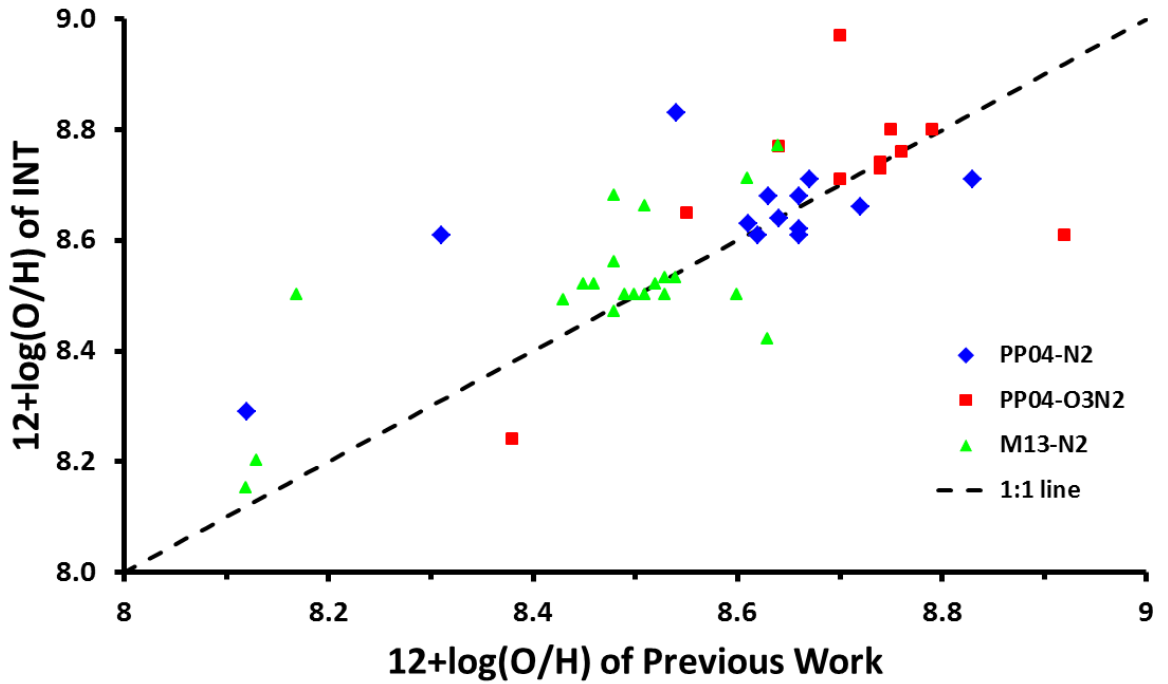

Figure 5-4: Scatterplot of targets multiple observed by INT and in previous work. The figure shows the INT results vs. the results of previous work. For targets with more than two results, the worst case difference has been taken.

Table 5-2: Overview of metallicity results of targets multiple observed at INT and in previous work. The table is structured in three blocks for PP04-N2, M13-N2 and PP04-O3N2 (no M13-O3N2 results in previous work). Each block consists of the INT results of this work, the results of previous work and the sources where the value has been taken from. The red marked values are previous results outside the uncertainty range of the INT results.

target	type	INT	previous[1]		INT	previous[1]		INT	previous[1]	
		12+log(O/H) of PP04-N2			12+Log(O/H) of M13-N2			12+Log(O/H) of PP04-O3N2		
2001B	Ib	8.61±0.18	8.66	An10	-	-	-	8.65±0.14	8.55	An10
2002ji	Ib	8.64±0.18	8.64	An10	8.53±0.16	8.54	Ga16	8.74±0.14	8.74	An19
2004ao	Ib	-	-	-	8.49±0.17	8.43	Ku18	-	-	-
2004gq	Ib	8.66±0.18	8.72	An10	-	-	-	8.80±0.14	8.75	An10
2005V	Ib/c	8.71±0.18	8.83	An10	-	-	-	8.76±0.14	8.76	An10
2007C	Ib	8.71±0.18	8.67	Le11	-	-	-	8.80±0.14	8.79	Le11
2008D	Ib	-	-	-	-	-	-	8.61±0.15	**8.92**	Mo11
2012au	Ib	-	-	-	8.50±0.16	8.51	Ku18	-	-	-
2012P	Ib/c	-	-	-	8.50±0.16	8.53	Ku18	-	-	-
2000ew	Ic	-	-	-	8.50±0.16	8.49	Ku18	-	-	-
2002jz	Ic	8.29±0.20	8.12	An10	-	-	-	8.24±0.15	8.38	An10
2004bm	Ic	8.68±0.18	8.63	An10	-	-	-	8.97±0.14	**8.70**	An10
2004gn	Ic	8.62±0.18	8.66	An10	-	-	-	-	-	-
2004gt	Ic	-	-	-	-	-	-	8.71±0.14	8.70	Mo11
2005kl	Ic	8.61±0.18	8.62	An10	-	-	-	8.73±0.14	8.74	An10
2007gr	Ic	-	-	-	8.50±0.16	8.54 Ga16 8.60 Ku18		8.77±0.14	8.64	Mo11
2009em	Ic	8.63±0.18	8.61	An10	-	-	-	-	-	-
2011jm	Ic	-	-	-	8.15±0.16	8.12	Ku18	-	-	-
2012fh	Ic	-	-	-	8.47±0.16	8.48	Ku18	-	-	-
1998dl	IIP	-	-	-	8.52±0.16	8.46	Ku18	-	-	-
1999em	IIP	-	-	-	8.77±0.16	8.64	Ga16	-	-	-
1999gi	IIP	-	-	-	8.42±0.16	**8.63** Ga16 8.47 Ku18		-	-	-
2001fv	IIP	-	-	-	8.71±0.16	8.61	Ku18	-	-	-
2002hh	IIP	-	-	-	8.52±0.16	8.52	Ku18	-	-	-
2003gd	IIP	8.83±0.19	**8.54**	An10	8.68±0.17	**8.48**	Ga16	-	-	-
2004dg	IIP	-	-	-	8.53±0.16	8.53	Ku18	-	-	-
2004dj	IIP	8.61±0.19	**8.31**	An10	8.50±0.16	**8.17**	Ku18	-	-	-
2005ay	IIP	8.68±0.19	8.66	An10	8.56±0.17	8.48	Ku18	-	-	-
2007aa	IIP	-	-	-	8.50±0.17	8.50	Ku18	-	-	-
2012A	IIP	-	-	-	8.20±0.16	8.13	Ku18	-	-	-
2012ec	IIP	-	-	-	8.52±0.16	8.45	Ku18	-	-	-
2013ej	IIP	-	-	-	8.66±0.17	8.51	Ga16	-	-	-

1) References: An10 = Anderson et al. 2010; Ga16 = Galbany et al. 2016; Ku18=Kuncarayakti et al., 2018); Le11 = Leloudas et al. 2011; Mo10 = Modjaz et al. 2011.

5.2.3 Correlation between N2 and O3N2 Calibration

Scatter plots are a means to reveal underlying relations between two samples e.g. in the case of a linear relation the scatter plot should show a linear correlation. It can also reveal areas with large and small scatter range.

Figure 5-5 and Figure 5-6 show the scatter plots of O3N2 vs. N2 for PP04 and M13 calibration of the INT observations for which both calibration results are available. For both calibrations, the scatter range increases with increasing metallicity but the correlation of the overall sample is still almost linear in both cases as shown by the linear trend lines (green) having regression coefficients >76%. Trend lines with higher polynomial order do not improve the regression coefficients.

Figure 5-5 also show the conversion relation (red line) between PP04-N2 and PP04-O3N2 as given by Kewley and Ellison (2008) as the quadratic polynomial

$$y = -0.09368x^2 + 2.74353x - 8.0069 \qquad \text{(Eq. 5-1)}$$

where y is PP04-O3N2 and x is PP04-N2. The relation has a slightly different slope compared with the trend line but it is also mostly linear.

An equivalent relation for M13-N2 and M13-O3N2 can be derived from (Eq. 5-1) using (Eq. 4-11) and (Eq. 4-13):

$$y = -0.09543x^2 + 2.5568x - 6.3482 \qquad \text{(Eq. 5-2)}$$

where y is M13-O3N2 and x is M13-N2. The equation above is shown in Figure 5-6 as red line. Again, the relation has a slightly different slope compared with the trend line but it is mostly linear also.

The most interesting result of the scatter plots is the increasing scatter with increasing metallicity. This may be caused by the relatively small number of targets in the lower metallicity range and/or by the limitations of the N2 calibration at higher metallicities (see section 5.2.6).

PP04 Scatterplot (INT only)

y = 1.358x - 3.0049
R² = 0.7637

- ◆ O3N2 vs. N2 (PP04)
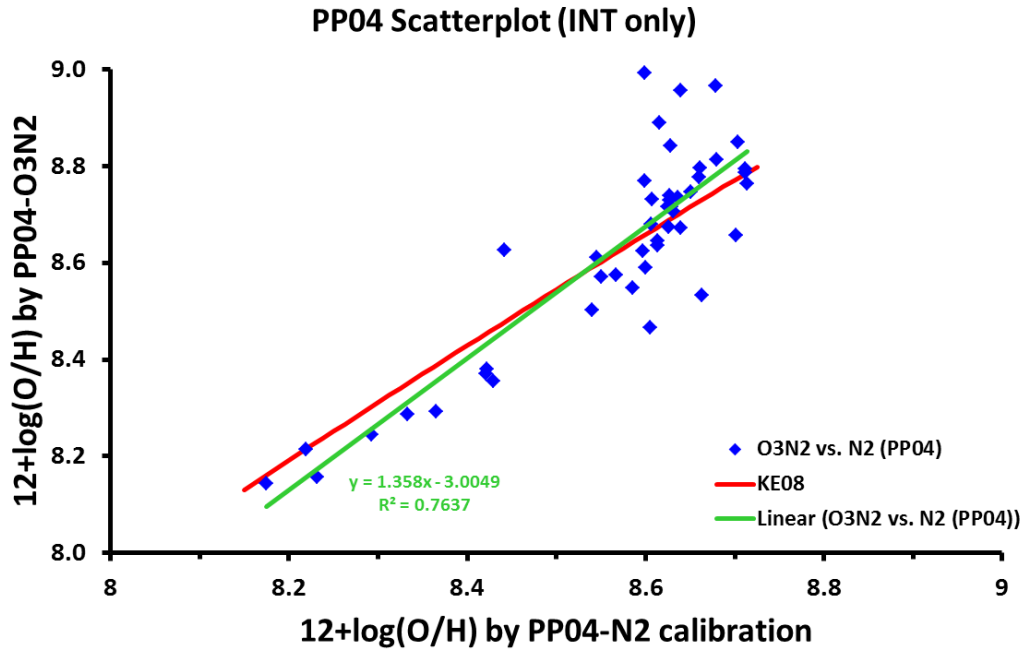- — KE08
- — Linear (O3N2 vs. N2 (PP04))

Figure 5-5: Scatter plot of PP04-O3N2 results vs. PP04-N2. The blue diamonds mark the INT targets with both N2 and O3N2 results available. Green line is the linear trend line calculated from the sample points. The red line is the relation between PP04-N2 and PP03-O3N2 as published by Kewley and Ellison (2008). There is an apparent pileup of points for x-axis values > 8.6 dex, where the scatter significantly increases. Despite the weak correlation at high metallicities, the regression coefficient R^2 of about 76% of the linear trend line indicates a linear correlation between the overall samples.

M13 Scatterplot (INT only)

y = 1.1206x - 1.0294
R² = 0.764

- ◆ O3N2 vs. N2 (M13)
- — KE08 transformed
- — Linear (O3N2 vs. N2 (M13))

Figure 5-6: Scatter plot of M13-O3N2 results vs. M13-N2. The blue diamonds mark the INT targets with both N2 and O3N2 results available. Green line is the linear trend line calculated from the sample points. The red line is the transformed (Eq. 5-2) relation by Kewley and Ellison (2008) for M13-N2 and M13-O3N2. Again, there is an apparent pileup of points for x-axis values > 8.5 dex, where the scatter significantly increases. Despite the weak correlation at high metallicities, the regression coefficient R^2 of about 76% of the linear trend line indicates a linear correlation between the overall samples.
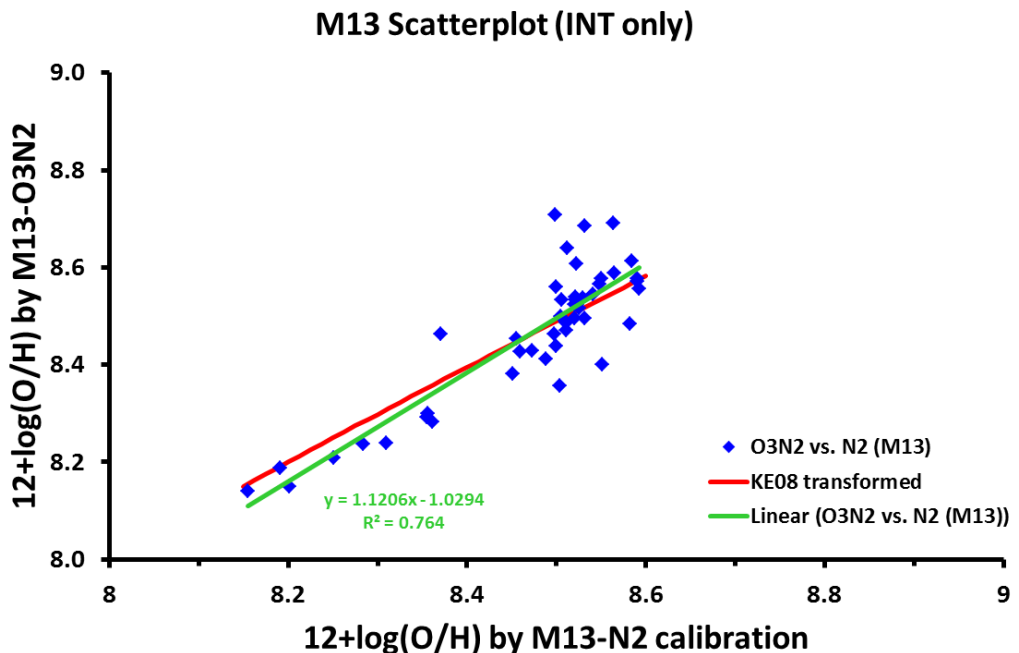
96

5.2.4 Observational Issues

From an observational point of view there are at least two points that can cause differences in the behaviour of the two calibration methods: the close proximity of Hα and the doublet [NII]λλ6548,6583 and the worse SNR for Hβ compared with Hα.

The close proximity of Hα and [NII] doublet ($\Delta\lambda_0 = 15$ Å and 20 Å, respectively) can cause interference between the two lines by blending in the case of broad lines (Figure 5-7). This is not the case for all INT observations but SN1996D as checked by visual inspection. Some interference by the emission line wings cannot be excluded definitively but it should be negligibly small.

The second point is the always weaker Hβ line compared with the Hα line. Constant noise level assumed, the SNR for Hβ is always worse as the Hα SNR. But for all INT observations where Hβ is present, the SNR of the Hβ is good enough for line fitting and SNR issues are more often caused by the [NII] and/or [OIII] lines. It is unlikely that SNR issues cause the differences between O3N2 and N2 method.
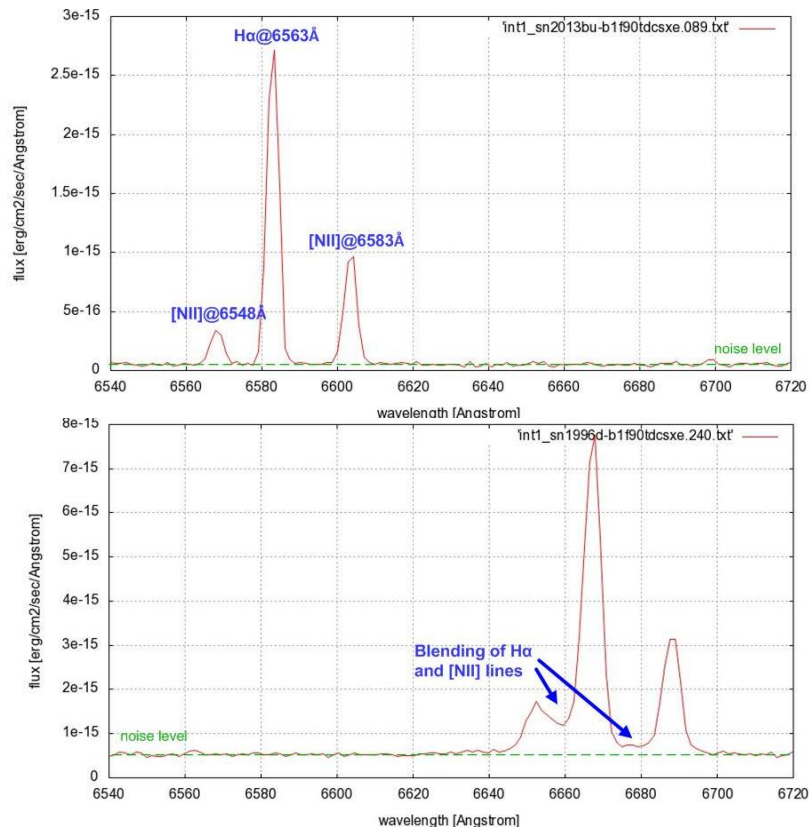

Figure 5-7: Example (SN2013bu) of well separated Hα and [NII] emission lines (top). Line broadening, e.g. by high velocity dispersion, can cause blending of the close lines (bottom, example SN1996D) that results in flux estimation errors. Visual check of all INT observations of all targets in Table 4-1 has proven blending as not significant.

5.2.5 Stellar Contaminations

A third observational issue is much more severe: the contamination of the HII region spectrum by stellar radiation by both stars within the HII region and/or stars in the line of sight. This contamination especially impacts the hydrogen lines by an underlying absorption impacting the true emission line intensities.

The stellar absorption impacts the hydrogen emission lines differently depending on the age of the underlying stellar population (e.g. Leitherer 2005, Figure 5-9). The underlying absorption also depends on the temperature and hence the mass of the stars. The predominant contribution comes from the A stars. The ratio of the Hα absorption line to the Hβ absorption line decreases if the stars get more massive (Figure 5-8; see also Carroll and Ostlie 2006, chapter 8). Thus, in young stellar populations, the stellar contamination impacts the Hβ emission line more than the Hα emission line and the ratio of these two lines is wrong if the contamination is not taken into account. Additionally, the [NII] and [OIII] lines are usually not affected by stellar contamination at all.
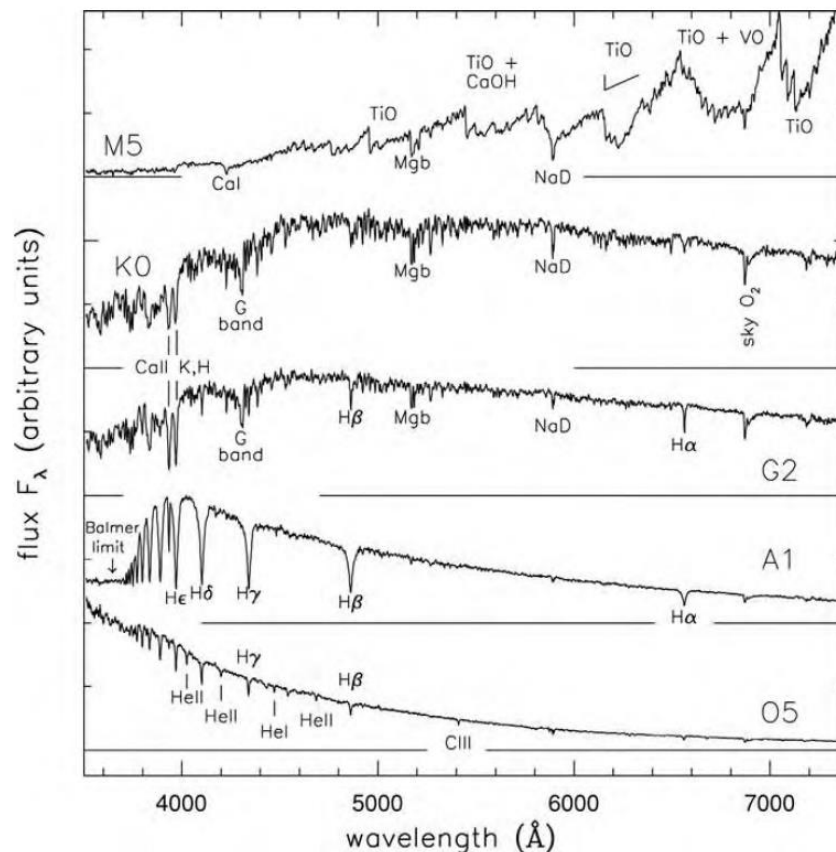

Figure 5-8: Example for different stellar spectra depending on the spectral class of main-sequence stars. The ratio of Hα absorption to Hβ absorption decreases with increasing effective temperature of the stars. The underlying stellar absorption comes predominantly from A stars (image: Sparke and Gallagher 2007).
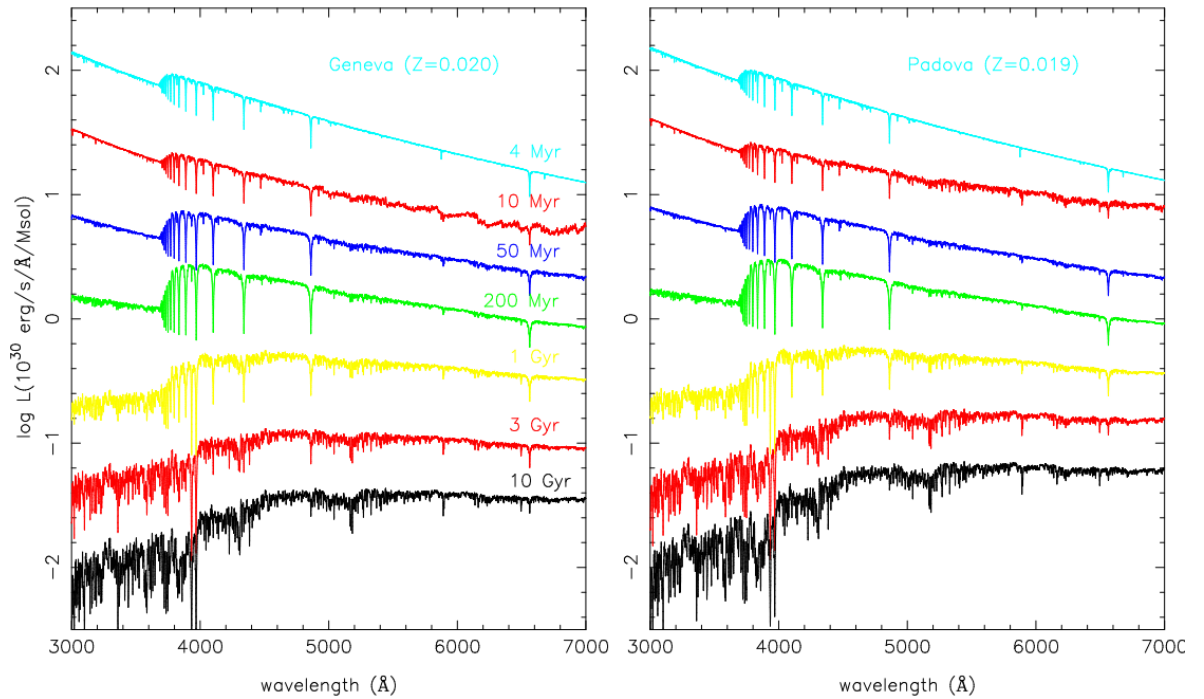
Figure 5-9: Spectral evolution of a simple stellar population with solar composition. Left panel shows the evolution from 4 Myr to 10 Gyr as predicted by the Geneva code (Schaller et al. 1992), the right one the prediction by the Padova code (Girardi et al. 2000) (image: Leitherer 2005).

The workaround to remove stellar contamination by DIPSO described in section 3.2.4 works well as long as the contamination is broader than the emission line. If the stellar absorption has the same or smaller width as the emission line, then the workaround is not applicable. The tests with PPXF (see section 3.2.4) reveal stellar contamination for most targets and generally the Hβ line is stronger affected (example see Figure 5-10).

The inferred metallicities by DIPSO and by PPXF were consistent and agreed well despite the fact that there were large differences of the line fluxes of Hβ and [OIII] (see section 3.2.4). Unfortunately, the plausibility checks of the PPXF results failed. E.g. the mean value of the Balmer decrement after de-reddening of the PPXF emission line fluxes was 2.27 ± 0.43 (DIPSO result: 2.78 ± 0.20) significantly less than the theoretical Case B value of 2.86 (see section 3.2.3). Also, there were unreasonable large radial velocity differences between stellar and gas component estimated by PPXF for some targets.

Modified PPXF evaluations with different stellar templates (see section 3.2.4) and changed call parameters did not help to remove the implausible results. Because the stellar contamination seems to be essential for the application of the strong emission

line method, deeper investigations of PPXF (or similar tools) are required to remove the inconsistencies. But this is beyond the scope of this work.
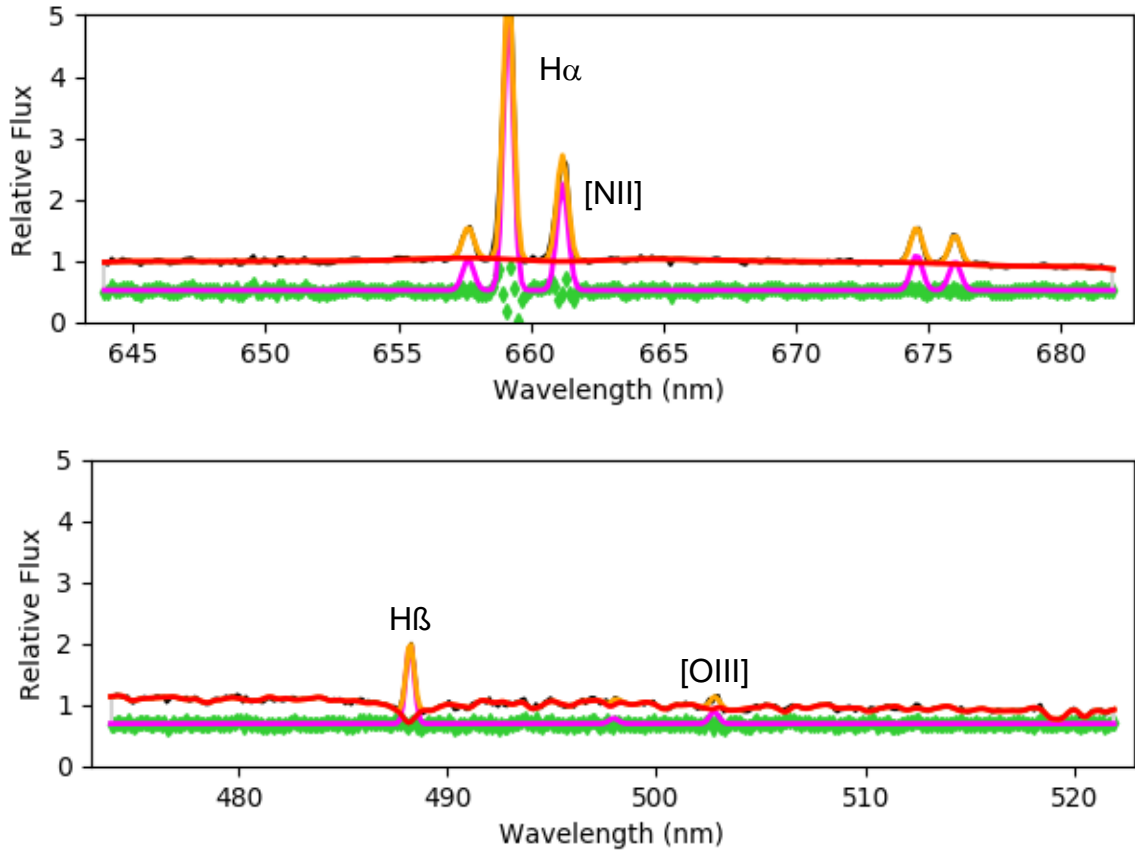

Figure 5-10: Example of a PPXF fit (target SN2004bm). The black line (hard to see because of the good fit) is the initial spectrum, the red line is the PPXF fit to the stellar component. The orange line is the fit to the emission lines. The green line shows the fit residuals and the magenta line is the gas-only fit. The upper panel shows the Hα region where no absorption is visible by the stellar component (red line). The lower panel shows the Hβ region with a clearly visible stellar absorption component impacting the Hβ emission line flux.

5.2.6 Physical Differences between O3N2 and N2 Calibration

The differences between the N2 and the O3N2 results may have a physical background. As mentioned by e.g. Pettini and Pagel (2004) and Marino et al. (2013), the [NII] line saturates for metallicities greater than solar metallicity (12 + log(O/H) = 8.59, Asplund et al. 2009) while the [OIII] line does not. Consequently, the N2 results should be unreliable for high metallicities as it relies just on [NII].

This larger uncertainty of the N2 calibration at high metallicities is consistent with the larger scatter at higher metallicities in the scatter plots of section 5.2.3. The N2 calibration seems to be challenged for high metallicity applications (see Figures 5-5/5-6).

5.3 Sensitivity of Statistical Tests

The statistical tests in sections 4.3.2/4.3.3 and 4.4.3/4.4.4 did not reject the null hypothesis that the samples are drawn from same parent population. This result is surprising especially for the O3N2 results of Type Ib compared with Types Ic/IIP with the obviously narrower Type Ib distribution.

The statistical tests so far do not take into account uncertainties of the samples. The simplest test of the statistical test sensitivity is to look at changes of the test results depending on variations of the sample mean value in the interval of its uncertainty. The standard error σ_m of the mean value of a sample is given by (e.g. Lane et al. 2019):

$$\sigma_m = \frac{\sigma}{\sqrt{N}} \qquad \text{(Eq. 5-3)}$$

where σ is the standard deviation of the sample and N is the sample size. The typical values of the standard errors of the samples are about 0.03 - 0.04 dex (see Table 5-3 and Table 5-4).

The sensitivity check of the statistical tests works as follows: The CDFs of the two samples under test are varied within the interval of the standard errors of their means. Because the samples are assumed to be statistically independent, the two means may vary by different amounts and in opposite directions. For simplification and to cover the worst case the variation of the means has been done by the same amount in opposite directions over the full standard error range.

Table 5-3: Standard errors of the mean values of the INT observations.

| Type | INT observations | | | |
	PP04-N2	M13-N2	PP04-O3N2	M13-O3N2
Ib	8.66 ± 0.04	8.54 ± 0.03	8.68 ± 0.03	8.50 ± 0.02
Ic	8.59 ± 0.04	8.49 ± 0.03	8.66 ± 0.06	8.49 ± 0.04
IIP	8.62 ± 0.03	8.52 ± 0.02	8.57 ± 0.05	8.42 ± 0.03
all	8.62 ± 0.02	8.52 ± 0.02	8.63 ± 0.03	8.46 ± 0.02

Table 5-4: Standard errors of the mean values of the extended sample.

| Type | extended sample | | | |
	PP04-N2	M13-N2	PP04-O3N2	M13-O3N2
Ib	8.61 ± 0.03	8.51 ± 0.02	8.63 ± 0.03	8.47 ± 0.02
Ic	8.58 ± 0.04	8.48 ± 0.03	8.63 ± 0.05	8.47 ± 0.03
IIP	8.62 ± 0.02	8.52 ± 0.01	8.58 ± 0.04	8.43 ± 0.02
all	8.61 ± 0.01	8.51 ± 0.01	8.61 ± 0.02	8.45 ± 0.02

Figure 5-11 and Figure 5-12 show as an example the results of the Type Ib samples with Type Ic samples. The x-axis is the variation of the mean value of the Type Ib sample (for better comparison the variation interval is ±0.04 dex in all cases). The mean value of the Type Ic sample changes the same amount but opposite direction, e.g. if the Type Ib mean changes by +0.01 dex, the Type Ic mean changes by −0.01 dex. The y-axis is the p-value as the result of the statistical test. In the case of p-value is below the chosen significance level (e.g. 5%), the null hypothesis (same parent population) must be rejected.

Figure 5-11: Sensitivity of KS-test (top) and AD-test (bottom) to variation of the sample mean values. The chart shows the result of the test with Type Ib and Type Ic and N2 calibration. Solid lines are results for the INT only sample, dashed lines for the extended sample. Red lines are PP04-N2 samples, blue lines are M13-N2 samples. The variation of the mean values is two-sided, that means if Type Ib mean varies by +Δmean dex, mean of Type Ic varies by −Δmean dex at same time (and vice versa).
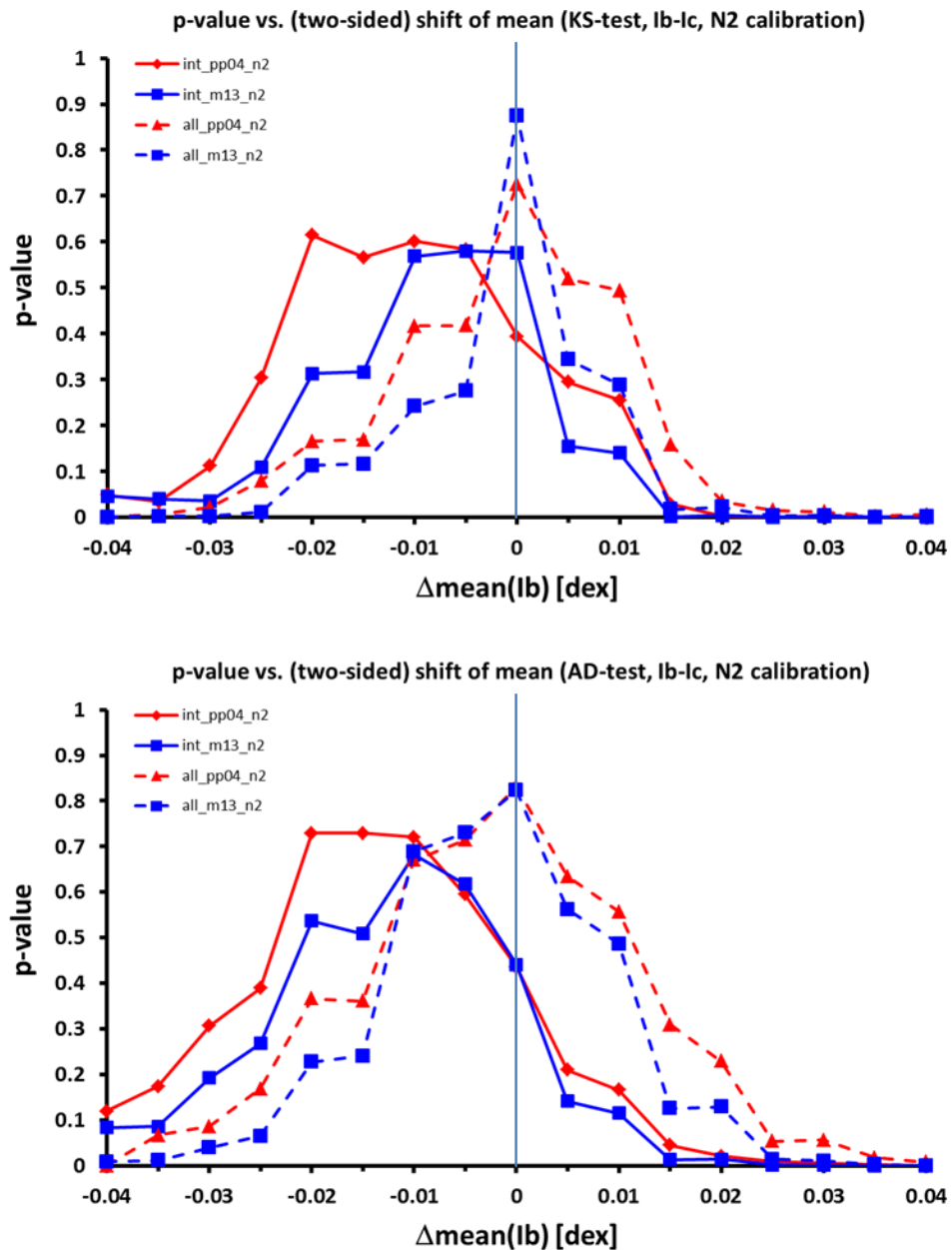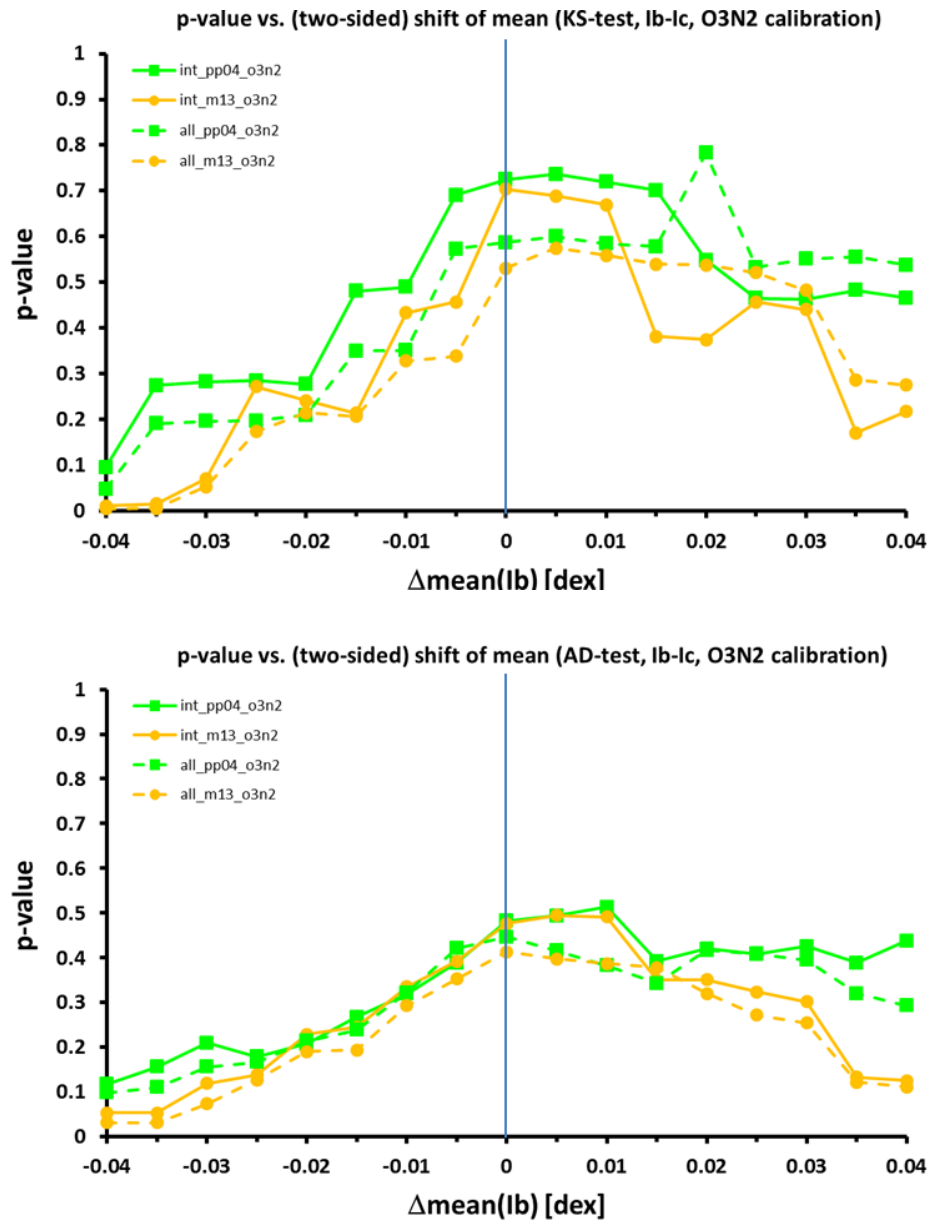
Figure 5-12: Sensitivity of KS-test (top) and AD-test (bottom) to variation of sample mean values. The chart shows the result of the test with Type Ib and Type Ic and O3N2 calibration. Solid lines are results for the INT only sample, dashed lines for the extended sample. Green lines are PP04-O3N2 samples, yellow lines are M13-O3N2 samples. The variation of the mean values is two-sided, that means if Type Ib mean varies by +Δmean dex, mean of Type Ic varies by −Δmean dex at same time (and vice versa).

The vertical lines in the figures at x=0 are the results as presented in sections 4.3 and 4.4 with large p-values leading to the conclusion that the samples have the same parent population. The variation of the means changes this picture: the p-values drop to a low level rapidly within the standard error interval of the means. This is most obvious for the KS-test and N2 calibration, but also clearly visible in the other three cases.

Consequently, taking into account the standard errors of the means, the statistical tests are not able to provide evidence regarding the parent population of the samples. If the errors of the means are allowed for the tests then it is possible that there are differ-

ences in the parent population between the SN types, but the test results are not conclusive because they provide significantly different p-values within the uncertainty interval of the means.

5.4 Observational Biases

The target sample of this work is strictly volume limited and an observational bias by specific host galaxy types or luminosities is not expected. The observed galaxies were defined by the target SNe and not by the project design of an untargeted survey potentially creating some bias (e.g. Galbany et al. 2014). There may be a bias to a specific galaxy type just by accident and indeed, as shown in Figure 5-13 and Figure 5-14, the Type Ib targets are more concentrated in higher luminosity galaxies than the other two types. But because the bulk of targets is concentrated in higher luminosity galaxies, the bias of Type Ib is unlikely the reason for the observed metallicity differences in the CDFs.
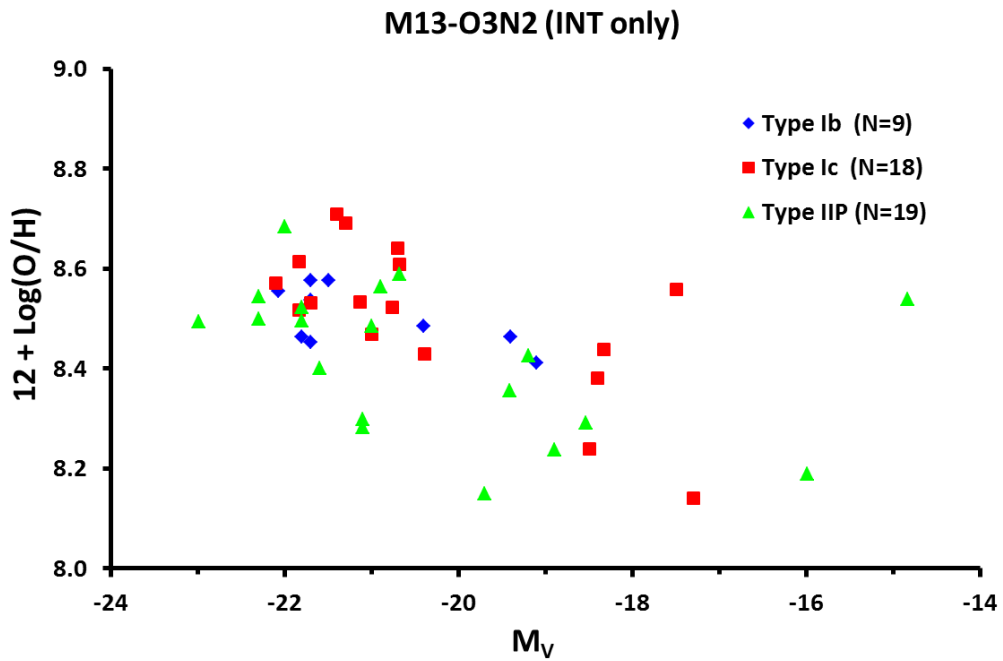

Figure 5-13: M13-O3N2 metallicities of the INT sample vs. absolute magnitude M_V of the host galaxies as proxy of the global galactic metallicity. Compared with Type IIP and Type Ic, the Type Ib targets of the INT sample are more concentrated in higher luminosity galaxies.
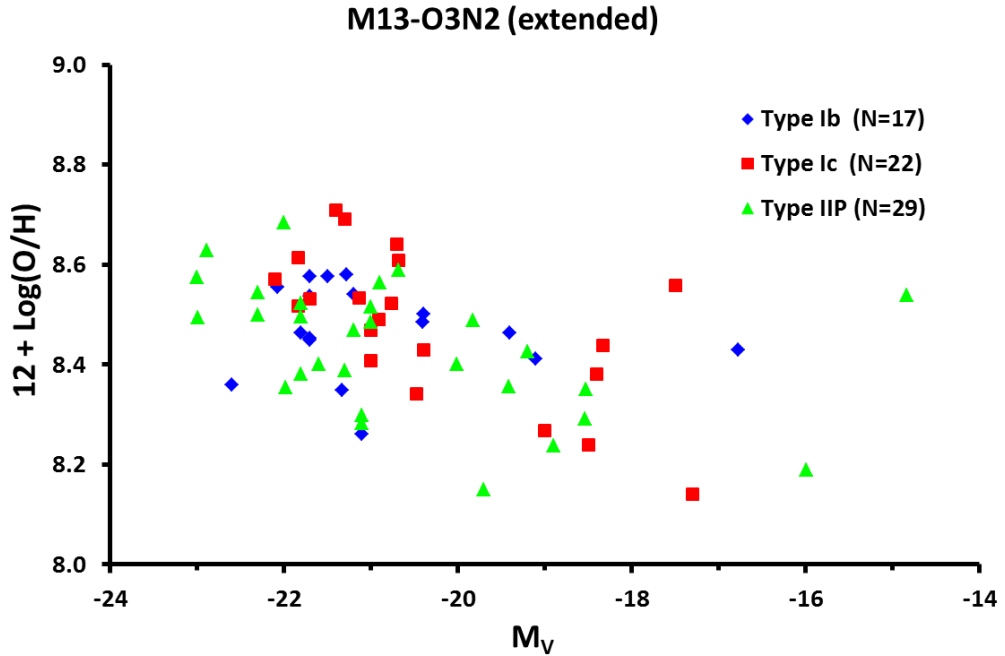
Figure 5-14: M13-O3N2 metallicities of the extended sample vs. absolute magnitude M_V of the host galaxies as proxy of the global galactic metallicity. Again, the Type Ib targets are more concentrated in higher luminosity galaxies.

5.5 Constraints for Type Ib,c Supernovae Progenitors

Is it possible to draw constraints for the progenitors of Type Ib,c SNe from the CDFs of the SNe environment metallicities? The statistical tests in chapter 4 revealed no statistical significance of a different parent population but the sensitivity check in section 5.3 creates some doubts on the limitations of the results of the statistical tests. Additionally, as for all statistical tests, if the test does not reject the null hypothesis, this does not mean that the inverse null hypothesis is wrong.

In addition to the statistical result that the hypothesis of common parent population must not be rejected, three conclusions can be drawn from the O3N2 calibration based on visual inspection of the CDFs of Type Ib,c SNe (see Figures 4-5/4-6 and Figures 4-11/4-12).

a) The distribution of Type Ib SNe seems to be narrower than the Type Ic distribution; it starts at higher metallicities and stops at lower metallicities than the Type Ic distribution. This gives some evidence that the single massive progenitor star fraction for Type Ib is larger than for Type Ic. Single massive stars have less physical parameters determining their mass loss (essentially initial mass, metallicity, rotation and magnetic field). Compact binaries have additional orbital and evolutionary parameters of the companion influencing the mass loss rate. The larger number of

physical parameters induces the expectation of a larger scatter (e.g. Xiao et al. 2019) and consequently of broader CDFs for the binary scenario.

b) Type Ic SNe have a broad distribution starting at low metallicities. This is a second hint of a significant binary fraction of Type Ic SNe progenitors. Stripping H- and He-shells at low metallicities by stellar winds only is unlikely because the mass loss strongly depends on metallicity (the higher metallicity the stronger mass loss; e.g. Tramper et al. 2016). Thus, the binary scenario is favoured as the mass stripping mechanism at low metallicities.

c) Regardless of low metallicities of some Type Ic SNe, the Type Ib,c environments tend to have higher metallicities than Type IIP for metallicities of about 8.3 dex and higher (see e.g. Figure 5-1). This point fits to common expectation that WR stars are progenitors of Type Ib,c SNe either as an initially single massive star or a less massive star in a close binary.

The points a) to c) are the only constraints which can be drawn by the CDFs directly. The results of this work do not allow for constraining the initial mass of the progenitors without further assumptions drawn from stellar population and evolution models.

An interesting point would be a similar research like this work for the HII environments of WR stars but no study has been found in the literature. It is known from surveys that WR stars are often associated with HII regions (e.g. Pledger et al. 2018 and references therein) but the local metallicities of the WR star environments are commonly estimated by indirect methods e.g. by the metallicity gradient of the host galaxy. Local metallicities of WR star environments estimated by direct methods have not been found publicly available.

Surveys for WR stars have revealed (e.g. Bibby 2010, Neugent and Massey 2019) a galactocentric gradient of the WC/WN ratio from the high metallicity central regions to the lower metallicity of outer galaxy regions. Figure 5-15 (Neugent and Massey 2011) shows as example the distribution of WR stars in galaxy M33. The WC type stars are more centralised in regions of higher metallicities. The WC/WN ratio drops from 0.58 in the central region to 0.22 in the outer regions in consistence with the decrease of the metallicity from 8.72 to 8.29 dex. As WC type stars are believed to be more stripped than WN type stars, these results are consistent with WN/WC progenitor scenario of Type Ib/Type Ic SNe (see also the discussion on the claimed WN progenitor scenario of iPTF13bvn in section 1.3.2).
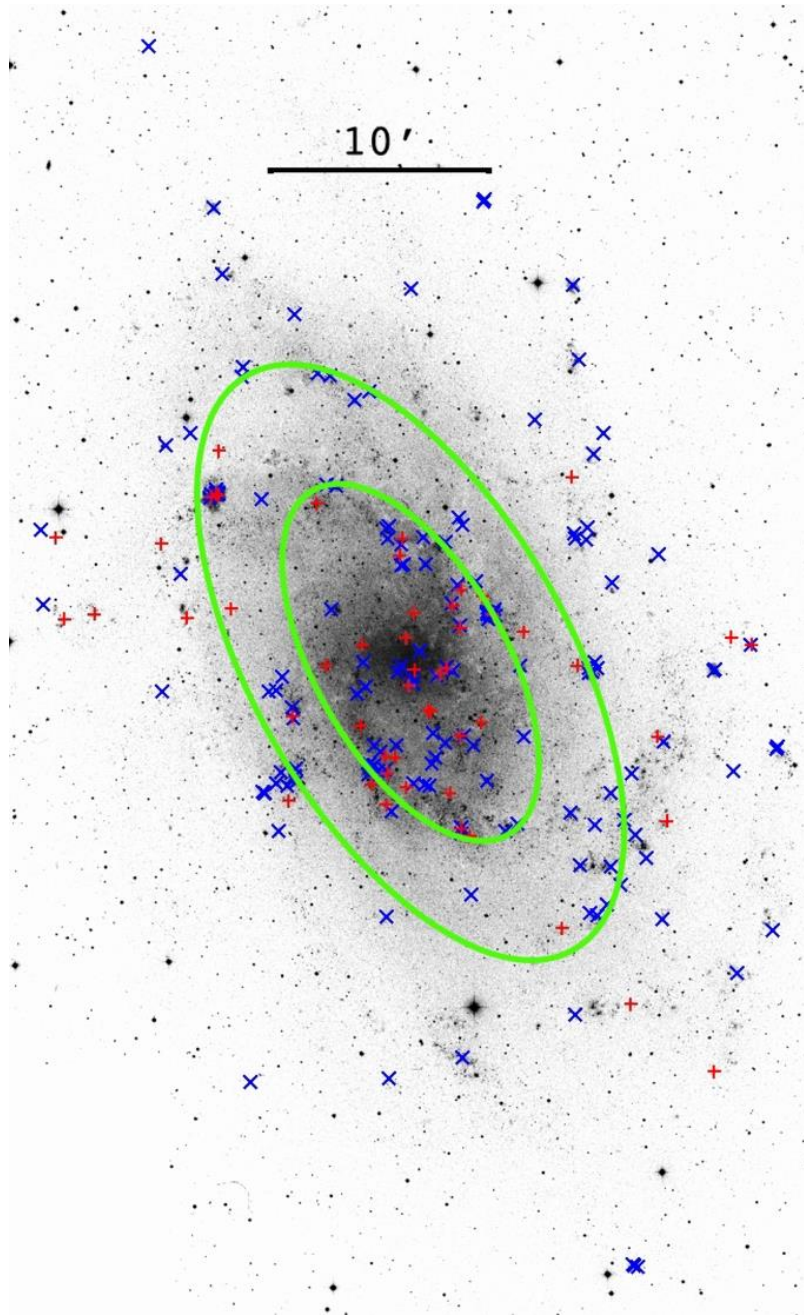
Figure 5-15: Distribution of WR star content of galaxy M33 taken from Neugent and Massey (2011). WN type stars are marked as blue, WC type stars are marked as red. The WC type stars are more centralised in regions of higher metallicities than the WN type stars.

The currently available surveys for WR stars are limited to the local group and nearby galaxies up to a distance of about 8.6 Mpc (Bibby 2010). Surveys to larger distances are affected by resolution issues and the relative faintness of the WR stars requires long telescope times. This may be the reason of the lack of studies with direct metallicity measurements of WR star environments using the strong emission line method.

Chapter 6

Conclusions and Future Work

This work estimated the metallicities of environments of Type IIP, Type Ib and Type Ic SNe within a luminosity distance of 30 Mpc by the strong emission line method. During the runtime of the project 76 targets out of a sample of 110 selected targets could be observed at the INT on La Palma.

For 66 observed targets the metallicities could be measured by the N2 and O3N2 calibrations: 14 Type Ib, 19 Type Ic and 33 Type IIP by N2 calibration with additional O3N2 calibration results for 9 Type Ib, 18 Type Ic and 19 Type IIP. The sample of the INT observations has been extended by results of previous work to 23 Type Ib, 29 Type Ic and 60 Type IIP results of N2 calibration (O3N2: 17 Type Ib, 22 Type Ic and 29 Type IIP) improving the statistical significance of the total sample.

The CDFs of the metallicities of the three SN types have been presented. The CDFs based on O3N2 calibration exhibit distinct features: narrow Type Ib distribution; Type Ic at low metallicities; Type Ib and Ic tend to higher metallicity than Type IIP. However, the statistical tests (KS-test and AD-test) fail to reject the null hypothesis that the different SN types come from the same parent population. According to the results of the statistical tests no constraints for the progenitors of the Type Ib,c SNe can be derived from the CDFs. Based on the largest sample size to date, the KS-test as well as the AD-test provides no statistical significance for a strong difference in metallicity distributions between the environments of the three SN types. The conclusion of this work is thus that Tape Ib, Ic and IIP SNe do not originate from regions of different metallicity.

However the statistical tests are challenged by the simplified sensitivity analysis done: taking into account uncertainties, the tests provide inconclusive results. A full Monte Carlo analysis is required to check the reliability of the tests.

In addition to the statistical test results, the CDFs of the O3N2 calibration results provide some evidence for a significant fraction of single massive stars as Type Ib progenitors: the narrow CDFs starting at relatively high metallicities meet the expectations for stripping by strong stellar winds with a small physical parameter space as given for a single star scenario.

For Type Ic, the CDFs of the O3N2 calibrations provide some evidence of a large fraction of compact binaries as progenitors because Type Ic SNe are present in low metallicity environments. Additionally, the CDFs of Type Ic are significantly broader than the Type Ib CDFs expected as a result of a binary scenario because of the larger physical parameter space.

There is also a general trend to higher metallicities for Type Ib,c SNe compared with Type IIP environments visible in the O3N2 based CDFs.

The current results may be improved by future work in different directions:

- 34 of the 110 selected targets could not be observed during the run time of the project. Observational data of these targets will further improve the statistical significance of the sample.

- The reliability of the statistical tests is challenged by the simplified sensitivity test. This result asks for further support by a full Monte Carlo analysis of the robustness of the statistical tests against uncertainties of the samples under test.

- The N2 calibration seems to be less accurate in the high metallicity range. Investigations of the effects of [NII] saturation and of the N/O ratio on the accuracy/applicability of the N2 calibration would make sense.

- All strong emission line methods using hydrogen lines are challenged by stellar contamination. The simple emission line fit as done by DIPSO does not seem to be adequate to solve this issue. More sophisticated tools like PPXF are required for the emission line fit but the pre-conditions for a successful use of such tools must be evaluated.

- Metallicities of WR star environments are commonly estimated by indirect methods e.g. metallicity gradients only. The search for studies with direct metallicity measurements of the environments of WR stars was not successful. Direct metallicity measurements by the strong emission line method look interesting but are likely hampered by observational issues.

Finally, a short summary of experiences gained in the project:

- The realisation of a clear project design into a practical astronomical project is a critical and difficult issue because of the uncertainties and lack of clear definition present in many astronomical quantities (see discussion in section 2.1)

- The project plan should always be as flexible as possible including fallback options because of imponderables of observation conditions and observation opportunities.

- The creation of an automated pipeline for the data reduction process initially takes some time but the pipeline is very effective for large data sets regarding net time savings and process flexibility. It also provides a complete documentation of the reduction process automatically.

- The sense of the application of statistical significance tests seems to be debatable at least for applications to astronomical data with large uncertainties.

- The project work has been done off-campus completely and it worked excellent without any technical issues. But by far the greatest impressions were the on-site observations at the INT and the work with professional astronomical equipment.

Bibliography

Anderson J.P., Covarrubias R.A., James P.A., Hamuy M., Habergham S.M., 2010, *Observational constraints on the progenitor metallicities of core-collapse supernovae*, MNRAS, 407, 2660.

Anderson J.P., Habergham S.M., James P.A., Hamuy M., 2012, *Progenitor mass constraints for core-collapse supernovae from correlations with host galaxy star formation*, MNRAS, 424, 1372.

Anderson J.P., James P.A., Habergham S.M., Galbany L., Kuncarayakti H., 2015, *Statistical studies of supernova environments*, PASA, 32, 19A.

Arcavi I. et al., 2010, *Core-collapse Supernovae from the Palomar Transient Factory: Indications for a Different Population in Dwarf Galaxies*, ApJ, 721, 777.

Asplund M., Grevesse N., Sauval A.J., Scott P., 2009, *The Chemical Composition of the Sun*, ARA&A, 47, 481.

Bastian N., Covey K.R., Meyer M.R., 2010, *A Universal Stellar Initial Mass Function? A Critical Look at Variations*, ARA&A, 48, 339.

Bersten M.C. et al., 2014, *iPTF13bvn: The First Evidence of a Binary Progenitor for a Type Ib Supernova*, AJ, 148, 68.

Bibby J.L., 2010, *Wolf-Rayet starts as the progenitors of type Ib/c supernovae*, PhD Thesis, University of Sheffield.

Boissier S., Prantzos N., 2009, *Relative frequencies of supernovae types: dependence on host galaxy magnitude, galactocentric radius, and local metallicity*, A&A, 503, 137.

Cao Y. et al., 2013, *Discovery, Progenitor and Early Evolution of a Stripped Envelope Supernova iPTF13bvn*, ApJL, 775, L7.

Cappellari M., 2017, *Improving the full spectrum fitting method: accurate convolution with Gauss-Hermite functions*, MNRAS, 466, 798.

Carroll B.W., Ostlie D.A., 2006, *An introduction to modern astrophysics*, Pearson International Edition, 2nd.ed., Pearson/Addison-Wesley, San Francisco, ISBN 978-0-321-44284-0.

Conti P.S., Crowther P.A., Leitherer C., 2012, *From luminous hot stars to starburst galaxies*, Cambridge University Press, Cambridge, ISBN 978-1-107-40773-2.

Crowther P.A., 2007, *Physical Properties of Wolf-Rayet Stars*, MNRAS, 45, 177.

Crowther P.A., 2013, *On the association between core-collapse supernovae and H ii regions*, MNRAS, 428, 1927.

Crowther P.A., Hadfield L.J., 2006, *Reduced Wolf-Rayet line luminosities at low metallicity*, A&A, 449, 711.

Crowther P.A., Smith L.J., Hillier D.J., Schmutz W., 1995, *Fundamental parameters of Wolf-Rayet stars. III. The evolutionary status of WNL stars.*, A&A, 293, 427.

Crowther P.A., Lennon D.J., Walborn N.R., 2006, *Physical parameters and wind properties of galactic early B supergiants*, A&A, 446, 279.

Currie M.J., Berry D.S., Jenness T., Gibb A.G., Bell G.S., Draper P.W., 2014, *Starlink Software in 2013*, ASPC, 485, 391.

Dopita M.A., Kewley L.J., Sutherland R.S., Nicholls D.C., 2016, *Chemical abundances in high-redshift galaxies: a powerful new emission line diagnostic*, Ap&SS, 361, 61.

Duchêne G., Kraus A., 2013, *Stellar Multiplicity*, ARA&A, 51, 269.

Ekström S. et al., 2012, *Grids of stellar models with rotation. I. Models from 0.8 to 120 $M_\odot$ at solar metallicity (Z = 0.014)*, A&A, 537, A146.

Eldridge J.J., Fraser M., Smartt S.J., Maund J.R., Crockett R.M., 2013, *The death of massive stars - II. Observational constraints on the progenitors of Type Ibc supernovae*, MNRAS, 436, 774.

Eldridge J.J., Fraser M., Maund J.R., Smartt S.J., 2015, *Possible binary progenitors for the Type Ib supernova iPTF13bvn*, MNRAS, 446, 2689.

Eversberg T., Vollmann K., 2015, *Spectroscopic Instrumentation*, Springer Publishing, Heidelberg, ISBN 978-3-662-44534-1.

Fang Q., Maeda K., 2018, *The Origin of the Ha-like Structure in Nebular Spectra of Type IIb Supernovae*, ApJ, 864, 47.

Filippenko A.V., 1997, *Optical spectra of supernovae*, ARA&A, 35, 309.

Folatelli G. et al., 2016, *Disappearance of the Progenitor of Supernova iPTF13bvn*, ApJL, 825, L22.

Freedman R.A., Kaufmann W.J., 2008, *Universe*, 8th ed., W.H. Freeman and Co, New York, ISBN 978-0-7167-8584-2.

Galbany L. et al., 2014, *Nearby supernova host galaxies from the CALIFA Survey: I. Sample, data analysis, and correlation to star-forming regions*, A&A, 572, A38.

Galbany L. et al., 2016, *Nearby supernova host galaxies from the CALIFA survey: II. Supernova environmental metallicity*, A&A, 591, A48.

Galbany L. et al., 2018, *PISCO: The PMAS/PPak Integral-field Supernova Hosts Compilation*, ApJ, 855, 107.

Gal-Yam A., 2019, *The Most Luminous Supernovae*, ARA&A, 57, 305.

Gal-Yam A. et al., 2007, *On the Progenitor of SN 2005gl and the Nature of Type IIn Supernovae*, ApJ, 656, 372.

Girardi L., Bressan A., Bertelli G., Chiosi C., 2000, *Evolutionary tracks and isochrones for low- and intermediate-mass stars: From 0.15 to 7 M_{sun}, and from Z=0.0004 to 0.03*, A&AS, 141, 371.

Groh J. H., Meynet G., Ekström S., 2013, *Massive star evolution: luminous blue variables as unexpected supernova progenitors*, A&A, 550, L7.

Groh Jose H., Georgy C., Ekstrom S., 2013, *Progenitors of supernova Ibc: a single Wolf-Rayet star as the possible progenitor of the SN Ib iPTF13bvn*, A&A, 558, L1.

Guillochon J., Parrent J., Kelley L.Z., Margutti R., 2017, *An Open Catalog for Supernova Data*, ApJ, 835, 64.

Gutiérrez C.P. et al., 2017, *Type II Supernova Spectral Diversity. I. Observations, Sample Characterization, and Spectral Line Evolution*, ApJ, 850, 89.

Heger A., Fryer C.L., Woosley S.E., Langer N., Hartmann D.H., 2003, *How Massive Single Stars End Their Life*, ApJ, 591, 288.

Henry R.B.C., Worthey G., 1999, *The Distribution of Heavy Elements in Spiral and Elliptical Galaxies*, PASP, 111, 919.

Janka H.-T., 2012, *Explosion Mechanisms of Core-Collapse Supernovae*, ARN&P, 62, 407.

Kewley L.J., Ellison S.L., 2008, *Metallicity Calibrations and the Mass-Metallicity Relation for Star-forming Galaxies*, ApJ, 681, 1183.

Kilpatrick C.D. et al., 2018, *A potential progenitor for the Type Ic supernova 2017ein*, MNRAS, 480, 2072.

Kippenhahn R., Weigert A. and Weiss A., 2012, *Stellar structure and evolution*, 2nd ed., Springer Publishing, Heidelberg, ISBN 978-3-642-30304-3.

Kozyreva A., Yoon S.-C., Langer N., 2014, *Explosion and nucleosynthesis of low-redshift pair-instability supernovae*, A&A, 566, A146.

Kreyszig E., 1998, *Statistische Methoden und ihre Anwendungen (Statistical Methods and their Applications)*, 7th ed., Vandenhoeck & Ruprecht Publishing, Göttingen, ISBN 3-525-40717-3.

Kudritzki R.-P., Puls J., 2000, *Winds from hot stars*, ARA&A, 38, 613.

Kuncarayakti H. et al., 2018, *Constraints on core-collapse supernova progenitors from explosion site integral field spectroscopy*, A&A, 613, A35.

Kurtz S., 2005, *Hypercompact HII regions*, IAUS, 227, 111.

Lada C.J., Lada E.A., 2003, *Embedded Clusters in Molecular Clouds*, ARA&A, 41, 57.

Laing R., Jones D., 1985, *The Isaac Newton Group*, VA, 28, 483.

Lane, D., Scott, D., Hebl, M., Guerra, R., Osherson, D., Zimmer, H., 2019, *Introduction to Statistics*, [ebook] David Lane, Available at: http://onlinestatbook.com/Online_Statistics_Education.pdf [Accessed 26 Nov. 2019].

Lee E.S., Forthofer R.N., 2006, *Analyzing complex survey data*, 2nd ed., Sage Publications, Thousand Oaks, ISBN 978-1-412-98334-1.

Leitherer C., 2005, *Age-Dating of Starburst Galaxies*, AIPC, 783, 280.

Leloudas G. et al., 2011, *The properties of SN Ib/c locations*, A&A, 530, A95.

Levesque E.M., 2010, *The physical properties of red supergiants*, NewAR, 54, 1.

Li W. et al., 2011a, *Nearby supernova rates from the Lick Observatory Supernova Search – II. The observed luminosity functions and fractions of supernovae in a complete sample*, MNRAS, 412, 1441.

Li W. et al., 2011b, *Nearby supernova rates from the Lick Observatory Supernova Search - III. The rate-size relation, and the rates as a function of galaxy Hubble type and colour*, MNRAS, 412, 1473.

Makarov D., Prugniel P., Terekhova N., Courtois H. and Vauglin I., 2014, *HyperLEDA. III. The catalogue of extragalactic distances*, A&A, 570, A13.

Maoz D., Mannucci F., Nelemans G., 2014, *Observational Clues to the Progenitors of Type Ia Supernovae*, ARA&A, 52, 107.

Marino R.A. et al., 2013, *The O3N2 and N2 abundance indicators revisited: improved calibrations based on CALIFA and Te-based literature data*, A&A, 559, A114.

Marsaglia G., Tsang W.W., Wang J., 2003, *Evaluating Kolmogorov's Distribution*, JSS, 8, 1.

Massey F.J., 1952, *Distribution Table for the Deviation Between two Sample Cumulatives*, AoMS, 23, 435.

Massey P., 2013, *Massive stars in the galaxies of the Local Group*, NewAR, 57, 14.

Massey P., Strobel K., Barnes J.V., Anderson E., 1988, *Spectrophotometric standards*, ApJ, 328, 315.

Mauerhan J.C. et al., 2013, *The unprecedented 2012 outburst of SN 2009ip: a luminous blue variable star becomes a true supernova*, MNRAS, 430,1801.

Modjaz M., Kewley L., Bloom J.S., Filippenko A.V., Perley D., Silverman J.M., 2011, *Progenitor Diagnostics for Stripped Core-collapse Supernovae: Measured Metallicities at Explosion Sites*, ApJL, 731, L4.

Neugent K.F., Massey P., 2011, *The Wolf-Rayet Content of M33*, ApJ, 733, 123.

Neugent K.F., Massey P., 2019, *The Wolf-Rayet Content of the Galaxies of the Local Group and Beyond*, arXiv:astro-ph/1908.06238.

Oke J.B., 1974, *Absolute Spectral Energy Distributions for White Dwarfs*, ApJS, 27, 21.

Oke J.B., Gunn J.E., 1983, *Secondary standard stars for absolute spectrophotometry.*, ApJ, 266, 713.

Osterbrock D.E., Ferland G.J., 2006, *Astrophysics of gaseous nebulae and active galactic nuclei*, 2nd ed., University Science Books, Sausalito, ISBN 1-891389-34-3.

Pagel B.E.J., Edmunds M.G., Blackwell D.E., Chun M.S., Smith G., 1979, *On the composition of H II regions in southern galaxies - I. NGC 300 and 1365.*, MNRAS, 189, 95.

Perets H.B. et al., 2010, *A faint type of supernova from a white dwarf with a helium-rich companion*, Nature, 465, 322.

Pettini M., Pagel B.E.J., 2004, *[OIII]/[NII] as an abundance indicator at high redshift*, MNRAS, 348, L59.

Pettitt A.N., 1976, *A Two-Sample Anderson--Darling Rank Statistic*, Biometrika, 63, 161.

Pledger J.L., Shara M.M., Wilde M., Crowther P.A., Long K.S., Zurek D., Moffat A.F.J., 2018, *The first optical spectra of Wolf–Rayet stars in M101 revealed with Gemini/GMOS*, MNRAS, 473, 148.

Press W.H. (ed.), 1988, *Numerical recipes in C: the art of scientific computing*; Cambridge University Press, Cambridge, ISBN 0-521-35465-X.

Puls J., Vink J.S., Najarro F., 2008, *Mass loss from hot massive stars*, A&ARv, 16, 209.

Richardson D., Branch D., Casebeer D., Millard J., Thomas R.C., Baron E., 2002, *A Comparative Study of the Absolute Magnitude Distributions of Supernovae*, AJ, 123, 745.

Sana H. et al., 2012, *Binary interaction dominates the evolution of massive stars*, Science, 337, 444.

Sana H. et al., 2013, *Multiplicity of massive O stars and evolutionary implications*, ASPC, 470, 141.

Sanders N.E. et al., 2012, *A Spectroscopic Study of Type Ibc Supernova Host Galaxies from Untargeted Surveys*, ApJ, 758, 132.

Sanyal D., Grassitelli L., Langer N., Bestenlehner J.M., 2015, *Massive main-sequence stars evolving at the Eddington limit*, A&A, 580, A20.

Schaller G., Schaerer D., Meynet G., Maeder A., 1992, *New grids of stellar models from 0.8 to 120 M_solar at Z=0.020 and Z=0.001*, A&AS, 96, 269.

Smartt S.J., 2009, *Progenitors of Core-Collapse Supernovae*, ARA&A, 47, 63.

Smartt S.J., 2015, *Observational Constraints on the Progenitors of Core-Collapse Supernovae: The Case for Missing High-Mass Stars*, PASA, 32, id.e016.

Smartt S.J., Maund J.R., Hendry M.A., Tout C.A., Gilmore G.F., Mattila S., Benn C.R., 2004, *Detection of a Red Supergiant Progenitor Star of a Type II-Plateau Supernova*, Science, 303, 499.

Smith N., 2017, *Luminous blue variables and the fates of very massive stars*, RSTA, 375, id.2016.0268.

Smith N., Li W., Filippenko A.V., Chornock R., 2011, *Observed fractions of core-collapse supernova types and initial masses of their single and binary progenitor stars*, MNRAS, 412, 1522.

Sparke L.S., Gallagher J.S., 2007, *Galaxies in the universe: an introduction*, 2nd ed., Cambridge University Press, Cambridge, ISBN 978-0-521-67186-6.

Stasinska G., 2002, *Abundance determinations in HII regions and planetary nebulae*, arXiv:astro-ph/0207500.

Sternberg A., Hoffmann T.L., Pauldrach A.W.A., 2003, *Ionizing Photon Emission Rates from O- and Early B-Type Stars and Clusters*, ApJ, 599, 1333.

Stone R.P.S., 1977, *Spectral energy distributions of standard stars of intermediate brightness II*, ApJ, 218, 767.

Strömgren B., 1939, *The Physical State of Interstellar Hydrogen*, ApJ, 89, 526.

Suh H., Yoon S., Jeong H. and Yi S.K., 2011, *Early-Type Host Galaxies of Type II and Ib Supernovae*, ApJ, 730, 110.

Taddia F. et al., 2013, *Carnegie Supernova Project: Observations of Type IIn supernovae*, A&A, 555, A10.

Taddia F. et al., 2019, *Analysis of broad-lined Type Ic supernovae from the (intermediate) Palomar Transient Factory*, A&A, 621, A71.

Tody D., 1986, *The IRAF Data Reduction and Analysis System*, SPIE, 627, 733.

Tramper F., Sana H., de Koter A., 2016, *A New Prescription for the Mass-loss Rates of WC and WO Stars*, ApJ, 833, 133.

Tremonti C.A. et al., 2004, *The Origin of the Mass-Metallicity Relation: Insights from 53,000 Star-forming Galaxies in the Sloan Digital Sky Survey*, ApJ, 613, 898.

Tsvetkov D.Y., Pavlyuk N.N., Bartunov O.S., 2004, *The SAI Catalog of Supernovae and Radial Distributions of Supernovae of Various Types in Galaxies*, AstL, 30, 729.

Turatto M., 2003, *Classification of Supernovae*, arXiv:astro-ph/0301107.

Van der Hucht K.A., 2001, *The VIIth catalogue of galactic Wolf–Rayet stars*, NewAR, 45, 135.

Van Dyk S.D., Li W., Filippenko A.V., 2003, *On the Progenitor of the Type II-Plateau Supernova 2003gd in M74*, PASP, 115, 1289.

Van Dyk S.D. et al., 2018, *SN 2017ein and the Possible First Identification of a Type Ic Supernova Progenitor*, ApJ, 860, 90.

Vazdekis A. et al., 2010, *Evolutionary stellar population synthesis with MILES - I. The base models and a new line index system*, MNRAS, 404, 1639.

Woosley S.E., Bloom J.S., 2006, *The supernova–gamma-ray burst connection*, ARA&A, 44, 507.

Woosley S.E., Heger A., Weaver T.A., 2002, *The evolution and explosion of massive stars*, RvMP, 74, 1015.

Xiao L., Galbany L., Eldridge J.J., Stanway E.R., 2019, *Core-collapse supernovae ages and metallicities from emission-line diagnostics of nearby stellar populations*, MNRAS, 482, 384.

All links of the thesis last visited on 07-Jun-2020

Appendix

A.1 Acronyms

1D   1-dimensional

2D   2-dimensional

AD-test   Anderson-Darling test

ADU   analog to digital conversion unit

BSG   blue supergiant

CCD   charge coupled device

CDF   cumulative distribution function

FITS   flexible image transport system (astronomical image standard)

FWHM   full width at half maximum

GRB   gamma ray burst

HR   Hertzsprung-Russell

IDS   Intermediate Dispersion Spectrograph

ING   Isaac Newton Group of Telescopes

INT   Isaac Newton Telescope

IRAF   image reduction and analysis facility (data reduction software)

KE08   Kewley and Ellison 2008

KS-test   Kolmogorov-Smirnov test

LBV   luminous blue variable

M13   Marino et al. 2013

N2   name of calibration method based on Hα and [NII]

NTT   New Technology Telescope

O3N2   name of calibration method based on Hα, Hβ, [NII] and [OIII]

PP04   Pettini and Pagel 2004

PPXF   penalized pixel fitting (data fitting software)

RSG   red supergiant

SN   supernova

SNR   signal to noise ratio

WR   Wolf-Rayet

YSG   yellow supergiant

A.2 Permutation Method in 'R'-package 'twosamples'

Description of fast permutation method for calculation of the p-values of the statistical tests in the 'R' package 'twosamples' as citation of page https://github.com/cdowd/twosamples:

(start of citation)

Permutation Testing

Once we have a metric measuring distance between two samples, its easy enough to code up a testing procedure.

Specifically we want to test the following: * H0: J=K

where Sample 1 is distributed i.i.d. from J and Sample 2 is i.i.d. from K.

Broadly, under this null, observations from sample 1 and sample 2 are exchangeable.That is -- by randomly swapping observations between the samples, we can generate a new, equally likely data set from the same (Null) DGP. Then we can calculate our metric for distance between the samples on this data set. By repeating this procedure many times, we can generate a null distribution for our distance metric. We can then compare our observed distance to the null distribution. Because distances are non-negative, this will be a one-sided comparison. (Though if you wanted to test whether a sample was hyper-regular you could do that by looking at the one-sided test to the bottom).

Moreover, unlike other, more general, two-sample procedures we do not rely on any properties of the underlying distribution. Some procedures require continuity, derivatives, or smoothness to get their asymptotic and finite sample guarantees. Those are procedures which estimate the underlying density, rather than simply working working the ECDF. The testing procedures in this package only rely on the statement that observations are i.i.d. The Independence is necessary for the exchangeability statement to hold. The identicality is necessary for the null hypothesis to be a sensible claim.

(end of citation)

The webpage also contains examples of code for distance metric calculation; webpage last visited on 07-Jun-2020.